CHARACTERIZING MOLECULAR DYNAMICS OF POLYMER GLASS AND GEL PHASE TRANSITIONS AS A FUNCTION OF TIME, TEMPERATURE, AND CONCENTRATION USING NUCLEAR MAGNETIC RESONANCE

by

April Marie Dower

A thesis submitted in partial fulfillment
of the requirements for the degree

of

Master of Science

in

Chemical Engineering

MONTANA STATE UNIVERSITY
Bozeman, Montana

April 2016

DEDICATION

This thesis is dedicated to Dad, Mom, Jer, and M. My time in college would not have been nearly as wonderful without all of you.

ACKNOWLEDGEMENTS

Thank you to Joe Seymour for all of the teaching, assistance, and overall guidance during the writing of this thesis.

TABLE OF CONTENTS

1. BASICS OF NMR 1

History1 1
Basic Signal Detection 2
Magnetic Field Gradients 4
Spin Relaxation 5
Simple Pulse Sequences 9
Single-Pulse 9
Inversion Recovery 11
CPMG Train 12
PGSE Experiment 14
Phase Cycling 16
The Bloch Equations 18
Equipment 19

2. ADVANCED NMR CONCEPTS 21

Diffusometry 21
2D Relaxometry 29
T_1-T_2 Correlation 30
T_2-T_2 Correlation 35

3. HPMCAS/ACETONE SYSTEMS 41

Glass Transitions 42
Methods 43
Sample Preparation 43
2D Relaxometry and Diffusometry Measurements 44
Temperature Control 46
Data Analysis 46
Observing Glass Transitions with T_1-T_2 Maps 47
Mesh Size Determination with T_2-T_2 Experiments 52
Mesh Size Determination with Time-Dependent Diffusion 62
Conclusions 67

4. PSEUDOLATEX 69

Thermal Gelation 69
Aging Mechanisms 73
Methods 74
Sample Preparation 74
2D Relaxometry and Diffusometry Measurements 74
Temperature Control 75

TABLE OF CONTENTS - CONTINUED

Data Analysis 76
Polymer 1 Pseudolatex 76
T_1-T_2 Studies 77
T_2-T_2 and Diffusion Studies 80
Conclusions 83
Polymer 2 Pseudolatex 83
Thermal Gelation Model 84
Plasticization 88
T_1-T_2 Studies 88
T_2-T_2 Studies 97
Diffusion Studies 99
Conclusions 102

5.DRIED POLYMER FILMS **104**

Methods 104
Sample Preparation 104
2D Relaxometry Measurements 105
Temperature Control 105
Data Analysis 106
Wet Polymer Formulations 106
Dry Films 107
Conclusions 111

6.FUTURE WORK **112**

HPMCAS/Acetone Systems 112
Pseudolatex 112
Dried Polymer Films 113

REFERENCES CITED 114

LIST OF TABLES

Table Page

1.1. High power probe parameters 20

3.1. Characteristic time and length scales for HPMCAS/acetone systems..... 57

3.2. Length scales for 7 wt% acetone HPMCAS sample 67

4.1. Ages of polymer 1 pseudolatex samples 77

4.2. Plasticizer contents of polymer 2 pseudolatex samples 84

LIST OF FIGURES

Figure Page

1.1. Parallel and anti-parallel spin energy levels 3

1.2. Net magnetization vector aligned in z-direction 3

1.3. Regimes of T_1 and T_2 relaxation 8

1.4. Movement of magnetization vector in a single-pulse experiment 9

1.5. FID from a single-pulse experiment 10

1.6. Inversion recovery plot 11

1.7. CPMG pulse sequence 13

1.8. PGSE pulse sequence 14

1.9. Spin phase in a PGSE sequence 15

1.10. Coherence pathways 17

1.11. 250 MHz superconducting magnet image 19

2.1. PGSE pulse sequence 21

2.2. Effective gradients 22

2.3. Phase of a diffusing spin in a PGSE sequence 23

2.4. Stejskal-Tanner plot 26

2.5. Spectrum of a polymer/water system 27

2.6. T_1-T_2 pulse sequence 30

2.7. 2D ILT Interface in Matlab 33

2.8. T_1-T_2 Contour map 34

2.9. T_2-T_2 pulse sequence 35

LIST OF FIGURES - CONTINUED

Figure Page

2.10. Spins in a theoretical large and small domain 36

2.11. Theoretical short mixing time T_2-T_2 map..... 37

2.12. Theoretical long mixing time T_2-T_2 map 38

2.13. Mixing peak intensity vs mixing time plot..... 39

3.1. Structure of HPMCAS 41

3.2. Polymer solution undergoing a glass transition..... 43

3.3. HPMCAS/acetone system T_1-T_2 map 48

3.4. Varied concentration and temperature HPMCAS/acetone T_1-T_2 maps 50

3.5. Varied temperature SDD T_1-T_2 maps..... 51

3.6. 7 wt% acetone HPMCAS/acetone at 22°C T_2-T_2 maps 53

3.7. T_2-T_2 analysis plot of 7 wt% acetone HPMCAS/acetone sample at 22°C 54

3.8. 7 wt% acetone HPMCAS/acetone at 60°C T_2-T_2 maps 56

3.9. T_2-T_2 analysis plot of 7 wt% acetone HPMCAS/acetone sample at 60°C 57

3.10. 7 wt% acetone HPMCAS/acetone at 0°C T_2-T_2 maps 58

3.11. T_2-T_2 analysis plot of 7 wt% acetone HPMCAS/acetone sample at 0°C 59

3.12. SDD at 22°C T_2-T_2 maps 60

3.13. T_2-T_2 analysis plot of SDD at 22°C..... 61

3.14. Diffusion measurements of xenon in bead packs 63

3.15. Diffusion measurements of 7 wt% acetone HPMCAS/acetone sample..... 64

3.16. MSD vs observation time of 7 wt% acetone HPMCAS/acetone sample..... 65

LIST OF FIGURES - CONTINUED

Figure Page

3.17. Acetone molecule surrounded by polymer 66

4.1. Rheology measurements of polymer 2 during thermal gelation 71

4.2. Images of polymer 2 pseudolatex before and after gelation 72

4.3. T_1-T_2 maps of polymer 1 pseudolatex at 22°C and 45°C 78

4.4. Images of polymer 1 pseudolatex before and after gelation 80

4.5. T_2-T_2 maps of polymer 1 pseudolatex at 22°C and 45°C 81

4.6. Diffusion measurements of polymer 1 pseudolatex at 22°C and 45°C 82

4.7. Model of ungelled polymer 2 pseudolatex 85

4.8. Diffusion spectrum of polymer 2 pseudolatex 86

4.9. Model of gelled polymer 2 pseudolatex 87

4.10. T_1-T_2 thermal gelation of polymer 2 F aged 2 months 89

4.11. T_1-T_2 thermal gelation of polymer 2 A aged 2 months 90

4.12. T_1-T_2 thermal gelation of polymer 2 A aged 4.5 months 92

4.13. T_1-T_2 thermal gelation of new polymer 2 F 93

4.14. T_1-T_2 thermal gelation of new polymer 2 E 94

4.15. T_1-T_2 aging effects on entrained water peak 95

4.16. T_1-T_2 plasticizer effects on entrained water peak 96

4.17. T_1-T_2 of polymer 2 F aged 6 months total 97

4.18. T_2-T_2 analysis plot of polymer 2 F aged 6 months total 98

4.19. T_2-T_2 maps of polymer 2 F aged 6 months total 99

LIST OF FIGURES - CONTINUED

Figure Page

4.20. Water peak diffusion coefficients of polymer 2 pseudolatex 100

4.21. Varied temperature diffusion coefficients of polymer 2 pseudolatex..... 101

5.1. Wet polymer formulation T_1-T_2 maps 107

5.2. Dry polymer film T_1-T_2 maps 108

5.3. T_2-T_2 maps of dry polymer films 109

5.4. T_2-T_2 analysis plot of dry polymer films..... 110

ABSTRACT

Polymers can be used for a variety of applications and impact many aspects of our lives. This thesis investigates the dynamics of polymer gel and glass transitions over different times, temperatures, and concentrations using nuclear magnetic resonance (NMR) with the goal of further understanding these important systems.

A polymer/solvent system, hydroxypropylmethylcellulose acetate succinate (HPMCAS) and acetone, was examined using magnetic relaxation correlation and exchange experiments to characterize domains of different molecular mobility over various temperatures and concentrations. Diffusometry was employed to support the results of the 2D relaxometry experiments. A simple relaxometry method to determine glassiness was verified, and characteristic length scales of a polymer solution at different temperatures were quantified using both relaxation exchange methods and diffusion data. Glasslike dynamics were observed in gelled polymer systems above their glass transition temperatures.

The thermal gelation properties of colloidal polymer dispersions and the effects of different formulations on dry film formation of a polymer mixture were studied as well. Aging and plasticizer effects were examined in the colloidal polymer dispersions using magnetic relaxation correlation experiments along with diffusion experiments to understand molecular dynamics, and it was concluded that pre-gelation particle aggregates were necessary for the systems to thermally gel. The final polymer study aimed to determine why a formulation using differently-substituted polymer produced dry films with dissimilar mechanical properties than another. Using relaxometry data and quantitative length scales acquired through relaxation exchange, it was found that one mixture retained larger domains of water upon dry film formation, allowing the film to be less brittle.

BASICS OF NMR

History

Since the first observation of nuclear magnetic resonance (NMR) through the deflection of atoms in a molecular beam apparatus by Rabi in 1944 [1], the field has grown immensely and allowed insight into areas ranging from the dynamical processes of living systems to the microscale workings of complex polymer systems. Early work by Bloch, Hansen, and Packard at Stanford [2] along with studies by Purcell, Torrey, and Pound from Harvard in 1946 [3] explained the basic physics behind NMR and set the stage for the next seventy years of refinement and expansion of the phenomenon [4]. Because of its non-invasive properties and unique sensitivity to the rotational and translational movement of molecules, the method has been successfully applied to the advancement of fields including pharmacy, chemistry, physics, and materials science. This chapter will introduce the reader to the basic concepts of NMR, and the next will delve into some deeper concepts relevant to the research discussed in this thesis.

NMR utilizes the fundamental property of nuclei called "spin." Because this is a quantum property, it cannot be thought of as the nuclei physically spinning; however, they do behave mathematically as if they are so the term is fitting. These spins impart to each nuclei an intrinsic angular momentum and thus a magnetic moment which interacts with the environment. These spins are normally oriented randomly and have a net magnetic vector sum of zero, but when a magnetic field is applied, the spins align either parallel or anti-parallel with the field. The parallel state is slightly more energetically favorable than the anti-parallel state so the distribution of spins becomes slightly skewed in the parallel direction, causing a net magnetization vector parallel to the applied field. This magnetization vector can be

manipulated and a signal which gives information about the sample can be detected. Because spins of opposite signs in particles can pair up and cancel observable effects, NMR can only be performed on compounds containing unpaired nuclear spins. The most commonly used nuclei is that of the hydrogen atom [5].

Basic Signal Detection

The interaction energy between the magnetic field and the spins is known as the Zeeman interaction energy [6] and is quantified as:

$$H = -\gamma \hbar B_0 m \tag{1.1}$$

where H is the Hamiltonian energy operator, γ is a value unique to each type of nuclei called the gyromagnetic ratio, $\hbar$ is Planck's constant divided by 2π, B_0 is the strength of the applied magnetic field, and m is a value that varies by integer values which defines the spin angular momentum quantum number. A consequence of this interaction is that the energy difference between the parallel and anti-parallel states of spins in a magnetic field is discrete and equal to $\gamma \hbar B_0$ [5]. Figure 1.1 depicts these states and the orientation of nuclei in a macroscopic way. Bear in mind that a real sample contains more spins than could ever be drawn on a figure and that the orientation of the spins is stochastic (governed by Boltzmann statistics) rather than deterministic.

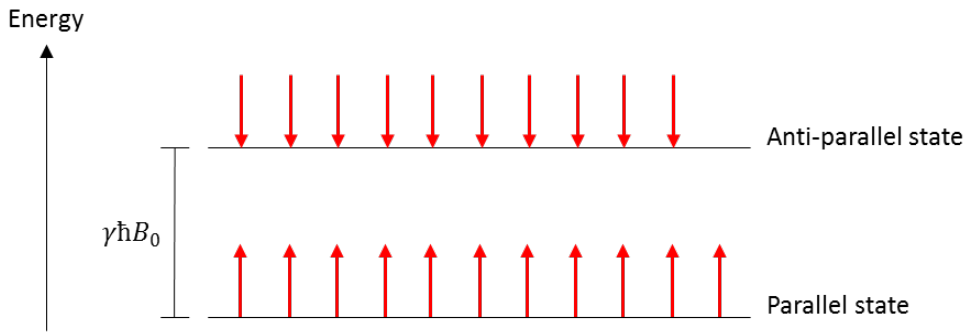

Figure 1.1. A small surplus of spins align in the parallel state as it is in a lower energy level than the anti- parallel state.

By convention, the direction of the B_0 field and therefore the net magnetization vector at equilibrium, M_0, is defined to be in the z direction as shown in Figure 1.2.

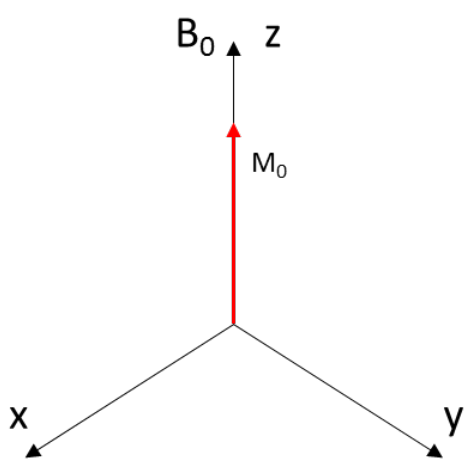

Figure 1.2. The net magnetization vector and the B_0 field are directed along the z-axis at equilibrium.

In an applied magnetic field, spins precess about the field at a natural frequency specific to their type. This frequency is called the Larmor Frequency, ω_0, and is equal to γB_0. NMR experiments take advantage of this frequency in the manipulation of spins. Before samples are inserted into

the magnet, a radio frequency (RF) coil is placed around them. This coil serves the dual purpose of applying resonant RF pulses to the spins in the sample and collecting information as the net magnetization vector precesses about the magnetic field and therefore induces an electric current in the coil. RF coils are designed to have an adjustable capacitance that allows them to be tuned to the frequency of the sample spins and to match the impedance of the probe circuitry to that of the external hardware, thus efficiently transferring power to and from the probe [7]. They are composed of wires organized in a variety of patterns, and a saddle coil design was utilized for the experiments in this thesis. In order to acquire a signal from a sample, the spins are manipulated using RF pulses of an energy proportional to the Larmor Frequency. These pulses can be used to tip the net magnetization vector from equilibrium to any coordinate in the Cartesian system shown in Figure 1.2, A huge number of different pulse sequences have been designed to acquire specific information from all sorts of samples [5].

Magnetic Field Gradients

It has been shown that the magnetization vector can be manipulated using RF pulses in order to obtain information about a system. Gradients in the magnetic field can also be manipulated to find specific information [8]. Gradient coils encase both the sample and the RF coil and consist of solid copper cylinders with current patterns cut into them. Inherent in their design are their maximum strength measured in Teslas per meter, resistance, and time required to switch on (rise time) – these properties vary among coils and are optimized for different purposes. Before an experiment is begun, current in a shim gradient coil is manipulated with the purpose of making small changes in the B_0 field until it is as homogeneous around the sample as possible. This process is referred to as shimming. During experiments, gradients can

be applied for a variety of reasons including the selection of a sample slice for imaging by encoding position into precession frequency, the marking of spins during a diffusion scan, or the elimination of unwanted signal [5]. Gradients will be further discussed later in terms of the diffusion pulse sequence.

Spin Relaxation

A common manipulation of the magnetization vector is the tipping from equilibrium along the z-axis 90° to the x-y (transverse) plane, a procedure accomplished with an RF pulse of a specified duration and power. Once the spins have been tipped, they begin to precess at their Larmor frequency in the x-y plane and return to equilibrium over time by a process known as spin-lattice or T_1 relaxation. The growth over time of the magnetization vector in the z-direction, M_z, is described by an equation involving the T_1 time constant [9]:

$$M_z = M_0\left(1 - 2e^{\frac{-t}{T_1}}\right) \tag{1.2}$$

Consider now the spins directly after they have "felt" the 90° RF pulse and are in the x-y plane. They each experience a slightly different magnetic field and therefore rotate at their own, unique Larmor Frequency since the frequency is a function of magnetic field strength. This causes them to de-phase over time, eventually completely losing coherence and causing the net transverse magnetization to be zero, a process is referred to as spin-spin or T_2 relaxation. The following equation involving the time constant T_2 describes the transverse magnetization ($M_{x,y}$) as it returns to its equilibrium value (M_0) [5]:

$$M_{x,y} = M_0 e^{\frac{-t}{T_2}} \tag{1.3}$$

De-phasing in the transverse plane arises from two factors. First, molecular dipolar spin-spin interactions cause pure T_2 relaxation and second, inhomogeneities in the B_0 field cause inhomogeneous T_2 relaxation. Combining both of these effects yields a value known as T_2* which can be calculated by adding the inverses of T_2 and $T_{2inhomo}$.

$$\frac{1}{T_2^*} = \frac{1}{T_2} + \frac{1}{T_{2inhomo}} \tag{1.4}$$

T_2 relaxation is always faster than or equal to T_1 relaxation. That is, the spins will de-phase in the transverse plane before they return to the positive z axis. However, both processes occur simultaneously [5].

Equations 1.2 and 1.3 arise from a phenomenological description of T_1 and T_2 based on the Bloch equations (see Equation 1.8) and describe the relaxation process well, but T_1 and T_2 can be further understood using spectral density functions. T_1 can be analyzed using time-dependent perturbation theory of the Hamiltonian since it occurs in the laboratory frame where dipolar interactions are weak in comparison to the longitudinal Zeeman field [5, 10]. After considering the transition rate between the two energy states for a spin ½ nuclei, making substitutions, and doing a great deal of algebraic manipulations, one can arrive at the expression [10]:

$$\frac{1}{T_1} = \left(\frac{\mu_0}{4\pi}\right)^2 \gamma^4 \hbar^2 \frac{3}{2} I(I+1)\left[J^{(1)}(\omega_0) + J^{(2)}(2\omega_0)\right] \tag{1.5}$$

where *I* is the angular momentum quantum number and $J^{(1)}(\omega_0)$ and $J^{(2)}(2\omega_0)$ are spectral density functions. A similar equation can be found for T_2 relaxation, but the laboratory frame is no longer applicable since T_2 is naturally described in the rotating frame. Therefore, Bloembergen, Purcell, and Pound (BPP) theory is utilized instead of time-dependent

perturbation theory, the density matrix equation of motion is solved to first order and the decay of M_y determined to yield [11]:

$$\frac{1}{T_2} = \left(\frac{\mu_0}{4\pi}\right)^2 \gamma^4 \hbar^2 \frac{3}{2} I(I+1) \left[\frac{1}{4} J^{(0)}(0) + \frac{5}{2} J^{(1)}(\omega_0) + \frac{1}{4} J^{(2)}(2\omega_0)\right] \tag{1.6}$$

where $J^{(0)}(0)$ is a spectral density function not involved in T_1 relaxation. In order to understand the physical significance of Equations 1.5 and 1.6, it is necessary to find expressions for the spectral density functions. The following equations show these functions evaluated for a simple isotropic rotational diffusion model, a reasonable approximation for most liquids [10]:

$$J^{(0)}(\omega) = \frac{24}{15 r_{ij}^6} \frac{\tau_c}{1 + \omega^2 \tau_c^2} \tag{1.7}$$

$$J^{(1)}(\omega) = \frac{4}{15 r_{ij}^6} \frac{\tau_c}{1 + \omega^2 \tau_c^2}$$

$$J^{(2)}(\omega) = \frac{16}{15 r_{ij}^6} \frac{\tau_c}{1 + \omega^2 \tau_c^2}$$

In these equations, τ_c represents the rotational correlation time and $\frac{1}{r_{ij}^6}$ is a dipole interaction field decay between dipoles *i* and *j* a distance r_{ij} apart. Each spectral density function corresponds to a dipolar interaction between a pair of like spins. Notice that the expression for $\frac{1}{T_2}$ contains $J^{(0)}(0)$ whereas that for $\frac{1}{T_1}$ does not. These equations quantitatively state that T_2 must always be less than or equal to T_1. Figure 1.3 shows a plot of Equations 1.5 and 1.6 [5].

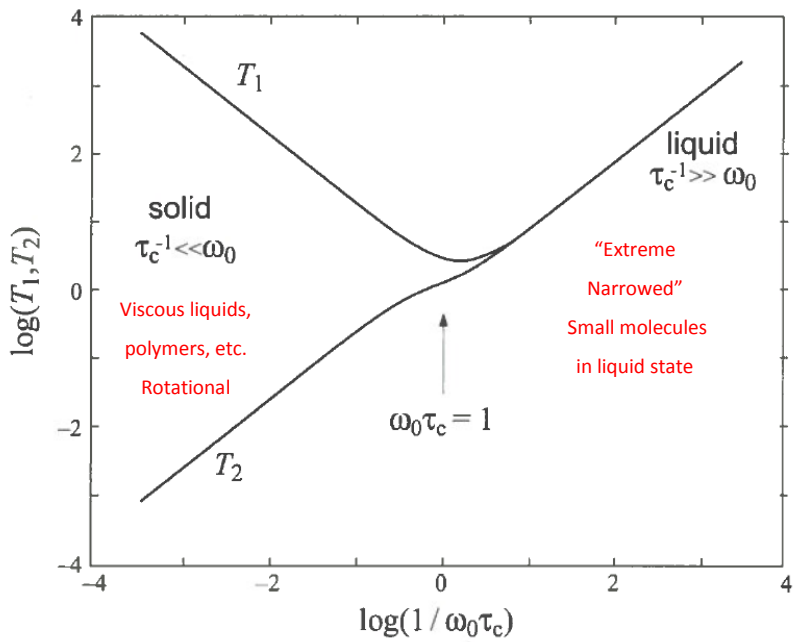

Figure 1.3. Different regimes of T_1 and T_2 relaxation [5]

Solid-like substances have a long correlation time and therefore tend towards the regime with a long T_1 and short T_2. As correlation time and rotational tumbling increase, substances become more liquid-like and reach the motionally narrowed regime where T_1 is equal to T_2. Note that T_1 reaches a minimum when the correlation time is equal to the inverse of the Larmor frequency but T_2 simply increases with decreasing τ_c. This phenomena is due to the $J^{(0)}(0)$ term in the expression for T_2. To understand this, first consider T_1 and its spectral density function components. Short correlation times make the denominators of the spectral density functions small due to the $\omega^2\tau_c^2$ term, allowing the linear term τ_c to dominate, and long correlation times cause the $\omega^2\tau_c^2$ quadratic term to dominate. These two regimes cause the T_1 minimum. T_2 on the other hand, has the zero frequency spectral density component which causes τ_c to dominate over all frequencies. Figure 1.3 was created using assumptions for dipolar

interactions between a pair of like spins, but Equations 1.7 can be modified to incorporate interactions from more than one spin, interactions between spins from unlike molecules, and effects from interactions other than dipolar. However, the motional features in the plot remain the same regardless [5].

Simple Pulse Sequences

Single-Pulse

The simplest manipulation of the magnetization vector one can perform is the single-pulse experiment. This involves applying a radio frequency pulse to a sample at equilibrium then collecting the resulting voltage response, termed the free induction decay (FID). The pulse time and power are adjusted such that the spins rotate 90 degrees from their original position along the z-axis to the x-y plane [5]. In the x-y plane, the spins precess at their Larmor frequency and de-phase due to T_2 relaxation. Figure 1.4 depicts the sequence.

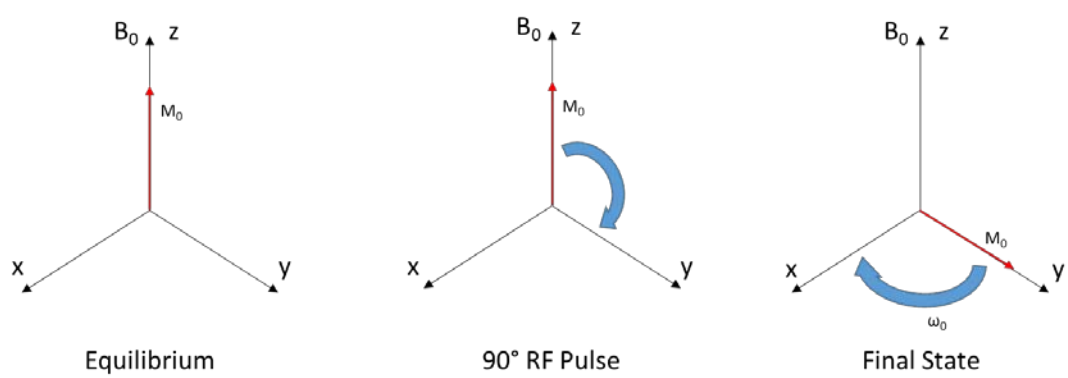

Figure 1.4. Movement of the magnetization vector during a single-pulse experiment

The collected signal that appears on the spectrometer is shown in Figure 1.5.

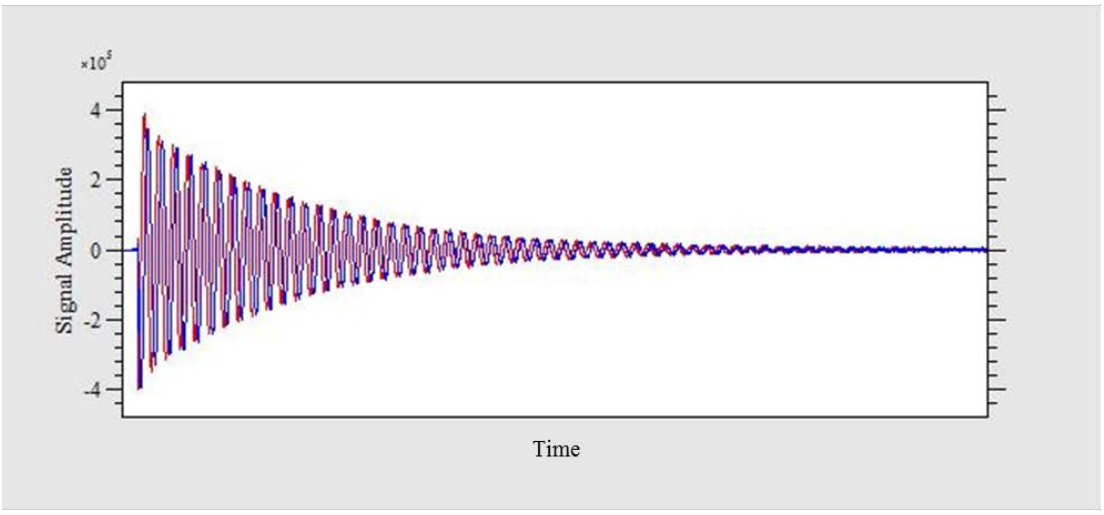

Figure 1.5. Real (blue) and imaginary (red) parts of the FID resulting from a single-pulse experiment

This signal was collected with the reference frame of signal acquisition slightly off-resonance from the Larmor frequency. This is why the sinusoidal component is seen in the decay. Because the signal is collected from both the x and y axes using quadrature detection, it can be decomposed into real and imaginary parts. Clearly, some frequency is inherent in the signal since sinusoidal oscillations are seen so it makes sense that Fourier transforming the signal would give information about frequencies present since Fourier transforms are used to translate between a time and frequency domain. The signal in Figure 1.5 is a multiplication of a sine function (from being off-resonance from the Larmor frequency) with an exponential decay function (from decay due to T_2), thus the Fourier transform is the convolution of a delta function with a Lorentzian. Since this signal oscillates at a single frequency, the Fourier transform would appear as a single Lorentzian shifted slightly from the reference frequency [5].

This single-pulse experiment is useful for shimming and setting parameters such as the offset frequency and the RF pulse duration necessary to flip the spins 180 degrees, but it is quite

simple and doesn't provide much insight into sample dynamics. Two slightly more complex experiments will next be explained.

Inversion Recovery

Recall Equation 1.2 which describes how the z-direction magnetization vector changes with T_1 relaxation. Upon setting M_z equal to zero, it can be determined that $t = 0.6931*T_1$ at that point. This information can be used to apply a pulse sequence to a sample that will allow determination of its T_1 relaxation time constant as shown in Figure 1.6.

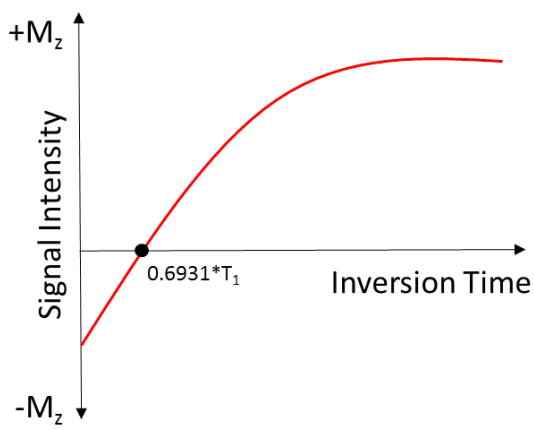

Figure 1.6. Signal collected from an inversion recovery pulse sequence

Upon generating the red curve, T_1 can be easily calculated. The curve is formed by applying a pulse sequence termed inversion recovery [9]. A 180 degree RF pulse is first applied to the sample in order to put the magnetization vector in the –z direction, an inversion time (t_I) allows the magnetization vector to relax due to T_1 and become more positive, then a 90 degree pulse is applied to flip the vector into the transverse plane where signal is acquired. If this process is

repeated several times with a varied t_I, the signal intensity can be plotted versus the inversion time, the red curve in Figure 1.6 formed, and T_1 calculated [5].

As shown in Figure 1.3, the T_1 of a sample gives information about its structure. A sample with a short T_1 tends to be more liquid with high mobility; conversely, a sample with a long T_1 tends to be crystalline with low mobility. Diamonds have a T_1 on the order of days, and free water has a T_1 of approximately one second [5].

CPMG Train

T_2 is also a useful parameter to characterize systems and can be found with a simple pulse sequence called a CPMG (Carr-Purcell-Meiboom-Gill) train [12]. First, a 90 degree pulse is applied to bring the magnetization vector into the transverse plane. Next, a series of evenly-spaced 180 degree pulses are applied. In between the 180 degree pulses, a spin echo forms because the 180 degree pulses "refocus" the magnetization after dephasing due to T_2* effects. In order to understand this, imagine runners on a circular racetrack beginning in different lanes. They run for some amount of time then are signaled to turn around and run back for an equal amount of time. During the race, they run at slightly different paces and for slightly different distances since those in the inner lanes have a shorter path than those in the outer lanes, but they all finish together at the starting point. Just as the runners began together but quickly separated due to pace and path differences, spins are in phase immediately after they are flipped into the transverse plane but quickly de-phase due to magnetic field inhomogeneity. The signal that tells the runners to reverse direction correlates to the first 180 degree pulse in the CPMG train. After the pulse, the spins change precession direction and begin to re-phase. They become entirely coherent after the echo time denoted as 2τ, and an echo is collected [13].

This process of letting the spins de-phase then re-phasing them with a 180 degree pulse is repeated many times. The echo amplitude decreases as more 180 degree pulses are applied due to pure T_2 relaxation which is caused by molecular interactions and cannot be re-phased. The relaxation due to inhomogeneity in the magnetic field is refocused over timescales greater than τ. Figure 1.7 illustrates the experiment in the form of a timing diagram. The top line displays which RF pulses are used and the times between them, and the second line shows where signal is collected.

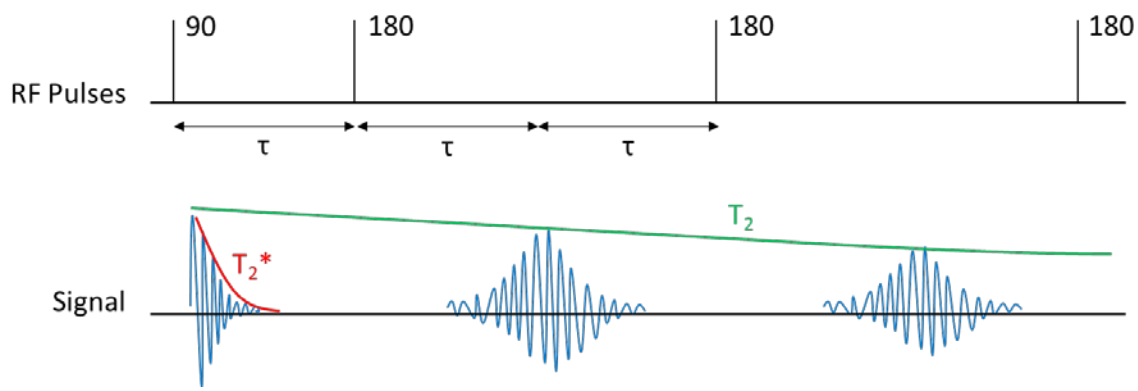

Figure 1.7. The RF pulses and resulting signal of a CPMG train

To analyze the data collected from the pulse sequence, Equation 1.3 is fit to the green exponential decay curve and the time constant T_2 found.

Consider again Figure 1.3. Crystalline structures have short T_2's since molecules have strong dipolar coupling and quickly lose phase coherence. Longer T_2's pertain to liquids with more mobility. Diamonds have T_2 values on the order of nanoseconds, and free water has a T_2 approximately equal to its T_1 on the order of a second [5].

PGSE Experiment

To measure translational motion, the pulsed gradient spin-echo (PGSE) experiment is used. The PGSE sequence encodes for translational movement of spins by generating a phase shift at a designated time then unwrapping the phase shift at a later time to determine how far spins moved during the interval [14]. This provides diffusion information due to random motion dephasing the signal. It is slightly more complex than the inversion recovery and CPMG train sequences because gradients are applied to generate phase shifts of spins. The theory behind this concept will be explored in a later section. For now, the focus will be on the pulse sequence. The RF pulses, gradients, and signal of a PGSE sequence are shown in Figure 1.8.

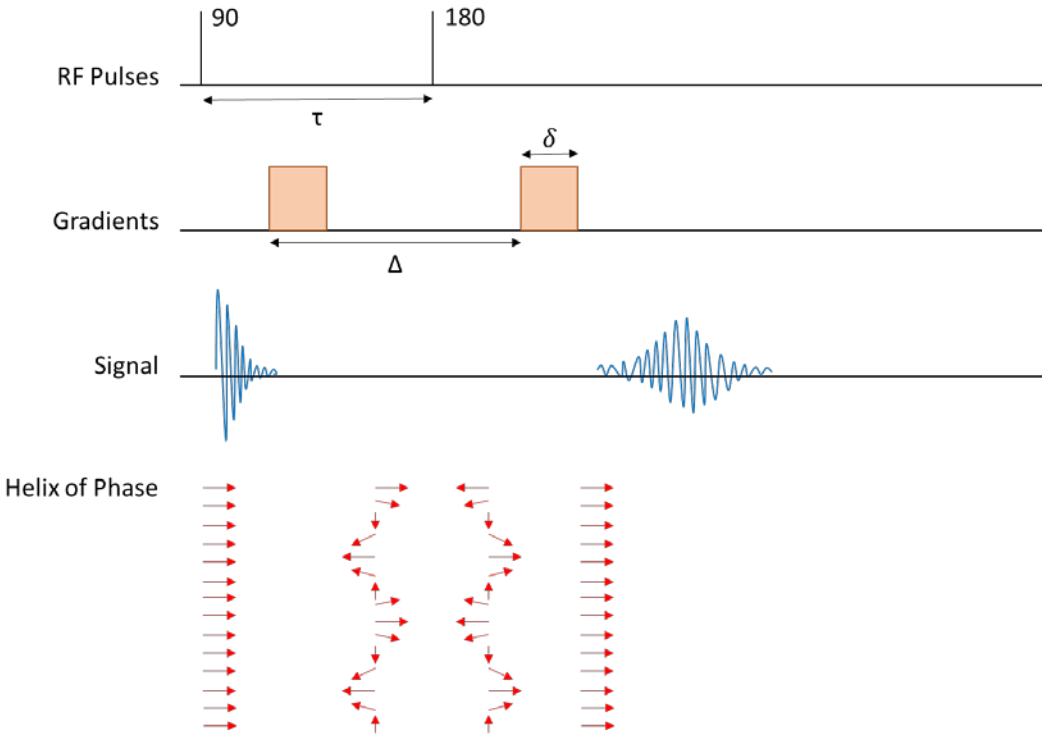

Figure 1.8. The PGSE pulse sequence winds up helices of phase using gradients.

The red arrows in the figure represent spins and their phases and illustrate how phase changes over time [5]. The sequence begins with a 90 degree RF pulse which puts the magnetization in the transverse plane and generates a FID. At this stage, the spins all have the same phase. Next, a gradient pulse of duration δ is applied to wind up a helix of phase, encoding the position of each spin by making the phase a function of position. The gradient does this by causing the B_0 field to change linearly over the direction of the applied gradient. Since phase or frequency is a function of magnetic field strength, this is how the gradient pulse makes phase position-dependent. The 180 degree pulse reverses phase precession so that the next gradient pulse (also of duration δ) unwinds the helix and re-phases the spins. This re-phasing causes an echo to form as previously demonstrated with the runners on a track analogy [5]. How does this give diffusion information? The phase in Figure 1.8 at the end of the experiment represents spins that did not diffuse or move in any way during the experiment. Consider now the green molecule in Figure 1.9 that diffuses from position z_1 to z_2 during time Δ.

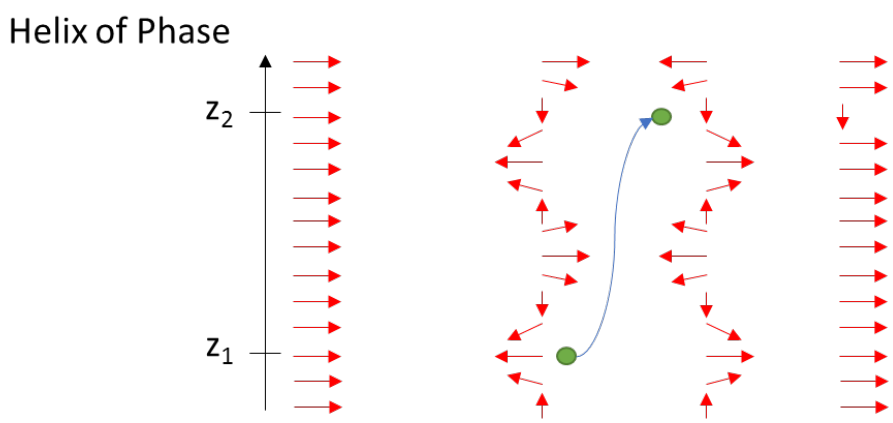

Figure 1.9. A diffusing spin causes a phase shift.

Note that the arrows in the fourth column which represent the phase at the end of the sequence contain a residual phase shift due to the movement of the diffusing molecule. Of course, a real sample would have a great deal more moving spins and therefore a significant random distribution of motion phase shift due to diffusive motion. This randomization of phase is detected as an attenuation of the collected signal as a function of gradient strength, and the data from this experiment can be analyzed to find a diffusion coefficient of moving molecules. Δ is termed the displacement observation time and can be varied to explore the movement of molecules over a range of time scales limited by relaxation effects [5].

In summary, the PGSE experiment provides data on diffusing spins by encoding them with a gradient that gives their phase a position dependence then checking for movement after a displacement observation time by applying a gradient that unwinds the phase helix. If no spins moved during the observation time, the spins will all have the exact same phase at the end of the experiment. If diffusion occurred, there will be a residual phase shift that reflects the random motion and causes an attenuation of the collected signal. The full theory and data analysis will be delved into during a later section of this thesis.

Phase Cycling

Since NMR deals with a huge number of spins in a spatially finite sample, it is inevitable that some spins will not see an exact RF and gradient pulse amplitude applied to the sample during a pulse sequence. This issue can lead to coherent noise and consequently signal that does not accurately represent the data one hoped to acquire. Phase cycling is a technique that solves this problem and is implemented in nearly every pulse sequence written. To phase cycle an experiment such as that shown in Figure 1.7 or Figure 1.8, the sequence is repeated many

times with the phase of the RF pulses varied for each repetition [15]. In this way, the spins are forced through a pathway that cancels out unwanted signal and leaves only spins that have been encoded by the desired pulse sequence correctly.

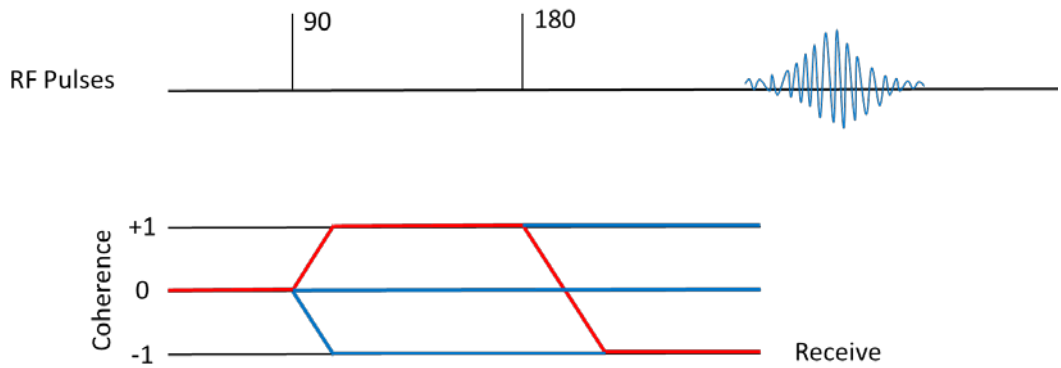

Figure 1.10. Different coherence pathways of the Hahn echo sequence. The red path is desirable [16].

The experiment depicted in Figure 1.10 is called the Hahn echo sequence [13], but it is an arbitrary sequence for the purpose of our current discussion. These concepts can be applied to any series of pulses. In the ideal coherence path (red), the 90 degree pulse gives the spins a coherence of +1, the 180 degree pulse brings them to a coherence of -1, and the signal is received on the -1 coherence. Note that there are several undesirable coherences (blue) by the end of the pulse sequence. Using some simple math and phase knowledge, a phase cycle that selects for the desirable red path can be calculated [16].

For many of the experiments used in this thesis, 16 step phase cycles that require 16 loops of a pulse sequence were used. Because of this, sequences had to be run in multiples of 16 to acquire averages, *e.g.* an experiment would loop through its RF pulses a total of 64 times

in order to obtain 4 data sets to be averaged. This can be time consuming, but phase cycling is necessary.

The Bloch Equations

In 1946, Felix Bloch put forth the following macroscopic equations to describe the evolution of the magnetization vector over time [17]:

$$\frac{dM_x}{dt} = \gamma M_y \left(B_0 - \frac{\omega}{\gamma}\right) - \frac{M_x}{T_2} \tag{1.8}$$

$$\frac{dM_y}{dt} = \gamma B_1 - \gamma M_x \left(B_0 - \frac{\omega}{\gamma}\right) - \frac{M_y}{T_2}$$

$$\frac{dM_z}{dt} = -\gamma M_y B_1 - \frac{M_z - M_0}{T_1}$$

These equations account for spin relaxation, nutation, and precession. The expressions for M_x and M_y contain the T_2 time constant since T_2 relaxation affects only the magnetization in the transverse plane, and the M_z expression is dependent upon the T_1 time constant since T_1 relaxation pertains to relaxation along the z-axis (the direction of the B_0 field). Note that the M_x and M_y expressions contain a $\left(B_0 - \frac{\omega}{\gamma}\right)$ term which accounts for the difference between the Larmor frequency and the reference frequency, ω. This causes sinusoidal behavior in the magnetization vectors over time as seen in Figure 1.5 [5].

The Bloch equations are valuable because they provide a way to calculate the macroscopic magnetization vector evolution as a function of time when T_1 and T_2 relaxation are present. They can be used for writing pulse sequences, predicting signal behavior, and generally providing a great deal of insight into NMR processes.

Equipment

The data in this thesis was acquired using the equipment in the College of Engineering Magnetic Resonance Laboratory at Montana State University Bozeman. The Bruker 250 MHz superconducting magnet shown in Figure 1.11 was utilized along with a special high power RF probe made by Bruker and the data collection software package TopSpin 3.2.

Figure 1.11. The 250 MHz superconducting magnet used for experiments in this thesis

The high power RF probe, which is the first of its kind, proved invaluable for attaining the rapid timing between RF pulses required to capture short, approximately 10 µs T_2 domains inherent in polymer compounds. It contains a 5 mm permanently attached RF coil and allows for easy temperature control with the Bruker temperature control unit. The samples in the probe can be

safely heated up to 60°C, a temperature that allowed data collection on thermally gelled polymer samples, and down to -20°C for glass transition studies. Table 1.1 displays the shortest time parameters possible for a two-dimensional relaxation experiment (see Chapter 2 for details) on the high power probe along with any calculations necessary to find the values. Notice that the probe can achieve a remarkably short 90° pulse time around 4 µs, a duration typically associated with solid state NMR probes.

Name in TopSpin	Parameter	Shortest Value	Method of Determination
DW [µsec]	Dwell Time	0.4	= 1/24*Tau
D3 [sec]	Tau	0.0000096	= DW*24
D4 [sec]	Delay	0.0000004	= D6 = DW
D6 [sec]	Delay	0.0000004	= D4 = DW
TD	Time Domain Size	Calculate	$= \frac{2*L22*Tau+D4+D6+del32}{DW}$
P3 [µsec]	90° Pulse Time	~ 4 (Find)	= 2*P4
P4 [µsec]	180° Pulse Time	~ 8 (Find)	Find in zg scan
PldB1 [dB]	Pulse Power	-20	Max power possible

Table 1.1. Shortest parameters possible for a 2D relaxation experiment on the high power probe which allow for T_2's as short as 10 µs to be resolved. Tau is the time between application of RF pulses in a CPMG train.

Another essential component to this research was the diff30 gradient set. Its maximum gradient value is 17.82 T/m at 60 Amps, a parameter that allowed diffusion information to be collected from even solid-like polymer samples.

ADVANCED NMR CONCEPTS

The following sections will cover details of two advanced NMR concepts relevant to this thesis, diffusometry and 2D relaxometry.

Diffusometry

Diffusion data was collected as one method to measure the micro and mesoscale dynamics of the samples discussed in this thesis. NMR can be utilized to track spins as they undergo translational motion and diffusion. The pulse sequence used here that gives information regarding molecular displacement is called the pulsed gradient spin-echo (PGSE) experiment and is shown here again in Figure 2.1 [5]. Notice that an echo forms at 2τ, a displacement encoding time Δ occurs between the gradient pulses, and the pulses are of a duration δ.

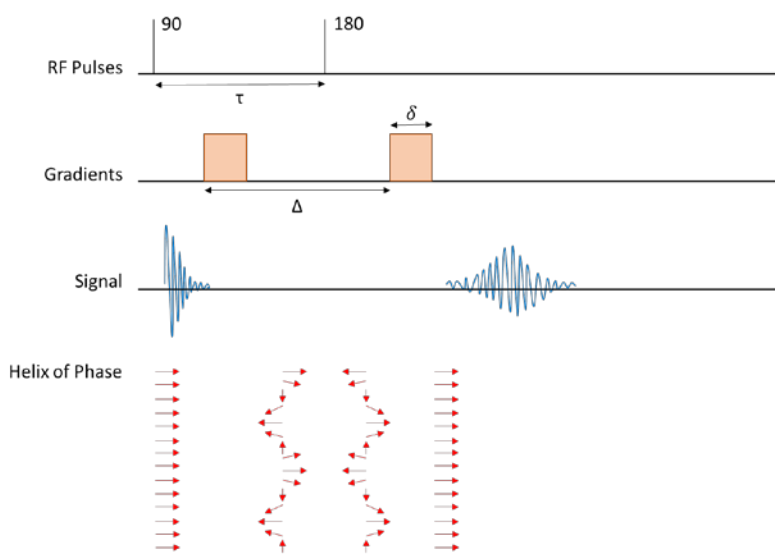

Figure 2.1. The PGSE experiment and the phase of spins through the gradient and RF pulses

This pulse sequence gives the phase of the spins a dependence on displacement and therefore allows measurement of their motion. The linear gradients cause the magnetic field to vary as a function of position.

$$\omega_0(\boldsymbol{r}) = \gamma B_0 + \boldsymbol{r} \cdot \boldsymbol{G} \tag{2.1}$$

As shown by Equation 2.1, spins at different positions have a unique Larmor frequency. Thus a gradient pulse results in a phase shift of some angle which is dependent upon location. For one spin *j* in location $\boldsymbol{r}_j$, the phase shift experienced at time *t* in a gradient ***g*** is given by Equation 2.2.

$$\emptyset_j(t) = \gamma \int_0^t \boldsymbol{g}(t') \cdot \boldsymbol{r}_j(t') dt' \tag{2.2}$$

This simple equation does not account for RF pulses (which also affect phase), so it will be helpful to define an "effective gradient" ***g*(t)*** to further analyze the PGSE sequence. ***g*(t)*** possesses the actual sign of the magnetization by taking into consideration all RF pulses which change the sign of the phase. Figure 2.2 displays the PGSE pulse sequence with a ***g*(t)*** line. The first gradient pulse is inverted because the 180° pulse directly following it effectively reverses the phase sign [5].

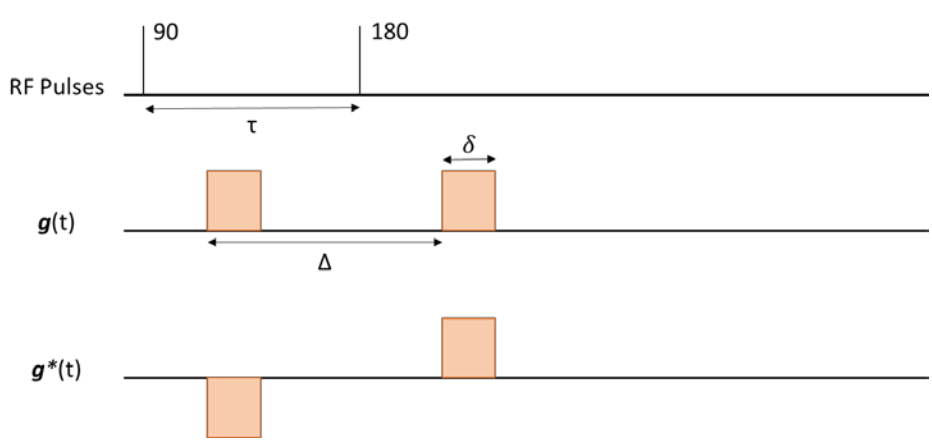

Figure 2.2. The effective gradients consider changes in phase sign due to RF pulses.

Now that these effective gradient values have been established, it is clear that the first gradient pulse shifts the phase of the spins by $\gamma\delta\boldsymbol{g}\cdot\boldsymbol{r}$ (from Equation 2.2), then the second equal but opposite pulse "undoes" that change after time Δ. Because the accumulated phase is proportional to the displacement of the spins along the z-axis when the gradients are applied in the z-direction, the phase changes take the form of a helix as shown in Figure 2.1. It can be said that the first gradient pulse of the PGSE sequence winds up a helix of phase then the second unwinds it [5].

How does this winding and unwinding of phase reveal diffusion information? If the spins are completely stationary during Δ, a perfectly refocused echo will form after the two gradient pulses in the PGSE experiment because the spins will be exactly in phase. However, consider the situation in Figure 2.3 where a spin has translationally moved from position z_1 to z_2 during the experiment.

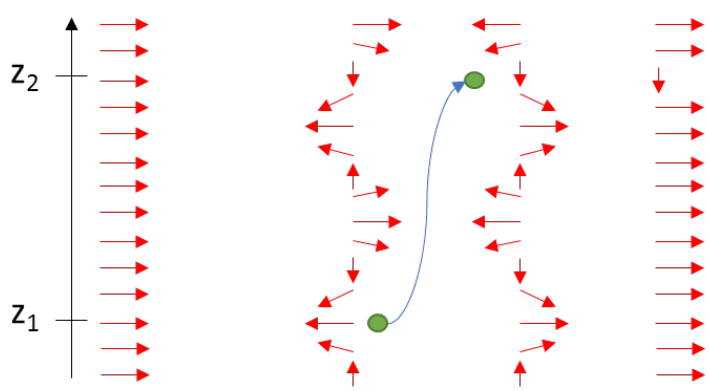

Figure 2.3. A spin moves from position z_1 to position z_2 during Δ, causing a phase shift.

Now there is a phase shift in this moving spin's contribution to the echo. Of course, many spins diffuse during the experiment rather than only one, and the net phase shift caused by their movement is given by Equation 2.3.

$$\emptyset_{shift} = \gamma\delta\boldsymbol{g} \cdot (\boldsymbol{r}' - \boldsymbol{r}) \tag{2.3}$$

Here ***(r′ – r)*** represents the dynamic displacement. It must be noted that Equation 2.3 and the following equations of this analysis assume that no motion occurs during the time of the gradient pulses, δ. This assumption is valid for $\delta \ll \Delta$, a condition that holds for all experiments in this thesis [5].

In order to understand the effects of this net phase shift caused by diffusive movement on the collected signal, it is helpful to return to the Bloch Equations (Equation 1.8). Upon solving these equations for the evolution of the magnetization as a function of time, an expression for the amplitude of the echo at its center, *E(t)*, can be obtained. The result is shown in Equation 2.4 [18].

$$E(\boldsymbol{g}) = \exp\left[-D\gamma^2 \int_0^t \left(\int_0^{t'} \boldsymbol{g}^*(t")\, dt"\right)^2 dt'\right] \exp\left[i\gamma\boldsymbol{v} \cdot \int_0^t \left(\int_0^{t'} \boldsymbol{g}^*(t")dt"\right) dt'\right] \tag{2.4}$$

In this equation, *D* represents the diffusion coefficient of the substance investigated, and ***v*** represents the velocity vector. The effective gradient is applied so the equation accounts for RF pulses. The integrals in this equation can be calculated for the PGSE sequence using the time sequence of the applied gradients. First, Equation 2.5 must hold in order for an echo to form at time 2τ [5]. Because of its two equal and opposite gradient pulses, the PGSE experiment clearly fulfills this requirement.

$$\int_0^{2\tau} \boldsymbol{g}^*(t')dt' = 0 \tag{2.5}$$

Next, the double integral in the second exponential of Equation 2.4 can be reduced to

$$\int_0^t \left(\int_0^{t'} \boldsymbol{g}^*(t")dt" \right) dt' = -\boldsymbol{g}\delta\Delta \tag{2.6}$$

Finally, the result in Equation 2.6 can be used to find the first double integral in Equation 2.4 [14].

$$\int_0^t \left(\int_0^{t'} \boldsymbol{g}^*(t")dt" \right)^2 dt' = \boldsymbol{g}^2\delta^2 \left(\Delta - \frac{\delta}{3} \right) \tag{2.7}$$

With these results, Equation 2.4 reduces to the more tractable expression shown in Equation 2.8 for the PGSE experiment.

$$E(\boldsymbol{g}) = \exp\left[-D\gamma^2 \boldsymbol{g}^2 \delta^2 \left(\Delta - \frac{\delta}{3} \right) \right] \exp[i\gamma \boldsymbol{v}\boldsymbol{g}\delta\Delta] \tag{2.8}$$

From this equation, it can be seen that diffusion causes an attenuation of signal, and velocity causes a phase shift. When $\boldsymbol{v}$ = 0 as it will for the experiments in this thesis, Equation 2.8 returns the well-known Stejskal-Tanner relation displayed in Equation 2.9 [14].

$$E(\boldsymbol{g}) = \exp\left[-D\gamma^2 \boldsymbol{g}^2 \delta^2 \left(\Delta - \frac{\delta}{3} \right) \right] \tag{2.9}$$

The exponent in this equation is proportional to the mean-squared displacement of the spins over the timescale $\left(\Delta - \frac{\delta}{3} \right)$. Therefore, all experimental times are fixed when this sequence is run and the normalized signal on a log scale is plotted vs $\gamma^2 \boldsymbol{g}^2 \delta^2 \left(\Delta - \frac{\delta}{3} \right)$ as shown in Figure 2.4 so the slope of the line yields the self-diffusion coefficient of the sample.

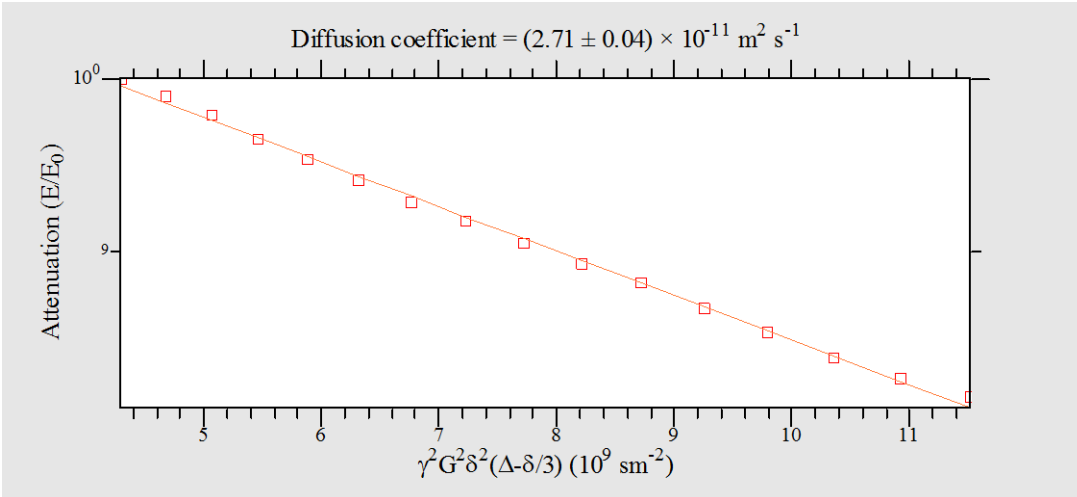

Figure 2.4. Stejskal-Tanner plot of PGSE data. The slope of the line is equal to the self-diffusion coefficient (D = (2.71±0.04) x 10^{-11} m^2/s) of the material, in this case a polymer.

In this figure, each point represents echo data from a different gradient value as the PGSE sequence is run with incremental gradient values, and the attenuation arises from phase incoherence generated by the random diffusive motions of the spins. Many of the experiments in this thesis are run on samples that contain multiple components such as polymer and water. It is therefore important to note that the entire echo is collected during this sequence which allows for spectral resolution. The raw data is Fourier transformed into the frequency domain where the spectra can be seen and one peak can be selected for by integrating over it and excluding all others. Figure 2.5 displays the spectrum for a polymer/water sample at one gradient step of a PGSE sequence. The peak pertaining to water is located on the left and that from polymer is positioned on the right.

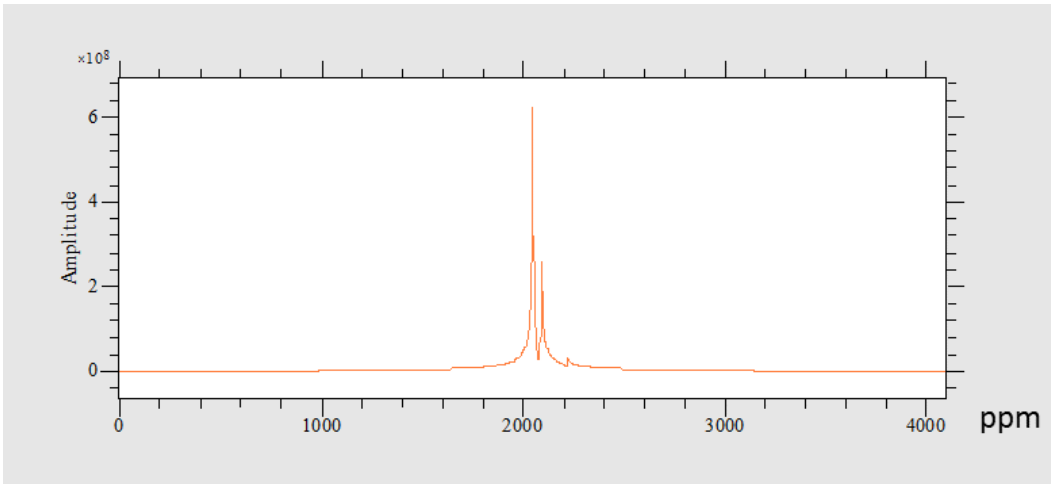

Figure 2.5. Two peaks arising from water and polymer are seen because the PGSE experiment allows for spectral resolution.

To obtain diffusion data on a specific peak, one would integrate over that peak to investigate its attenuation, then form the Stejskal-Tanner plot with that data on the y-axis.

To summarize, the PGSE sequence checks the position of spins by winding up a helix of phase, waits for a time Δ, and then unwinds the helix to determine if spins have moved during the observation time. Diffusion causes phase incoherence which leads to an attenuation of signal, and that attenuation can be quantified to yield a self-diffusion coefficient.

In order to further grasp how the PGSE sequence conveys information about translational motion, the concepts of propagators [19] and *q*-space [20] will be explored. A propagator is simply a probability distribution that describes the chance that a molecule or particle spin will move some specified distance from position ***r*** to ***r'*** over a certain amount of time Δ. For free water which undergoes random Brownian motion [21], the propagator is a Gaussian distribution with its maximum at zero because the molecules will have no net average displacement over time Δ, but a few spins will diffuse some distance. The relevant propagator

for the PGSE experiment represents the conditional probability for a spin to move from position $\boldsymbol{r}$ to $\boldsymbol{r}'$ during Δ and is written $P(\boldsymbol{r}|\boldsymbol{r}',\Delta)$. Because NMR is averaged over all molecules whose spin magnetization is properly encoded, the propagator must be multiplied by the molecular density function, $\rho(\boldsymbol{r})$, of the NMR active spins in a sample. The probability measured then becomes $\rho(\boldsymbol{r})P(\boldsymbol{r}|\boldsymbol{r}',\Delta)$ [5]. To acquire an expression for echo amplitude using these ideas, this probability is used to weight each phase term in an ensemble average as shown in Equation 2.10.

$$E(\boldsymbol{g},\Delta) = \int \rho(\boldsymbol{r}) \int P(\boldsymbol{r}|\boldsymbol{r}',\Delta)\exp(i\gamma\delta\boldsymbol{g}\cdot[\boldsymbol{r}-\boldsymbol{r}'])\,d\boldsymbol{r}'d\boldsymbol{r} \tag{2.10}$$

This expression says that the signal of the PGSE experiment is equal to the sum of all phase shifts due to spins diffusing from their initial position $\boldsymbol{r}$ to $\boldsymbol{r}'$ during the displacement observation time Δ. To describe the space in which this diffusion data is sampled, it is logical to define the reciprocal space $\boldsymbol{q} = (2\pi)^{-1}\gamma\delta\boldsymbol{g}$ (units of m^{-1}) [20]. As the experiments step through higher and higher gradient values, the data goes farther out in *q*-space. Equation 2.10 can now be written using new notation.

$$E(\boldsymbol{q},\Delta) = \int \rho(\boldsymbol{r}) \int P(\boldsymbol{r}|\boldsymbol{r}',\Delta)\exp(i\boldsymbol{q}\cdot[\boldsymbol{r}-\boldsymbol{r}'])\,d\boldsymbol{r}'d\boldsymbol{r} \tag{2.11}$$

In the interest of elucidating an important relationship, a few more simplifications can be applied to Equation 2.11. The distribution defined in Equation 2.12 is known as an average propagator and represents a sum over all possible start positions with $\boldsymbol{R} = \boldsymbol{r}' - \boldsymbol{r}$:

$$\overline{P}(\boldsymbol{R},t) = \int \rho(\boldsymbol{r})\ P(\boldsymbol{r}|\boldsymbol{r}+\boldsymbol{R},t)d\boldsymbol{r} \tag{2.12}$$

This definition allows Equation 2.11 to be written as [19]

$$E(\boldsymbol{q},\Delta) = \int \overline{P}(\boldsymbol{R},\Delta)\exp(i\boldsymbol{q}\cdot\boldsymbol{R})\,d\boldsymbol{R} \tag{2.13}$$

It is clear from Equation 2.13 that there is a Fourier relationship between $E(\boldsymbol{q},\Delta)$ and $\overline{P}(\boldsymbol{R},\Delta)$. This can be interpreted by realizing that the PGSE sequence essentially images the propagator by probing dynamic displacement space; a great deal of information regarding molecular dynamics can be gathered from acquiring data in *q*-space [5, 22].

A final note must be made on the low *q* limit. Notice in Figure 2.4 that the signal was only allowed to attenuate approximately 20%, and that the points collected remain in the low *q* region relevant to the large displacement limit. The reason behind this analysis can be understood by doing an expansion on $E(\boldsymbol{q},\Delta)$ around $\boldsymbol{q}$. The first linear term falls out for any motion with no net flow because the term is related to mean displacement and leaves the approximation [5]

$$E(\boldsymbol{q},\Delta) \approx 1 - \frac{1}{2}q^2\langle Z^2(\Delta)\rangle \tag{2.14}$$

where *q* is the magnitude of $\boldsymbol{q}$ and *Z* is the projection of $\boldsymbol{R}$ along $\boldsymbol{q}$. When the low *q* signal is plotted against q^2, the initial decay is linear (as in Figure 2.4) and allows for direct measurement of mean squared displacement, $\langle Z^2(\Delta)\rangle$. Because mean squared displacement is related to the self-diffusion coefficient via the Einstein relation [23], Equation 2.14 again shows how *D* can be acquired from PGSE data.

2D Relaxometry

The first chapter of this thesis discussed the concepts of T_1 and T_2 along with the pulse sequences used to determine their values. In this section, methods to measure the correlation of these relaxation time constants will be described. In polymer/solvent systems, a hierarchy of

dynamics exists in which both solid and liquid dynamics are present. For example, consider a system of polymer in acetone. The polymer molecules themselves are fairly rigid, and solvent molecules very close to a polymer backbone or arm exhibit different mobility characteristics than do free solvent molecules. A two-dimensional experiment which correlates one relaxation time to another allows these differing domains to be resolved. In this way, valuable microstructure information is revealed.

T_1-T_2 Correlation

First, this thesis will examine the sequence shown in Figure 2.6 which relates T_1 and T_2 called the T_1-T_2 correlation pulse sequence [24, 25].

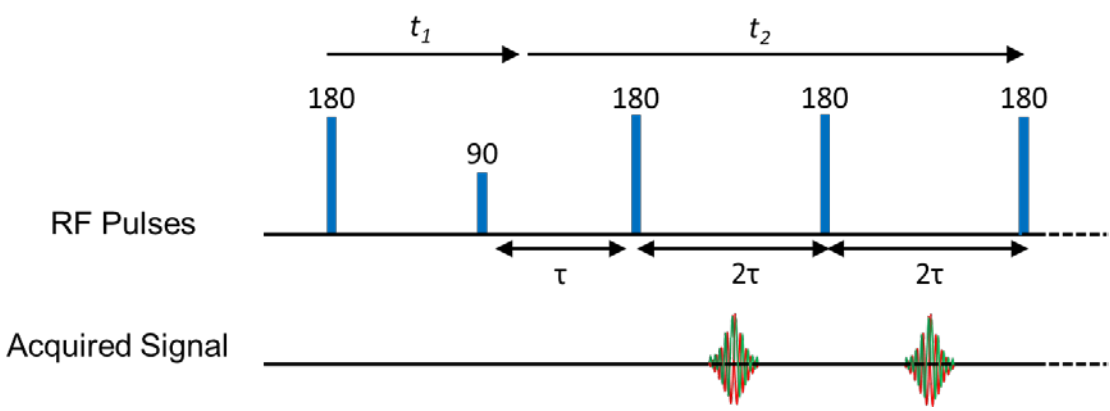

Figure 2.6. The T_1-T_2 correlation pulse sequence allows for resolution of domains with different relaxation constants [26].

The sequence consists of two time intervals, t_1 and t_2. During the first interval, a 180 degree RF pulse flips the magnetization vector along the negative z-axis, an inversion time (t_1) passes, and then the magnetization is flipped 90 degrees into the transverse plane. Notice that this arrangement is the same as that in the inversion recovery sequence discussed in Chapter 1; in

this way, the T_1-T_2 pulse sequence encodes for T_1 relaxation in the first time interval. The second time interval pertains to the encoding of T_2 relaxation. Since the 90 degree pulse at the end of t_1 left the magnetization in the transverse plane, a CPMG train can be immediately run to obtain T_2 data. The signal acquired at the end of the sequence therefore contains information regarding both T_1 and T_2 in two independent dimensions. The normalized signal is written as

$$S(t_1, t_2) = \iint (1 - 2\exp(-R_1 t_1))\exp(-R_2 t_2) f(R_1, R_2) dR_1 dR_2 \tag{2.15}$$

where t_1 and t_2 are as shown in Figure 2.6, R_1 and R_2 refer to the relaxation rates T_1^{-1} and T_2^{-1} respectively, and $f(R_1, R_2)$ is the continuous relaxation-spectru m density [5].

The data from this experiment is multi-exponential so it is logical to use an inverse Laplace transform (ILT) to derive distributions of time constants from it. Unfortunately, the ILT (shown in Equation 2.16) is asymmetric, ill-defined, and virtually impossible to implement exactly on the 2D data set which results from the T_1-T_2 sequence.

$$f(R) = \mathcal{L}^{-1}\{S(t)\} \tag{2.16}$$

$$S(t) = \mathcal{L}\{f(R)\} = \int_0^\infty f(R)\exp(-Rt)\, dR$$

For the data in consideration, $f(R)$ represents the probability of finding a relaxation time constant R, and $S(t)$ can be thought of as the time domain signal. Despite its difficulties, the ILT can be executed using a special approach [27, 28]. This method uses a pre-specified window of values, the requirement that an optimal, minimum mean-squared error solution be reached, and parsimony [29]. The principle of parsimony is elegantly implemented using Tikhonov regularization. If this is done using a smoothness operator that involves the curvature of $f(R)$, one reaches the expression in Equation 2.17.

$$V(\alpha) = \sum_{i}^{N}\sum_{j}^{M}\left(S_i - \exp\left(-t_i R_j\right) f_j\right)^2 + \alpha^2 \sum_{j}^{M}\left(2f_j - f_{j+1} - f_{j-1}\right)^2 = Minimum \qquad (2.17)$$

where $V(\alpha)$ is the minimum mean-squared error numerical solution to the ILT, α is a smoothing parameter, S_i is an element of the signal vector that corresponds to a time value t_i, R_j is a discrete relaxation rate, and the solution vector ***f*** (the spectrum of relaxation rates) has elements f_j corresponding to each R_j. Notice that the last term contains an approximation to the second derivative of $f(R)$. This is where the smoothness operator is involved. Before the minimization algorithm is performed, a value for α is chosen such that the residual (the first term in Equation 2.17) is minimized, but only just. *N* and *M* are also chosen *a priori* in order to define a window for the solution.

The algorithm described above presents a solution for a one-dimensional data set, but recall that the T_1-T_2 correlation sequence data is two-dimensional and contains two relaxation rates. Fortunately, the process can be implemented in the same way once the 2D data has been prepared [30]. The dimensions of the matrices are first reduced by singular value decomposition, then the smaller matrices are projected as vectors, and the solution in Equation 2.17 is obtained. The resulting solution is organized into the desired 2D array form.

This process was implemented for the data in this thesis using a Matlab code provided by the late Professor P.T. Callaghan [31]. Figure 2.7 presents the interface in which raw data can be loaded and inverted; the relevant sections are highlighted in red.

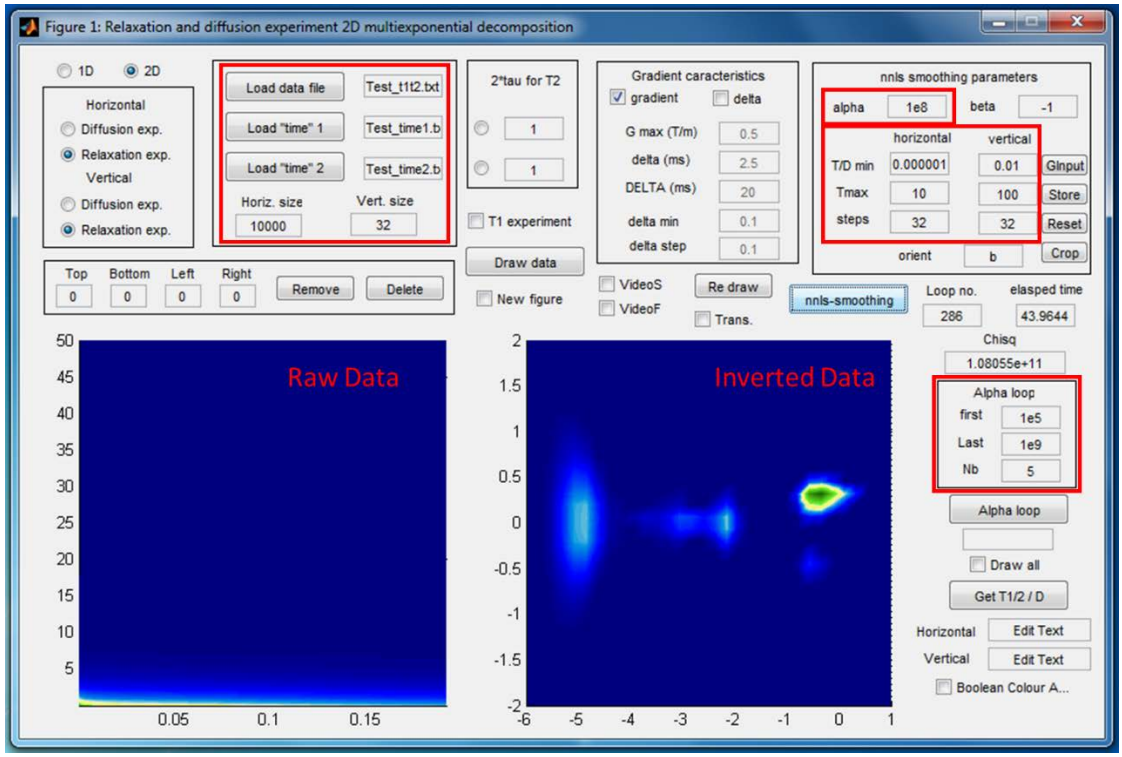

Figure 2.7. The 2D inverse Laplace transform algorithm is employed using a Matlab code which presents an interface where parameters can be defined [31].

Raw data is loaded using the box on the top left then represented as a 2D surface plot in "Raw Data." At the top right, α and the desired window (horizontal and vertical limits) are specified before the inversion algorithm is run. To determine α, the user runs the "Alpha loop" box on the right hand side over a range of values then selects the optimal one. Once the data is loaded and the parameters set, the inversion is achieved and its results are displayed in the "Inverted Data" window. It is shown in 2D surface plot form, but a more usable contour plot that clearly displays distributions of time constants such as that shown in Figure 2.8 can be generated.

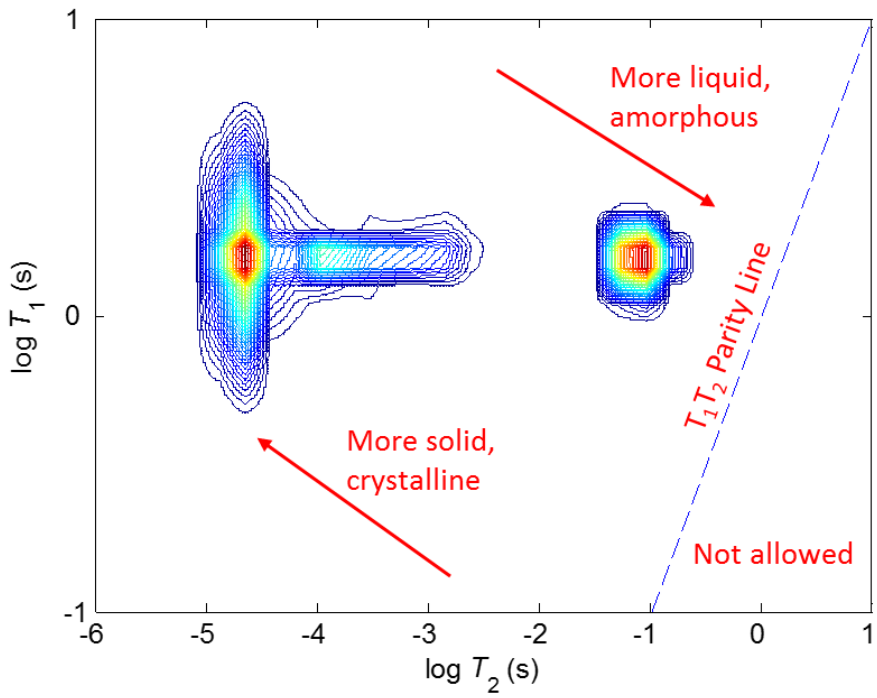

Figure 2.8. The T_1-T_2 contour map generated from an ILT of T_1-T_2 correlation sequence data provides considerable insight concerning the microstructure of samples. Data for an HPMCAS/acetone system provided as an example. The contour intensity (red highest) indicates the proportion of hydrogen spins in the sample with that magnetic relaxation behavior.

The contour plot contains T_2 on the x-axis, T_1 on the y-axis, and shows several signal domains corresponding to different T_1 and T_2 values. Because T_2 can never be greater than T_1, the parity line ($T_1 = T_2$) is delineated as a dashed line in Figure 2.8 and populations below that line cannot be real. Notice how T_2 is correlated to T_1. It is known that three populations of different T_2's exist in this sample, but the distribution of T_1 values associated with each of those populations is also apparent. This is the strength of the T_1-T_2 correlation pulse sequence. The data shown in Figure 2.8 is from a sample that consists of the polymer HPMCAS and acetone. Recall from Chapter 1 that longer T_2 values correspond to populations of high mobility liquid-like domains, while shorter T_2 values are associated with amorphous, glass-like domains [5]. Using this

knowledge, the populations revealed from the ILT can be ascribed to domains of different dynamics in the sample. The population with the longest T_2 in Figure 2.8 must correspond to free acetone molecules, the spins with the highest mobility. The one with the shortest T_2 arises from protons on solid-like polymer molecules. The wide T_1 distribution in this low T_2 polymer population arises from the fact that different sections of the polymer have slightly different mobilities; side chains are more mobile than the backbone. Finally, the middle population corresponds to acetone molecules that have lesser mobilities than do free acetone spins because they are highly associated with the polymer. This thesis will later explore how T_1-T_2 maps can be used to study polymeric sample dynamics over a range of times, temperatures, and compositions.

<u>T_2-T_2 Correlation</u>

Just as T_1 can be correlated to T_2, T_2 can be correlated to itself in the T_2-T_2 correlation pulse sequence shown in Figure 2.9 [32].

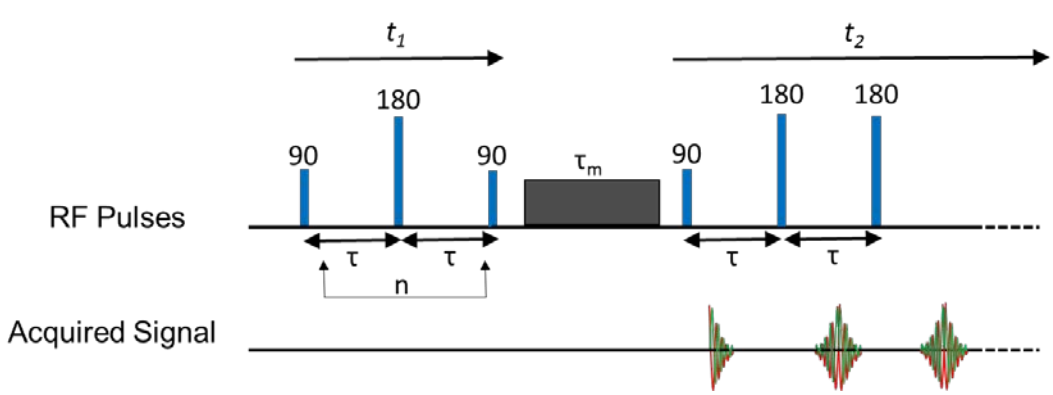

Figure 2.9. The T_2-T_2 correlation pulse sequence measures when spins translationally diffuse from one domain to another [26, 33].

This experiment consists of a first time interval (t_1) with a CPMG train which encodes for T_2, a variable mixing time (τ_m), then a second time interval (t_2) that also contains a CPMG train. With these pulses, the experiment measures T_2 values both before and after the spins are permitted to translationally diffuse during the mixing time [32]. This sequence generates a two-dimensional data set. The data is inverse Laplace transformed in the same manner as the T_1-T_2 correlation sequence data to yield a contour map having T_2 on both the x and y axes. In order to understand the value of this information, consider the simplified model shown in Figure 2.10 which contains a small domain or pore B, next to a larger domain or pore A. The grey packet of spins resides in the model and can diffuse from one domain to the other.

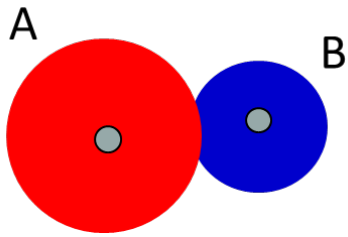

Figure 2.10. A theoretical material with a large domain and a smaller domain between which spins can diffuse [26]

Consider the results of conducting the T_2-T_2 correlation experiment on this model using a mixing time much shorter than the time it takes molecules to diffuse from one domain or pore to the other. The resultant T_2-T_2 contour map shows two populations – one with a short T_2 value corresponding to domain B and one with a longer T_2 value arising from population A. Because of the short mixing time, the T_2 value found in t_1 is the same as that encoded for in t_2, so both populations lie on the diagonal as portrayed in Figure 2.11. The time constants determined

from the data in the second encoding period are labelled T_2' to differentiate from those found in the first interval.

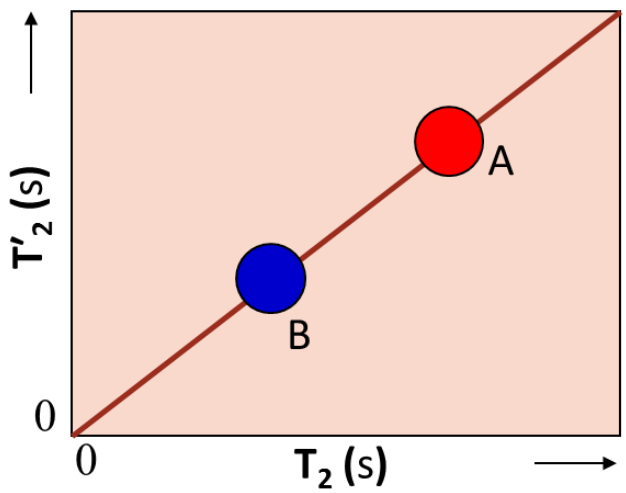

Figure 2.11. The theoretical map from a T_2-T_2 experiment run with a short mixing time displays two populations on the diagonal [26].

Consider now an experiment run with a long mixing time during which the spins translationally diffuse from one domain or pore to the other. In the first encoding period, some spins may reside in B but diffuse during the mixing time and are in domain A with a longer T_2 relaxation time by the second interval. In the same manner, some spins may begin in A but move to B by the end of the experiment. This diffusion leads to off-diagonal peaks AB and BA in the contour map shown in Figure 2.12.

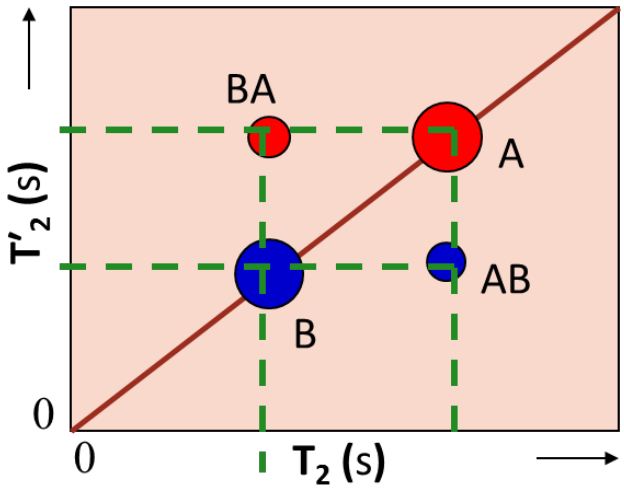

Figure 2.12: The theoretical result from a T_2-T_2 experiment during which molecules moved from one domain to the other during τ_m displays off-diagonal peaks [26].

These T_2-T_2 maps are incredibly useful because the intensities of the off-diagonal (mixing) peaks can be quantified and used to find a characteristic time scale for the sample. For a binary site model, the number of molecules starting in domain A but residing in domain B after τ_m is given by Equation 2.18 [33]

$$N_{AB}(t) = \frac{N_B \tau_{AB}}{\tau_{AB} + \tau_{BA}}(1 - \exp(-\lambda t)) \tag{2.18}$$

where τ_{AB} and τ_{BA} are the rates at which molecules migrate from site A to site B and vice versa, and $\lambda = \tau_{AB}^{-1} + \tau_{BA}^{-1}$. A similar expression can be written for $N_{BA}(t)$. A characteristic exchange time, τ_c, which describes the amount of time required for molecules to translationally diffuse from one domain to another can be calculated by taking the inverse of λ. In order to apply this quantitative analysis to real data, many T_2-T_2 contour maps are created with various mixing times, the intensities of the mixing peaks are found and normalized by total intensity, and those normalized intensities are plotted as a function of mixing time [33]. Equation 2.18 is fit to those

points, λ is determined from that fit, and τ_c is calculated from λ. Figure 2.13 illustrates the result of implementing these steps for domains called A, B, and C in an arbitrary sample; the points each correspond to a different contour map formed using a different mixing time, and the solid lines are the least squares fits of Equation 2.18 to the data.

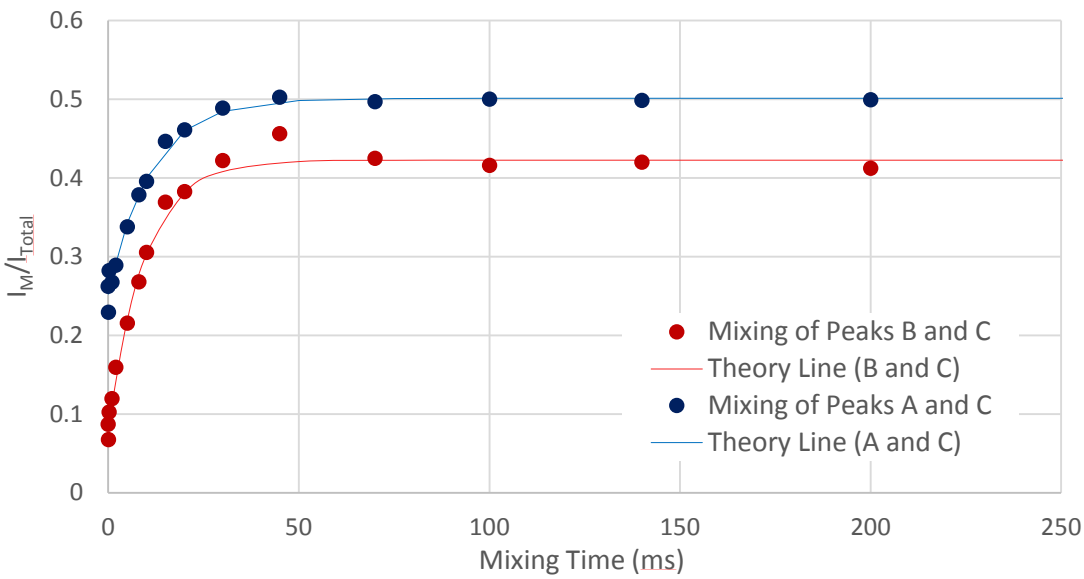

Figure 2.13. Quantitative analysis of T_2-T_2 correlation sequence data allows for determination of a characteristic time scale.

Once this analysis has been completed and τ_c obtained, one more piece of information can be used to determine a characteristic length scale, l_c, which describes an average distance between the domains in question. Because of the Einstein relation in three dimensions, $\langle Z^2 \rangle = 6Dt$, mean squared displacement is easily found once a time scale and a diffusion coefficient are known. τ_c serves as the time in this instance, and D can be found by doing an independent diffusion measurement on the sample. Therefore, in the case of T_2-T_2 exchange, it can be said that $l_c^2 = 6D\tau_c$ and the characteristic length scale can be calculated with little difficulty [33].

Knowledge of a quantitative, microscale length scale in a polymer compound is powerful information, and the T_2-T_2 correlation technique is frequently utilized in this thesis.

HPMCAS/ACETONE SYSTEMS

In order to form effective drugs using compounds of low solubility, a process called spray drying can be used. This process allows the insoluble drug to be evenly dispersed in a solid, amorphous polymer matrix which locks the active ingredient in a kinetically stable state and assists in its bioavailability. To create the spray-dried dispersion (SDD), a solution containing a polymer, solvent, and drug is sprayed through an atomizer in the presence of a hot, inert gas; most of the solvent evaporates off immediately, leaving a dry powder of polymer and drug "droplets." Care is taken to prevent phase separation or crystallization since either could impede the effectiveness or stability of the product [34, 35]. A commonly used polymer/solvent system for this process is hydroxypropylmethylcellulose acetate succinate (HPMCAS) and acetone. HPMCAS, a non-toxic polymer soluble in acetone, contains a cellulosic backbone with hydroxypropyl, methyl, acetate, and succinate functional groups randomly substituted and is frequently used as a drug excipient [34]. Its structure is displayed in Figure 3.1.

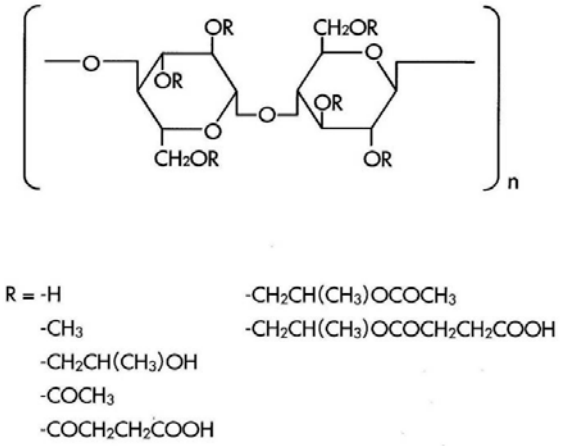

Figure 3.1. The structure of HPMCAS [36]

This thesis chapter describes data relating to this HPMCAS/acetone system with the goal of understanding its microstructure properties over various concentrations and temperatures.

Glass Transitions

One important parameter of the HPMCAS/acetone systems studied is their glass transition temperature T_g since the polymer mixture transitions to a glassy state during the spray-drying process. When the temperature of a polymer/solvent mixture is decreased through its T_g, it shifts from a liquid state to a "glassy" but amorphous solid state. A discontinuity in heat capacity accompanies this transition, but measurable quantities such as viscosity and diffusivity change smoothly over it. Thus, locating T_g for a substance can be quite difficult [37].

Glass transitions in polymer mixtures can be considered in terms of dynamic arrest. In both traffic and polymer systems, dynamics suddenly slow with increasing density as free volume becomes limited and cars or molecules cannot freely move around. Movement becomes slower until the system is locked into either a traffic jam or a glassy state [38]. This phenomenon is visualized for a polymer system in Figure 3.2; the black lines represent polymer chains, and the red dots symbolize solvent molecules. The polymer solution on the left is above its glass transition temperature and could be in a dilute or entangled regime. It exhibits some characteristic length scale l_c which defines an average free volume size and depends on parameters such as concentration and temperature [39]. When the solution's temperature is decreased through its T_g, dynamic arrest occurs and the system transitions to the glassy state shown on the right with a new characteristic length scale much smaller than that of the molten solution. The free volume size has decreased.

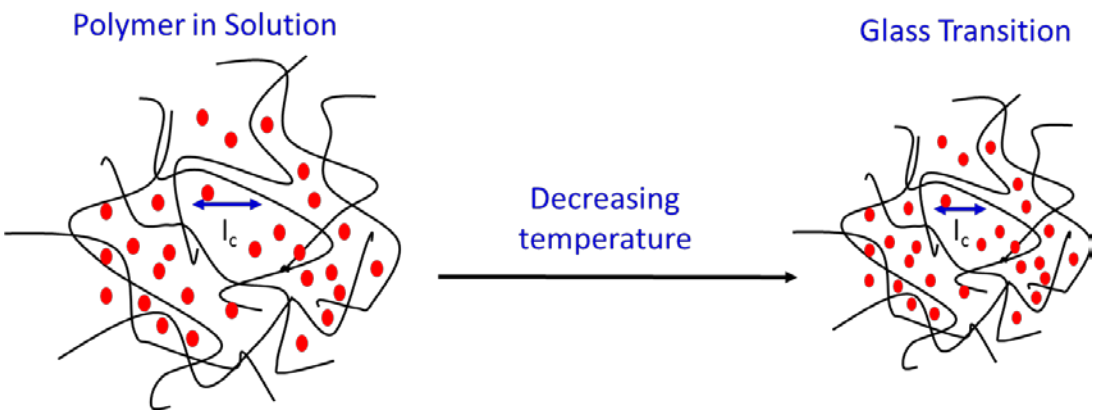

Figure 3.2. A polymer solution undergoes dynamic arrest as it is taken through its T_g [26].

For the solution on the right, the attractive potential energy between the polymer molecular units is much greater than the thermal energy ($\varepsilon \gg k_B T$) [40]. Dynamic arrest has occurred, and the solution exhibits sample-spanning networks and infinite cluster lifetimes – it is in a glassy state. Because SDDs are locked in a glassy state after the spray drying process, the following sections study dynamic arrest and glass transitions in HPMCAS/acetone systems. Two dimensional relaxometry and diffusometry data were utilized to understand the phenomena.

Methods

Sample Preparation

This chapter discusses two HPMCAS/acetone systems: a 7 wt% acetone sample made in-house and an SDD obtained from a manufacturer. To create the 7 wt% sample, HPMCAS polymer (Shin-Etsu Chemical Co.) was mixed with acetone to 85 wt% acetone and pipetted into an NMR tube. Five repetitions of evaporating acetone at ambient conditions and re-filling the NMR tube with HPMCAS/acetone solution were necessary to obtain a polymer-rich sample of sufficient volume to occupy the active region of the RF coil. Since acetone was the only volatile

component, the weight percent was determined gravimetrically. The 7 wt% sample on which the data in this section was acquired was capped at 11 wt% acetone and stored at ambient conditions for 270 days. During that time, the sample dried to 7 wt% acetone.

The wet SDD of HPMCAS and acetone was characterized by residual solvent analysis performed on the SDD batch using gas chromatography with a flame ionization detector. F rom this data, it was determined that the SDD contained 2.28 wt% acetone. During spray drying, the SDDs dried from a flowable liquid to a glassy state in seconds. The sample, stored at -20°C when not in the spectrometer, showed no measurable solvent loss.

2D Relaxometry and Diffusometry Measurements

Measurements were performed on a Bruker Avance III NMR spectrometer at a ^{1}H resonance frequency of 250.12 MHz. A Bruker high power probe and permanently attached 5 mm birdcage RF coil specially designed for 100 W maximal RF power was used, allowing for 90° and 180° pulse times as short as 3.5 µs and 7.0 µs respectively. The Diff30 gradient set was utilized, giving 17.82 T/m maximum gradient strength at 60 A in the z-direction.

Parameters of the T_1-T_2 correlation experiment and the T_2-T_2 exchange experiment were optimized for short T_2 relaxation times by minimizing the CPMG echo spacing. The signal acquisition dwell time was 0.4 µs. Depending on the duration times found for the 100 Watt 90° and 180° pulses, there were 22 or 23 dwells per τ (half the CPMG echo spacing), indicating a τ of 8.8 or 9.2 µs. The number of acquired echoes was 2000 if the echoes decayed to noise in this time, or 6000 if more were necessary to obtain full decay. At the start of the CPMG train, the receiver turned on. The receiver was gated between echoes such that acquired points had no magnitude, and it was ungated for one dwell on either side of the echo to allow for acquisition

of a single point per echo. For τ = 8.8 µs and 6000 echoes, the acquisition time was 2 x 8.8 µs x 6000 = 105.6 ms.

The T_1-T_2 correlation experiment encoded the signal with T_1 relaxation based on an inversion time t_1 before signal was acquired in the CPMG train during time t_2 (see Figure 2.6) [5, 24]. By looping through the experiment using variable inversion times, a two-dimensional data set was obtained with T_2 relaxation in the direct dimension and T_1 relaxation in the indirect dimension. The experiments performed for this study used 32 logarithmically spaced inversion times between 1 ms and 50 s. The repetition time (TR) was 25 s.

The T_2-T_2 exchange experiment encoded the signal for an amount of T_2 relaxation with a CPMG train during time t_1, stored the signal in the longitudinal axis during a mixing time τ_m, sent the signal through a second CPMG train, and acquired the signal during time t_2 (see Figure 2.9) [5, 32]. By looping through the experiment using variable numbers of echoes in the first CPMG train (t_1), a two-dimensional data set was obtained with T_2 relaxation during time t_2 in the direct dimension and T_2 relaxation during time t_1 in the indirect dimension. The first T_2 encoding period of the T_2-T_2 experiments in this study cycled the number of echoes through 64 logarithmically spaced whole numbers between 0 and 1000 if 2000 echoes were used in the second CPMG train, or between 0 and 4000 if 6000 echoes were used. The repetition time (TR) was 10 s.

The displacement observation time (Δ)-dependent pulsed gradient stimulated echo (PGSE) experiments were run for a range of observation times. Selection of parameters required a balance between the minimization of τ and the use of gradient durations (δ) long enough to obtain sufficient signal attenuation to measure diffusion. The signal acquisition dwell time was 1 µs, the number of acquired points was 2048, and the sweep width was 500 kHz. The

90° pulse times were 12.5 µs. The repetition time was 10 s. Experiments used sine shaped gradient pules with the gradient duration within the pulse program converted from the user-set effective gradient duration (δ) by TopSpin 3.2. The effective gradient duration (δ) was 0.6 ms at ambient conditions and 0.5 ms at 60° C. The gradient stabilization time, the delay after the gradient pulses, was 0.5 ms. The τ was 1.47 ms for experiments at ambient temperature and 1.3 ms for experiments at 60° C. The spoiler gradient duration was 2 ms. Experiments used 16 linearly spaced gradient steps. The observation time (Δ) was varied from 15 ms to 1 s while holding τ constant. The maximum gradient strength was 17.82 T/m if less than 30% signal attenuation (M/M_0=0.7) was obtained with this value, and was otherwise decreased with increasing Δ to keep signal attenuation near 30%.

Temperature Control

Temperature was controlled by the *BVT3000* Variable Temperature Unit using flowing nitrogen gas which was pre-chilled by the BCU II. The system was allowed to equilibrate for at least 30 minutes after a temperature change before tuning and matching, shimming, and determining the correct pulse power for the subsequent experiment.

Data Analysis

The two-dimensional experiments were processed using the 2D inverse Laplace transform (2D ILT) software discussed in the 2D Relaxometry section of Chapter 2 which revealed the rates of relaxation of the NMR signal as well as the weighting/magnitudes of these rates. By running the α-loop, a value of 10^9 for the smoothness parameter α was found to be correct for all experiments and was therefore implemented for all ILTs. The number of points in each direction of the ILT distribution was held constant at 32. Repetition over many samples

allowed for consistent features within the relaxation distributions to be identified. The characteristic mixing times, τ_c, were determined from T_2-T_2 maps using the method described in the 2D Relaxometry section.

The signal from the PGSE experiments were Fourier transformed in the resonance frequency domain, noise was baseline subtracted, and signal magnitude at each gradient value was found for the acetone signal (the only visible spectral peak). The acetone self-diffusion coefficient was then found by the Stejskal-Tanner method described in the Diffusometry section of Chapter 2 [14]. The gradient point range used in the analysis of each self-diffusion coefficient was adjusted for consistent signal attenuation among experiments.

Observing Glass Transitions with T_1-T_2 Maps

As established in the previous chapter, T_1-T_2 maps give a great deal of insight into the microstructure of samples. In this section, it will be seen how they can provide a simple method of determining a sample's glass transition temperature. Figure 3.3 shows a T_1-T_2 map of a 20 wt% acetone HPMCAS/acetone sample at 50°C.

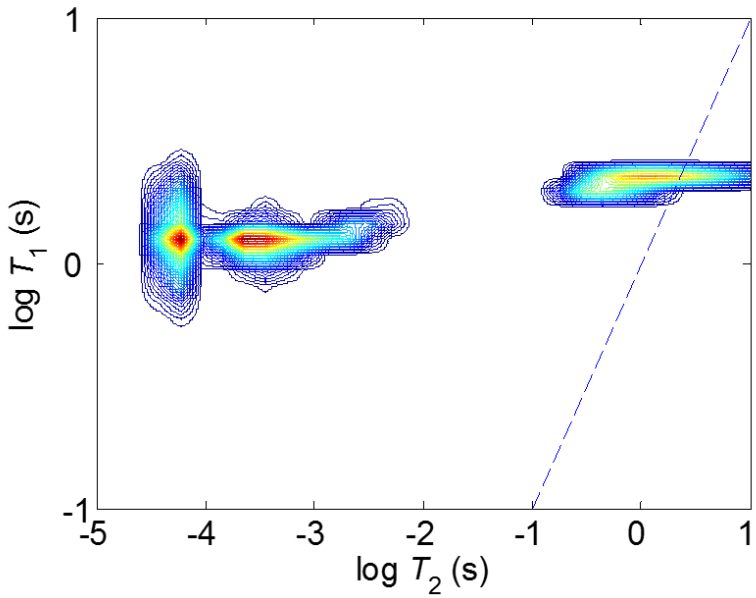

Figure 3.3. T_1-T_2 map of an HPMCAS/acetone system displaying domains of different mobility. The contour intensity (red highest) indicates the proportion of hydrogen spins in the sample with that magnetic relaxation behavior.

Three distinct populations are visible. The population on the parity line corresponds to the domain of highest mobility – the free acetone not feeling the effects of the polymer. The middle domain with a T_2 of approximately 1 ms relates to acetone that is close to the polymer backbone or its side chains and therefore has decreased mobility in comparison to free acetone molecules. The shortest T_2 population arises from the polymer itself and potentially acetone that is extremely associated with the polymer which have the least mobility of all the sample components.

An estimate of the glass transition temperature for a binary polymer/solvent system can be found using the phenomenological Fox equation shown in Equation 3.1 [41].

$$\frac{1}{T_g} = \frac{\omega_1}{T_{g1}} + \frac{\omega_2}{T_{g2}} \tag{3.1}$$

where ω_1 is the weight fraction of component 1, ω_2 is the weight fraction of component 2, and T_{g1} and T_{g2} represent the glass transition temperatures of the pure components. For the 20 wt% acetone sample shown in Figure 3.3, Equation 3.1 predicts that its glass transition temperature is -87°C using a value of 60 K (-213°C) for the T_g of acetone [42] and 393 K (120°C) for the T_g of HPMCAS [43]. At the map temperature of 50°C, the sample of Figure 3.3 is far above its glass transition temperature; note the population on the parity line which indicates a large amount of mobility and supports the idea that the sample was not locked into a state of glassiness.

Let us now examine polymer samples of different acetone contents over a range of temperatures. Figure 3.4 displays two samples, one concentrated at 7 wt% acetone and one more dilute at 45 wt% acetone, over three temperatures. In the first column, the more dilute sample is brought from 30°C to -18°C; its glass transition temperature is estimated by the Fox equation to be well below this range at -161°C. The domains of free acetone, highly associated acetone, and polymer are again seen in the maps, and they do not exhibit significant changes as the temperature is decreased. The dynamics remain similar and the free acetone population stays mobile even through a temperature difference as large as 50°C, indicating that the sample is far above its glass transition temperature.

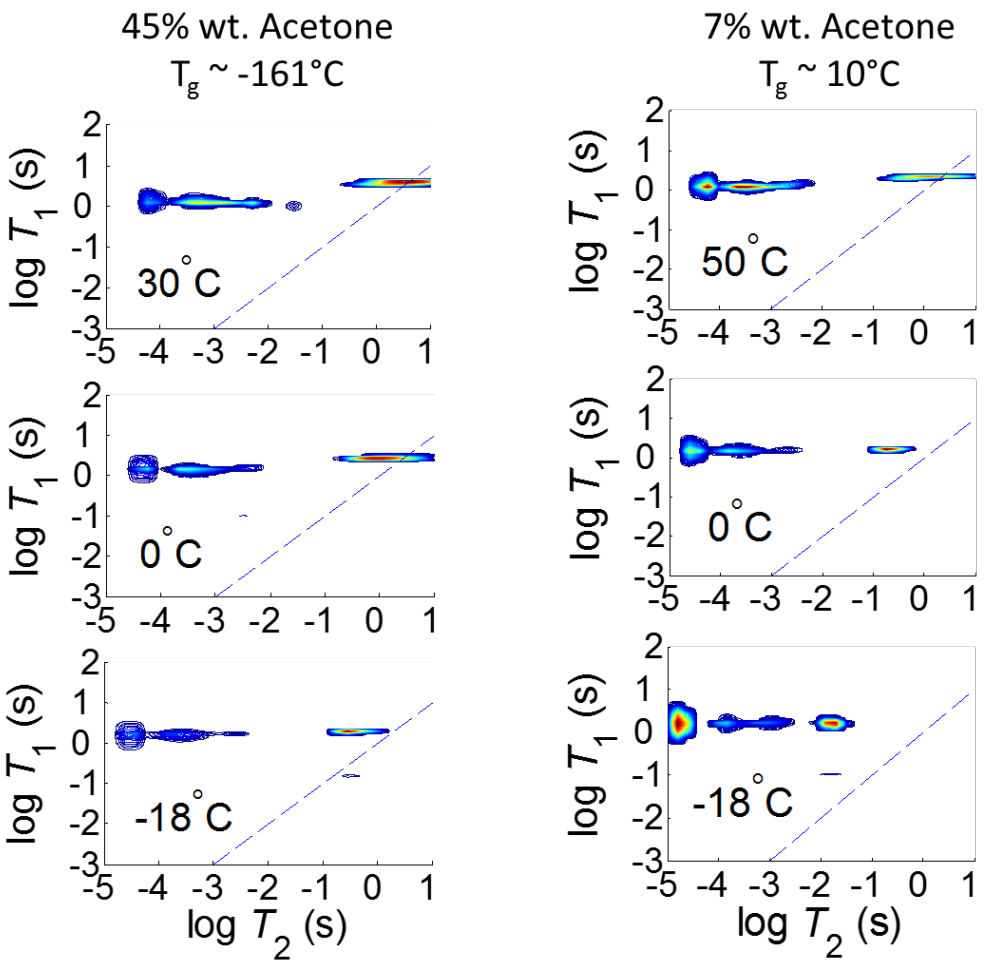

Figure 3.4. Samples of differing acetone contents over a range of high and low temperatures. The contour intensity (red highest) indicates the proportion of hydrogen spins in the sample with that magnetic relaxation behavior.

The NMR equipment is limited to temperatures down to -50°C well above the -161°C necessary for this sample's glass transition. In contrast, significant changes are seen in the 7 wt% acetone sample as the temperature is decreased to -18°C. This more concentrated polymer sample has a predicted T_g of 10°C, a temperature easily accessible with the equipment used. As the sample is taken from 50°C, a temperature above its T_g, to 0°C, a temperature slightly below its predicted T_g, notice that the free acetone population moves off the parity line to shorter T_2 values. This

change indicates that rotational mobility is decreasing and therefore dynamic arrest is occurring. At -18°C, the population has moved to a much shorter T_2 value and is far removed from the parity line. By this point, the sample is clearly locked in a glassy state with reduced mobility of the solvent acetone molecules.

Figure 3.5 shows temperature-varied T_1-T_2 maps of an SDD with 2.3 wt% acetone.

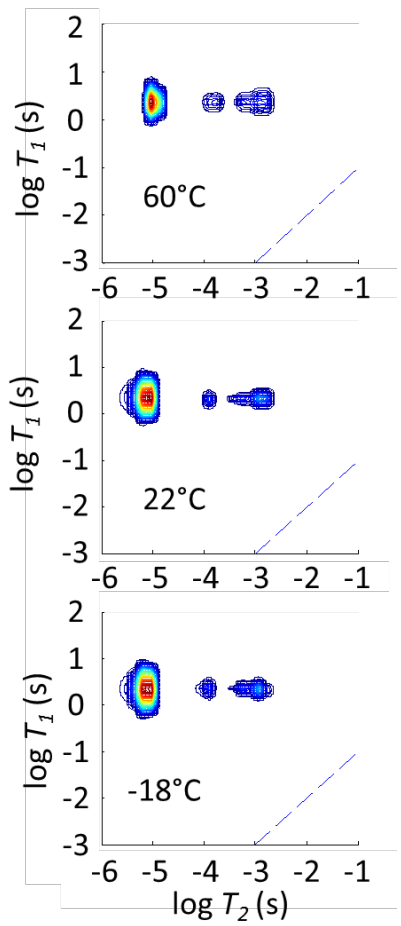

Figure 3.5. The microstructure of a glassy SDD does not change between 60°C to -18°C. The contour intensity (red highest) indicates the proportion of hydrogen spins in the sample with that magnetic relaxation behavior.

The T_g predicted by the Fox equation for this sample is 75°C, a temperature too high for the equipment to access. Notice that the T_1-T_2 maps show no changes as the sample is taken from 50°C down to -18°C. The longest T_2 population of free acetone is off the parity line for all temperatures and does not move. This demonstrates that the sample is indeed in a glassy state and confirms that dynamics do not change over a wide range of temperatures, a desirable quality in a pharmaceutical SDD.

Since determining a substance's glass transition temperature can be quite difficult, this T_1-T_2 method provides a necessary, potentially inexpensive benchtop method for determining T_g. It is non-invasive and relatively simple. One forms T_1-T_2 maps over a range of temperatures and watches the high mobility peak migrate off the parity line to regions of lesser mobility. The point at which the domain leaves the parity line indicates the onset of dynamic arrest, and the temperature at which the population ceases to move designates glassiness. This method can be applied to complex substances for which the Fox equation has more limited applicability. Furthermore, it can easily be determined if a compound remains in its glassy state over a range of temperatures by again watching the long T_2 peak and ensuring that it does not move, showing that dynamics are locked in.

Mesh Size Determination with T_2-T_2 Experiments

Figure 3.2 depicts how the characteristic length scale in a polymer sample changes through its glass transition temperature. It is helpful in understanding dynamics to quantify this length scale, but mesh sizes in polymer mixtures are too small to measure with most methods. NMR two-dimensional T_2 measurements and diffusometry, however, are capable of capturing dynamics on nanometer scales and were utilized to determine length scales as small as 200 nm

for the polymer samples studied. Figure 3.6 displays two T_2-T_2 maps for an HPMCAS/acetone sample with 7 wt% acetone at 22°C, a temperature slightly above its predicted T_g of 10°C.

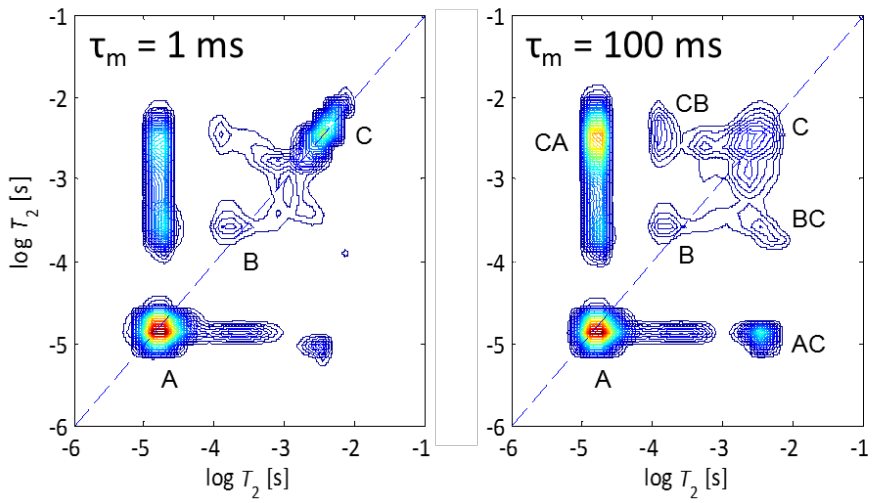

Figure 3.6. T_2-T_2 maps of a 7 wt% acetone polymer sample at 22°C with a predicted T_g of 10°C. The contour intensity (red highest) indicates the proportion of hydrogen spins in the sample with that magnetic relaxation behavior.

The left and right maps display short (1 ms) and long (100 ms) mixing times respectively. The three peaks on the diagonal represent three populations of different T_2 values. The domain with the shortest T_2 pertains to the polymer and acetone molecules highly associated with it, that with the longest T_2 symbolizes free acetone molecules, and the population in the middle shows acetone slightly associated with the polymer. At a mixing time of 1 ms, some spins are able to sample different domains and cause off-diagonal peaks to appear, and the peaks gain intensity as the mixing time increases. In the 100 ms mixing time map, the off-diagonal peaks representative of translational diffusion between populations B and C and A and C (CB, BC, AC, CA) are noticeably more intense. Note exchange between populations A and B has almost

completely saturated by 1 ms as indicated by a lack of change in intensity with τ_m. Upon applying the analysis described in the "2D Relaxometry" section of Chapter 2 to data for varying mixing times, the plot in Figure 3.7 was generated.

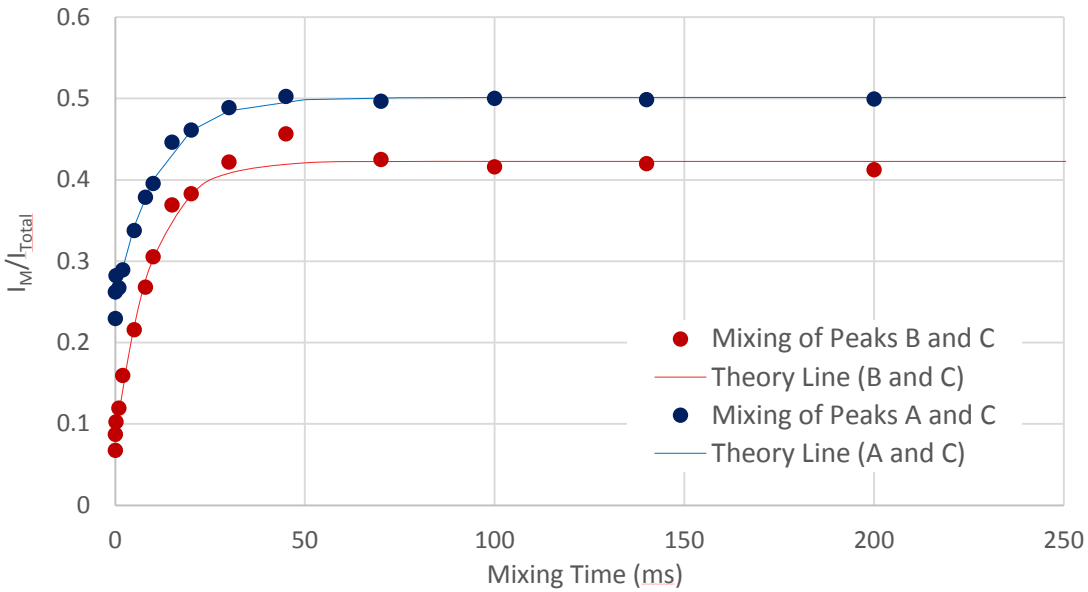

Figure 3.7. 7 wt% polymer sample mixing peak intensities at 22°C as a function of mixing time along with theory line fits

The data points all pertain to different τ_m data sets, and the lines were derived from fits of Equation 2.18 to the points with $I_M = N_{AB}(t) + N_{BA}(t)$. From the fits, a characteristic time scale (τ_c) was calculated for spin diffusion between peaks B and C and between domains A and C [5, 33]. The τ_c value for mixing between peaks B and C pertains to the average time required for a molecule to translationally diffuse from a domain where acetone is feeling the effects of the polymer to a domain where acetone is more free or vice versa. The calculated τ_c for peaks A and C represents an average time for an acetone molecule to move between a domain of high mobility and a domain of low mobility highly associated with the polymer. The quantitative

values found are shown in Table 3.1. As is physically reasonable, the average time required to diffuse between domains A and C is slightly longer than that needed to move between populations B to C. Using independent PGSE acetone diffusion coefficient measurements on the samples and the determined characteristic time scales, characteristic length scales (l_c's) were calculated using the Einstein equation [23], $\langle {l_c}^2 \rangle = 6D\tau_c$, and are displayed in Table 3.1. The approximate length between the domains of free acetone and those of acetone highly associated with the polymer was found to be 270 nm, and that between domains of free acetone and acetone molecules less associated with the polymer was determined to be 250 nm. It is, of course, logical that the length scale between A and C is slightly longer than l_c between B and C.

Acetone Content	**T_g Predicted by Fox Equation**	**Experimental Temperature**	**Characteristic Time Scale, B and C**	**Characteristic Time Scale, A and C**	**Characteristic Length Scale, B and C**	**Characteristic Length Scale, A and C**
7 wt%	10°C	22°C	9.5 ms	11 ms	250 nm	270 nm
7 wt%	10°C	60°C	46 ms	75 ms	2000 nm	2500 nm
7 wt%	10°C	0°C	Inaccessibly Short	Inaccessibly Short	--------	--------
2.3 wt% (SDD)	75°C	22°C	Inaccessibly Short	Inaccessibly Short	--------	--------

Table 3.1. Characteristic time and length scales for HPMCAS/acetone systems of different concentrations at different temperatures

Next, the same 7 wt% acetone sample was examined at a temperature much higher than its T_g. T_2-T_2 maps of the mixture at 60°C can be seen in Figure 3.8.

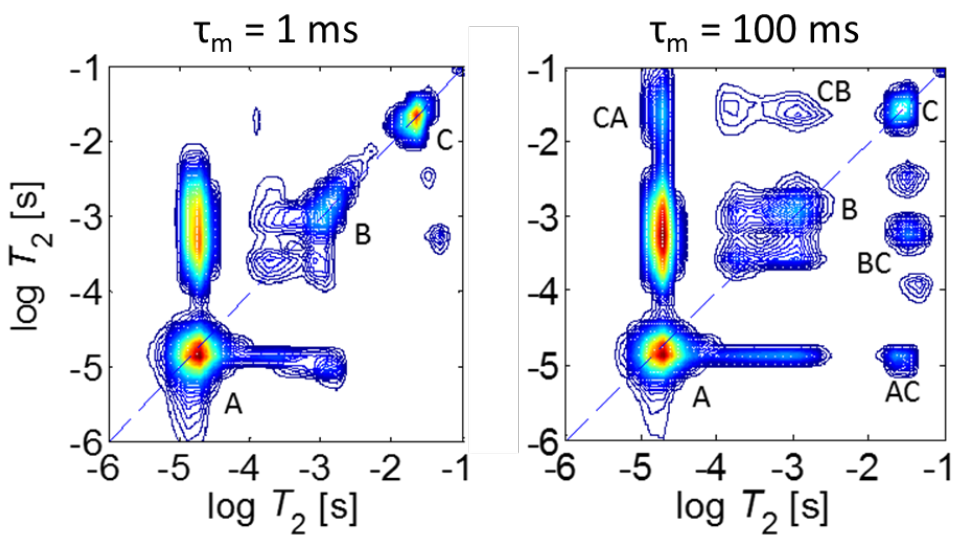

Figure 3.8. T_2-T_2 maps of a 7 wt% acetone polymer sample at 60°C, a temperature far above its T_g. The contour intensity (red highest) indicates the proportion of hydrogen spins in the sample with that magnetic relaxation behavior.

All of the populations have moved up in T_2 in comparison to those in Figure 3.6 due to the increased mobility that arises from being much more liquid-like than in a glassy state. Populations A, B, and C are still present and correspond to the same domains, and the same increased mixing peak intensity can be noticed in the longer mixing time map on the right when compared to the shorter mixing time map on the left. The diffusion between domains B and C and between A and C was again studied and the T_2-T_2 exchange analysis implemented in the same way to produce Figure 3.9.

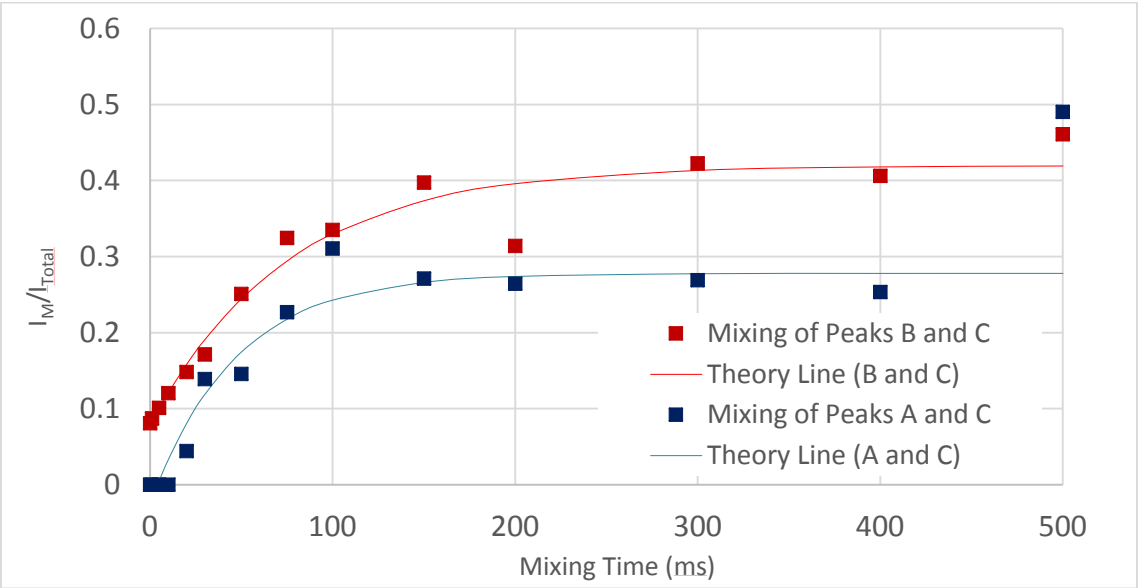

Figure 3.9. 7 wt% polymer sample mixing peak intensities at 60°C as a function of mixing time along with theory line fits

The results of the theory line fits are shown in Table 3.1. As before, an acetone diffusion coefficient was independently measured for the sample at 60°C and used to find l_c values. The time scales and length scales are greatly increased, reflecting the larger free volume caused by the sample being at a temperature much greater than its T_g.

Finally, this same 7 wt% acetone sample was analyzed at 0°C, a temperature below its T_g. At 0°C, it was expected that the sample would be in a glassier state and exhibit decreased free volume. This was seen in the T_1-T_2 map of the same sample in Figure 3.4 as the free acetone peak exhibited decreased mobility. Figure 3.10 displays two contour maps, one taken at a short mixing time and one at a longer τ_m.

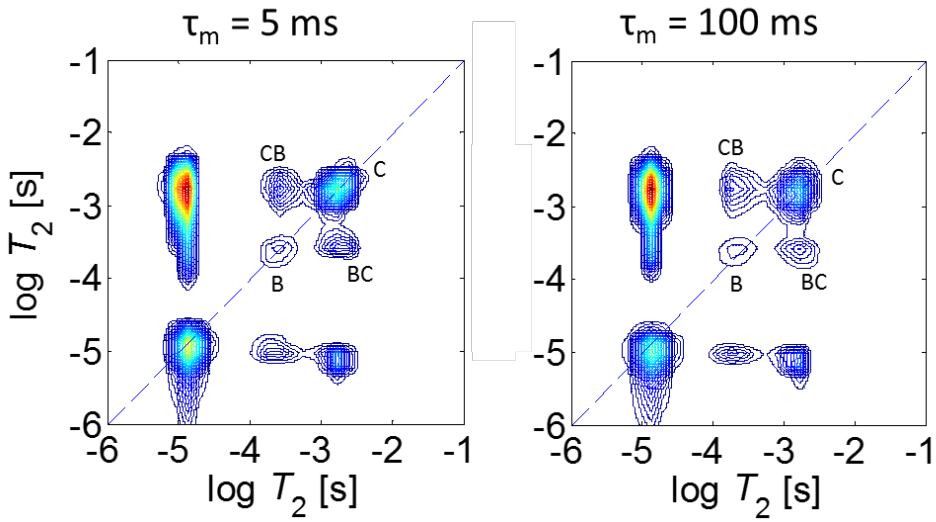

Figure 3.10. T_2-T_2 maps of the 7 wt% acetone sample at 0°C, a temperature below its T_g. The contour intensity (red highest) indicates the proportion of hydrogen spins in the sample with that magnetic relaxation behavior.

In contrast to previous examples, the maps appear quite similar; an increase in the intensity of the off-diagonal populations is not apparent. Analysis of the cross peak intensity as a function of τ_m revealed that translational diffusion exchange occurred on time scales too short to capture. The molecules in this glassy state sampled their small domains quickly and saturated the mixing peaks almost immediately. Even with mixing times as short as 0 ms, inherent delays in the electronics prevented the initial exponential increase in signal from being captured. Figure 3.11 shows this "levelling out" of the mixing peak intensity at short mixing times as well as points from the sample at 22°C for reference.

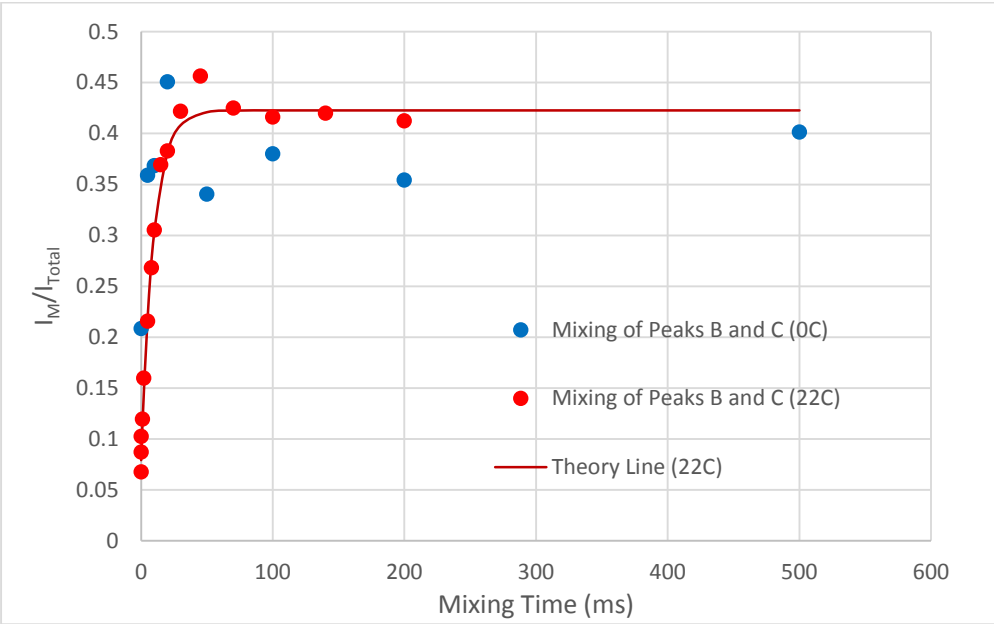

Figure 3.11. Mixing occurred on an inaccessibly short time scale in the glassy 7 wt% acetone sample.

Although quantitative time and length scales could not be extracted from this sample at 0°C, the analysis is still quite interesting and provides useful information. Time and length scales were found for the sample near and above its T_g, and it is evident that the sample below its T_g has a much decreased mesh size. This inference is consistent with the expectation that the glassier sample would contain less free volume than the liquid-like sample due to it being in a state of dynamic arrest [37, 44]. The T_2-T_2 exchange method could be used to determine if a compound at a certain temperature is glassy, and it could potentially be helpful in monitoring stability over various temperatures, times, and relative humidities.

Let us now study a glassy SDD at a temperature far below its glass transition temperature. T_2-T_2 experiments were run on a 2.3 wt% SDD at 22°C (predicted T_g = 75°C) to produce the data displayed in Figure 3.12.

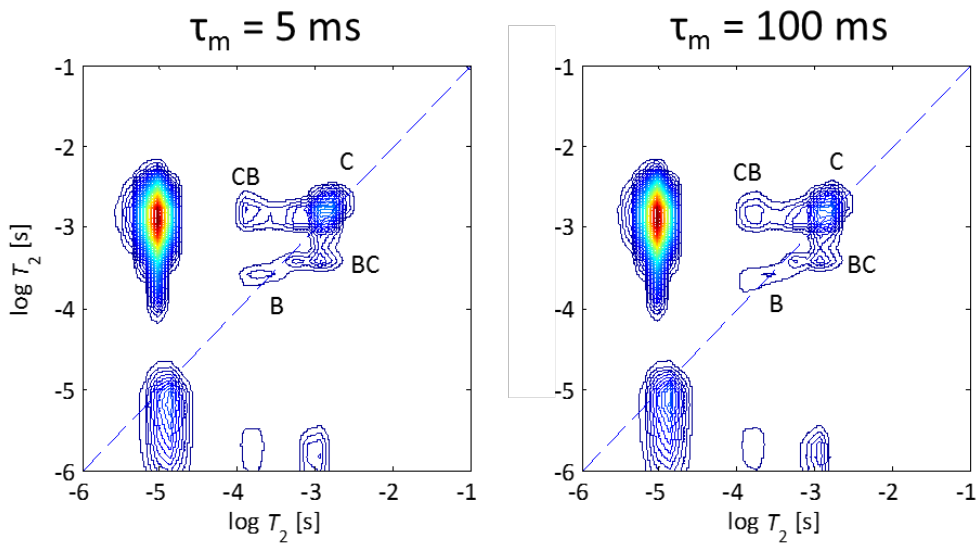

Figure 3.12. T_2-T_2 maps of a 2.3 wt% acetone SDD at 22°C with a predicted T_g of 75°C. The contour intensity (red highest) indicates the proportion of hydrogen spins in the sample with that magnetic relaxation behavior.

Note that the short and long mixing time maps are virtually indistinguishable similarly to those seen in Figure 3.10. Indeed, upon attempted analysis of the experiments, it was found that the mixing peak intensities again appeared levelled out even after the shortest possible mixing times. Figure 3.13 exhibits the points plotted from the SDD maps as well as the B and C analysis from the 7 wt% acetone sample for reference. Just as in the 7 wt% glassy sample, exchange occurred on an inaccessibly short time scale and no initial increase in mixing peak intensity could be captured. This supports the idea that T_2-T_2 maps are a useful method for determining glassiness.

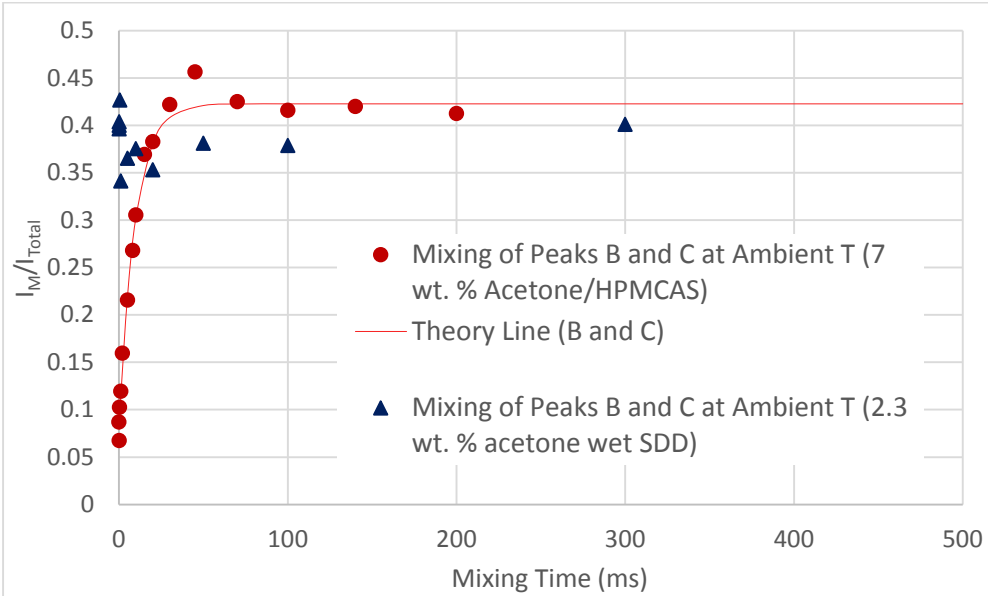

Figure 3.13. Analysis of the SDD at 22°C was not possible because the spins sampled the entire domain even after the shortest mixing times.

The method of determining time and length scales via T_2-T_2 exchange has been applied to porous materials such as rocks and cement [33, 45], but application to polymer systems is limited [46]. The data here displays a novel method for exploring polymer systems' dynamics above, near and below their T_g. Characteristic length scales were quantified and decreased as the samples underwent dynamic arrest. Although mesh sizes could not be acquired for samples in their glassy state due to exchange occurring on inaccessibly short time scales, a distinctive levelling out of mixing peak intensity was observed at short mixing times for glassy samples. This feature of a glass could be utilized in conjunction with T_1-T_2 maps for determination of T_g and testing of stability over a range of parameters including concentration, relative humidity, time, and temperature.

Mesh Size Determination with Time-Dependent Diffusion

As in porous media where fluid is contained within the pores of a solid matrix, polymer systems in a gel state contain connected domains of high solvent content and mobility within domains of higher polymer density and significantly lower mobility [47]. In this section, concepts from NMR analysis for determining pore sizes and length scales in porous media will be applied to HPMCAS/acetone systems and used to confirm length scales determined by means of T_2-T_2 exchange experiments.

Figure 3.14 presents a figure from a study of xenon gas diffusion NMR in random packs of mono-sized glass beads [48]. To generate the data in the figure, PGSE diffusion experiments with different observation times were run on xenon gas at ~6 bar pressure in bead packs of varied bead diameters [48]. The diffusion coefficient normalized by a free xenon diffusion coefficient was plotted as a function of normalized diffusion length, $b^{-1}\sqrt{D_0 t}$, where b is the bead diameter, D_0 is the free gas diffusion coefficient, and t is the observation time [48]. Mitra, Sen, and co-workers have calculated that $\frac{D(t)}{D_0}$ scales linearly with $\sqrt{D_0 t}$ by $\frac{s}{V_p}$, the pore surface area to volume ratio, in the short time limit (overlaid with a blue line) [49, 50]. This is described by Equation 3.2 [49].

$$\frac{D(t)}{D_0} = 1 - \frac{4}{9\sqrt{\pi}}\frac{S}{V_p}\sqrt{D_0 t} \tag{3.2}$$

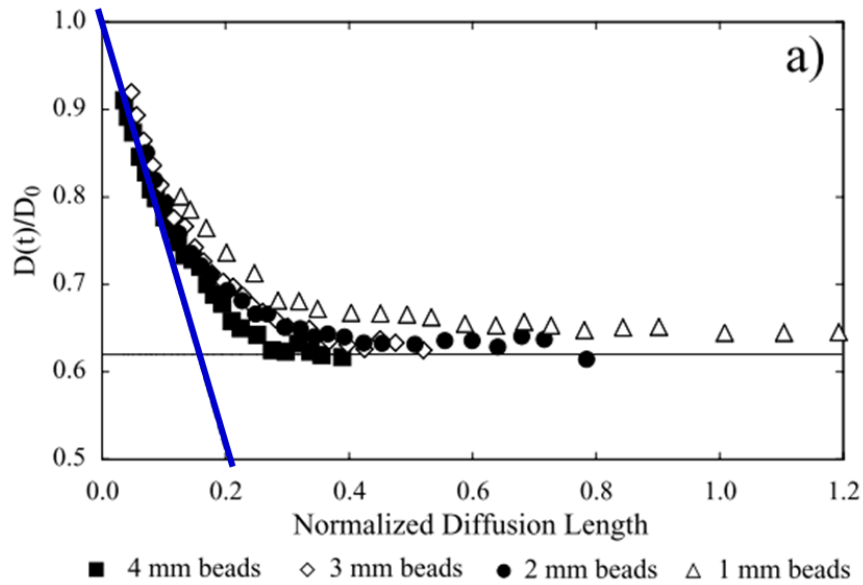

Figure 3.14. Time-dependent diffusion measurements of xenon gas in bead packs of varied bead diameter. The blue line indicates the short time limit [48]. Used with permission from Elsevier.

For spheres, $\frac{s}{V_p}$ scales as the inverse characteristic length scale of the system, $\frac{3}{2b}$. Thus, when $\frac{D(t)}{D_0}$ is plotted against the diffusion length scale normalized by the bead diameter $b^{-1}\sqrt{D_0 t}$, the data for spheres of all diameters collapse onto the same trend as seen in Figure 3.14.

The concepts from this approach for characterizing porous media are borrowed and applied to the HPMCAS/acetone system to produce Figure 3.15. The diffusion of the acetone molecules is determined using spectral resolution of the acetone peak, and the solvent acetone molecules probe the polymer molecule mesh structure just as the fluid filling the pores of a solid porous media sample the pore space structure.

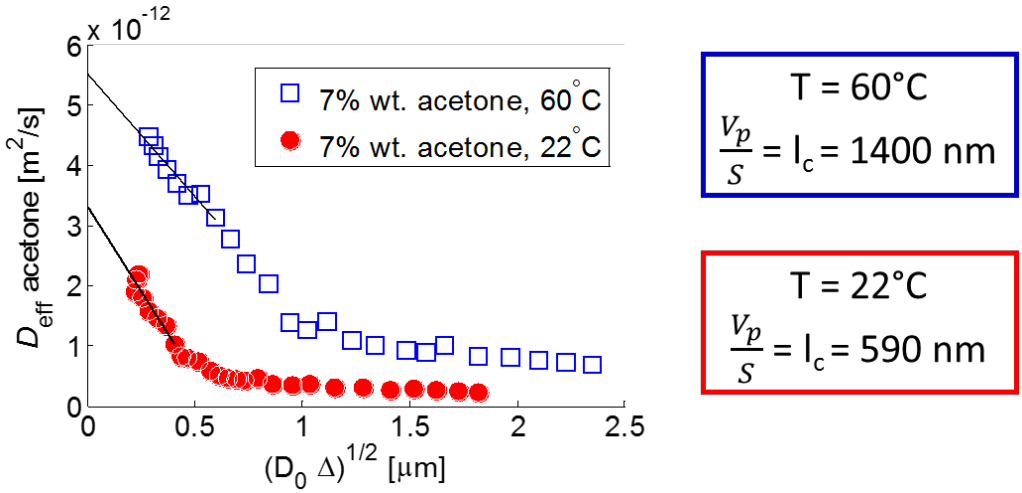

Figure 3.15. Displacement time-dependent diffusion measurements of the acetone molecules are used to determine l_c's of the 7 wt% acetone sample at 22°C and 60°C [51].

This figure displays data obtained on the 7 wt% acetone sample using the PGSE pulse sequence shown in Figure 1.8 with a varied displacement observation time Δ. As in Figure 3.14, the diffusion coefficient is plotted as a function of $\sqrt{D_0\Delta}$ and the short time limit studied. The slope of this short time limit correlates to $\frac{S}{V_p}$ of the "pores" or domains of high mobility in the system which provides an estimate of the characteristic length scale. Data was acquired at both 22°C and 60°C and the slope of the short time data calculated. The resulting l_c agrees reasonably well with the length scales determined through T_2-T_2 exchange studies of the same sample at the same temperatures. A summary of the results can be found in Table 3.2. By using approaches applied to characterize porous media, length scales were obtained which confirmed the mesh sizes determined using T_2-T_2 experiments. This agreement both supports the usefulness of the T_2-T_2 data and the idea that polymer gel and glass system structure can be characterized by NMR methods developed to describe the structure of porous media.

The data in Figure 3.15 can be displayed in another useful way. Consider Einstein's equation in one dimension, $\langle Z^2 \rangle = 2Dt$, which says that mean squared displacement (MSD) scales linearly with time for Brownian motion [23]. In the PGSE experiment, MSD is determined over a displacement observation time Δ so a log-log plot of the time-dependent diffusion measurements for unrestricted Brownian motion will exhibit a straight line with a slope of 1 when log(MSD) is plotted vs log(Δ). When the MSD data from the HPMCAS/acetone system is plotted this way (Figure 3.16), plateaus are clearly visible rather than a straight line through all observation times. In addition, the slopes of the lines before and after the plateaus are less than 1, indicating subdiffusion [52, 53].

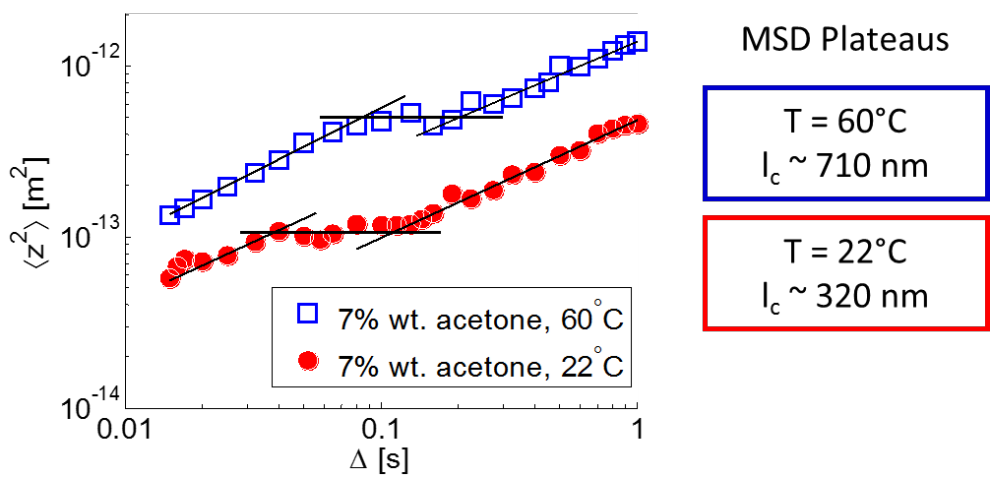

Figure 3.16. Displacement time-dependent diffusion measurements of acetone molecules in the 7 wt% acetone sample at 60°C and 22°C plotted as log(MSD) vs log(Δ) [51].

These plateaus in MSD are well known for glass phase systems [54] and have been predicted for polymer gel systems [40, 55]. Consider the diagram of a blue acetone molecule in a "cage" of green polymer molecules shown in Figure 3.17.

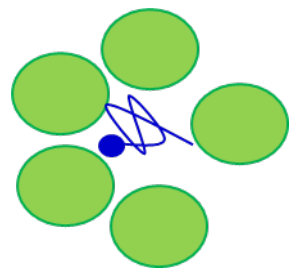

Figure 3.17. The blue acetone molecule diffuses until it feels the restriction of the green polymer molecules around it [26].

During short times, the molecule diffuses in a domain of larger free volume and likely higher solvent concentration. This regime pertains to the initial linear region in Figure 3.16. Given enough time to move a distance that allows sampling of the cage composed of the polymer molecule physical crosslinks, the acetone molecule starts to feel the polymer molecules surrounding it and its displacement is inhibited by the cage of polymer. The MSD levels off with time and the plateau is formed [40, 55]. Finally, after some time of being caged in, the molecule has time to break out of the cage and begin diffusing more freely in a domain of larger free volume, giving the second linear region of the plot. In view of this explanation, the location of the plateau corresponds to an average domain size of higher free volume of the sample [39, 47]. The length scales $l_c \sim \langle Z^2 \rangle^{\frac{1}{2}}$ for the two temperatures agree fairly well with both the l_c's determined in Figure 3.15 and those found with T_2-T_2 experiments. All of the length scale data is displayed in Table 3.2. This agreement confirms the validity of both of the prior analyses and provides a third means of mesh size determination.

Method	l_c at 22°C	l_c at 60°C
T_2-T_2 Exchange	250 nm	2000 nm
Diffusion (Porous Media Concepts)	590 nm	1400 nm
Diffusion (MSD vs Δ)	320 nm	710 nm

Table 3.2. Length scale determination via different methods of the 7 wt% acetone sample

Conclusions

In an effort to more fully understand and characterize the gelation that occurs during the drying process, the commonly used polymer HPMCAS in a solvent of acetone was studied. Focus was placed on the system's glass and gel transition dynamics since drying transitions a liquid polymer solution to a gel or a glassy, amorphous solid. T_1-T_2 correlation and T_2-T_2 exchange data were acquired along with time-dependent diffusion data for samples of varied acetone concentrations at different temperatures. T_1-T_2 data provide a simple, effective method for determination of glass transition temperature. The movement to shorter T_2's of a mobile domain on the parity line indicated the onset of dynamic arrest, and its lack of movement once it had settled off the parity line signified glassiness. Because T_g can be quite difficult to quantify with other methods, this NMR technique could provide an inexpensive, non-invasive method for acquiring T_g. T_2-T_2 and diffusometry experiments provided further insight into glass transitions through determination of characteristic length scales. The data also indicate that systems which are above their T_g but have gelled due to decreased solvent concentration exhibit similar relaxation behavior. By analyzing T_2-T_2 exchange over different mixing times, quantitative characteristic time and length scales were found for a sample in a gel

state above its T_g. Exchange occurred on inaccessibly short time scales for glassy samples, but it was established that mesh size [47] or liquid-like free volume domain size [39] decreased as the sample was brought closer to its glass transition. A characteristic levelling out of mixing peak intensity for short mixing times provided a signature of a glassy sample which could prove useful for stability testing. Finally, diffusometry confirmed the length scales found with T_2-T_2 exchange. Approaches from porous media were applied [5, 48, 49] when plotting time-dependent diffusion data to find $\frac{V_p}{S}$, a characteristic mesh size, and MSD vs Δ plots revealed plateaus occurring at length scales which agreed with the other two methods. The study in this section provides the first use of T_2-T_2 exchange to quantify characteristic length scales of polymer gel systems and directly measures the glass-like plateau in the MSD in a gel. This study lays the foundation for further work using two-dimensional relaxometry in the study of polymer mixtures and their glass and gel transitions.

PSEUDOLATEX

In this section, the thermal gelation of polymer colloidal dispersions is studied. Colloidal aqueous polymer dispersions can be prepared in two ways. Either emulsion polymerization is performed on monomers such that polymerization takes place in the particles that form during the first moments of the emulsion process, or a pre-formed, water-insoluble polymer is emulsified [56]. The former process produces a latex, and the latter yields a pseudolatex. For pharmaceutical applications such as enteric coatings [57], pseudolatexes are generally preferred due to the potentially toxic monomers or oligomers that remain in solution after the formation of a latex [56]. This thesis investigates two types of cellulose-based pseudolatex. The first, pseudolatex 1, is formed with a cellulose ester termed polymer 1, and the second, pseudolatex 2, is made using a different ester called polymer 2.

Thermal Gelation

The psedolatexes studied in this thesis gel upon heating. The precise mechanism for pseudolatex thermal gelation is unknown, but an overview of three unique mechanisms for the thermal gelation of polymers will be offered here in order to increase understanding of the phenomenon.

McAllister et al. presented a study on the reversible thermal gelation of methylcellulose [58] in which they determined that their results could not be explained solely using the commonly assumed idea that polymer solutions separate into two isotropic phases upon heating. Their methylcellulose solutions developed fibrillar aggregates at elevated temperatures, indicating that the solutions phase separate into an isotropic phase and a

nematic phase during gelation [58]. Kinetic limitations to the development of the nematic phase following heating lead to the formation of micron-sized fibrils which consist of collapsed polymer chains assembled axially. The exact fibril structure is unknown, but they give the gel a degree of nematic ordering. Thus, the authors postulated that a nematic order parameter which describes the coexistence of an isotropic and a nematic phase is necessary to define the solution behavior.

Star polymers and block copolymer micelles also undergo reversible thermal gelation, and the mechanisms involved were studied by Kapnistos et al. [59]. The authors theorized that concentrated solutions of these materials may display unexpected behaviors with changing temperature because of their unique polymeric and colloidal characteristics, and they successfully demonstrated a reversible gelation transition using different experimental techniques. The polymer solutions were suspended in good solvents, and it was found that the solvent quality increased with temperature [59]. Stronger arm interpenetration was observed with heating although core distance was insensitive to temperature variations. The study suggested the following mechanism for the reversible thermal gelation of these materials: because the solvent quality increases with temperature, the spheres swell with heat. Their arms overlap to accommodate themselves in the same volume but are hindered by excluded volume repulsions, and the system forms “trapped” spheres in equilibrium with “free” spheres [59]. A macroscopic, ordered solid is formed.

Sarkar studied yet another thermal gelation process in a paper that postulates the cause of methyl and hydroxypropyl methylcellulose reversible gelation [60]. When solutions of the polymers are heated, molecules lose their water of hydration and viscosity decreases. At a certain point of dehydration, a polymer-polymer association occurs and forms a sample-

spanning structure. Accompanied by this occurrence is a sharp rise in relative viscosity and a macroscopically solid gel formation [60]. Thus, gelation is primarily due to the hydrophobic interactions between molecules with methoxyl substitution. The author studied gelation of these polymers as a function of molecular weight, degree of substitution, and type of additive using various experimental techniques to characterize the phenomenon of thermal gelation to a great extent [60].

In contrast to the previous three examples, polymer 1 and polymer 2 pseudolatexes gel irreversibly. Storage modulus, loss modulus, and viscosity experience a sharp increase around 50°C for the polymer 2 formulation as shown in Figure 4.1 when the gel structure forms.

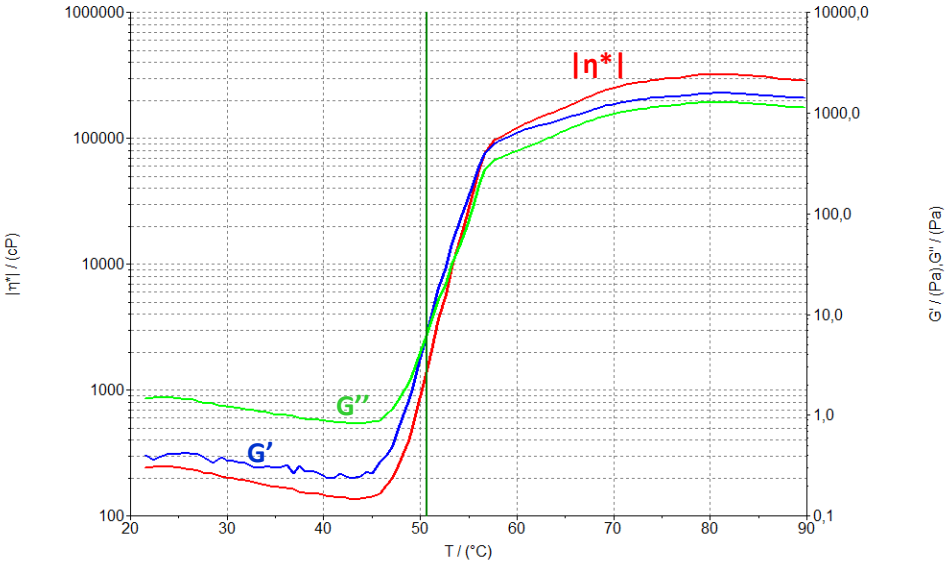

Figure 4.1. Shear modulus, loss modulus, and viscosity sharply increase as the polymer 2 pseudolatex thermally gels [61].

Polymer 1 pseudolatex gels around a slightly lower temperature of 45°C. The solutions expel water as they are heated and effectively increase the particle volume fraction in the gel. Free water can be seen sitting on top of the samples post-gelation. It is important to note that the polymer 2 samples were placed such that the active region of the RF coil was far below the free water during all NMR experiments so only signal from the gel was collected, but the polymer 1 gels pulled away from the sides of the test tube (see Figure 4.4) such that signal from their expelled water was collected along with signal from the gel. Figure 4.2 depicts a polymer 2 sample before and after gelation with the location of the RF coil active region denoted.

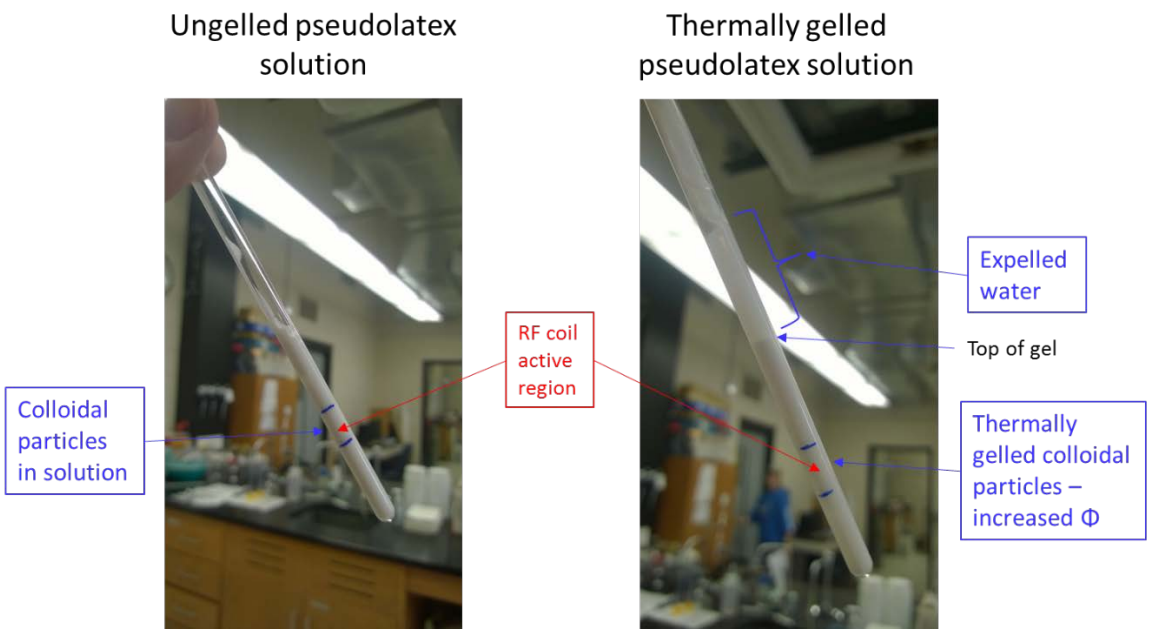

Figure 4.2. A pseudolatex 2 sample expels water as it gels, increasing colloidal particle volume fraction in the gel. The RF coil active region is marked in blue.

The following sections characterize polymer 1 and polymer 2 pseudolatex gelation as a function of solution aging and plasticizer content using NMR methods and postulate a mechanism for the irreversible thermal gelation of these polymeric colloidal dispersions.

Aging Mechanisms

Pseudolatex colloidal dispersions are prone to stability problems as they age. They become progressively more viscous over time due to coagulation of the colloidal particles. This phenomenon can be traced back to ester hydrolysis [62]. When the dispersions are first made, particles are stabilized with surfactant and the polymer core is shielded from water. Over time, the polymer becomes exposed to water as it diffuses into the particles and hydrolysis of ester bonds occurs [62]. Once those bonds have been cleaved, free acid is released into the solution and effectively lowers the pH. Particles in colloidal dispersions have surface charges which prevent them from interacting, but in the presence of electrolytes, those surface charges are diminished from contact with ions of opposite charges. This change leads to colloid destabilization and coagulation of the particles [63]. Therefore, once ester hydrolysis produces sufficient ionic strength, the pseudolatex solutions become more viscous as particles aggregate together [62].

Although polymer 1 and polymer 2 pseudolatexes both experience a loss of stability over time for the reasons described above, polymer 2 does so less quickly. Its large substituent group provides steric hindrance of the hydrolysis reaction and causes the rate of free acid production to decrease [62]. Thus polymer 2 pseudolatex exhibits better stability properties than dispersions made with polymer 1.

Methods

Sample Preparation

All of the pseudolatex samples were manufactured and shipped to the MSU lab for NMR experiments. All of the samples were loaded into 5 mm tubes with a vacuum method; an amount of pseudolatex appropriate for the filling of a test tube was drawn from its original container into a length of tubing with a vacuum, then the dispersion was removed from the tubing and deposited into the glass test tube using air pressure. In this way, the viscous samples were neatly and homogeneously placed into the bottoms of their test tubes.

2D Relaxometry and Diffusometry Measurements

All experiments shown in the polymer 1 Pseudolatex section were run on a Bruker Avance III NMR spectrometer with a ^{1}H resonance frequency of 250.12 MHz. A high power probe base made by Bruker was utilized along with its attached 5 mm birdcage RF coil and the Diff30 gradient set, a set capable of gradient strengths up to 17.82 T/m.

For T_1-T_2 measurements of the polymer 1 pseudolatex, focus was placed on the liquid-like molecular populations which occur near the parity line on a T_1-T_2 distribution by using a tau value of 276 µs. This tau value filtered out all populations with T_2's less than 276 µs and made the inverse Laplace transform procedure more regular. In order to obtain 23 dwells per tau, the dwell time was set as 12 µs, and 6,000 echoes allowed the signal to decay into noise. With these values, the acquisition time was 3.3 s. T_2-T_2 measurements were performed with the same tau, dwell time, and number of echoes. For the first T_2 encoding period, the number of echoes was cycled through a list of 64 logarithmically spaced numbers between 0 and 2000.

Shorter T_2 populations were captured in the T_1-T_2 maps for the polymer 2 pseudolatex by implementing a tau time of 9.6 µs. With this value, the domains arising from polymer signal were resolved. A dwell time of 0.4 µs allowed for 23 dwells per tau, and 10,000 echoes were required in order for the noise to be reached. These same parameters were utilized in the polymer 2 pseudolatex T_2-T_2 maps along with a list of 64 logarithmically spaced echo numbers between 0 and 1000.

PGSE diffusion experiments on both pseudolatex formulations were run with a gradient duration (δ) of 1 ms and an observation time (Δ) of 50 ms unless D(Δ) was being studied. The number of points acquired was 4096, the 90° pulse times were approximately 4 µs, and trapezoidal gradient pulses were used. The tau time was minimized at 2.12 ms, and experiments implemented 16 linearly-spaced gradient steps. The experiments were optimized to study diffusion of water rather than polymer by going out to a gradient value of about 0.5 T/m; this number decreased a small amount as temperature increased with the goal of keeping signal attenuation around 30%. For water peak diffusion measurements as a function of observation time, Δ was varied between 15 ms and 500 ms, and the gradient values used were set to obtain a signal attenuation of about 30%. All other parameters remained as stated previously.

Temperature Control

Temperature was controlled for all experiments using a *BVT3000* Variable Temperature Unit temperature control unit which used flowing nitrogen gas that was pre-chilled by the BCU II. Upon temperature changes, samples were given a minimum of 30 minutes to equilibrate before any set-up procedures were run.

Data Analysis

Raw T_1-T_2 and T_2-T_2 multi-exponential data was inverted to reveal microstructure populations using the 2D inverse Laplace transform (2D ILT) software discussed in the 2D Relaxometry section of Chapter 2. The α-loop function in the ILT interface was utilized to determine optimal α values for the scans; a smoothing parameter of 10^7 was implemented for T_1-T_2 maps, and an α of 10^8 was used for T_2-T_2 maps. There were 32 points in each direction of the ILT distribution for all contour maps. The following sections will discuss the intensities of peaks in 2D relaxometry contour maps. This is appropriate only because the gain was held constant, all experimental parameters were kept the same, and the ILT was implemented using the same values for experiments that were compared. Furthermore, the materials varied only as a function of age or plasticizer content. For these reasons, it is valid to consider domain intensities. Characteristic time and length scales for aged polymer 2 pseudolatex were calculated via the T_2-T_2 analysis method described in the 2D Relaxometry section

Data from the diffusion experiments was Fourier transformed in the spectral domain, and signal magnitude at each gradient value was determined by integration under the peak of interest. Diffusion coefficients were found using the Stejskal-Tanner method [14] explained in the Diffusometry section of Chapter 2.

Polymer 1 Pseudolatex

This section analyzes microscale molecular dynamics differences among polymer 1 pseudolatex batches of different ages ranging from new to approximately three years old. NMR was used with the goal of understanding the impact of the aging material on the molecular dynamics and water/polymer interactions during thermal gelation.

T_1-T_2 Studies

The polymer 1 pseudolatex samples thermally gel around 45°C so T_1-T_2 distribution maps were acquired for four samples of different ages at room temperature (22°C) and at 45°C. Table 4.1 shows the manufacturing dates of the four samples, and the first column in Figure 4.5 shows their T_1-T_2 distributions at 22°C.

Sample	**Manufacturing Date**
#5	Jan 2015
#3	April 2014
#2	June 2012
#1	Unknown, Oldest in House

Table 4.1. Ages of the polymer 1 pseudolatex samples

The experiments in this study were conducted between January and May of 2015; sample #5 is representative of fresh material. All of the samples shown in Figure 4.3 display two populations at room temperature (T_2 domains shorter than 300 µs were filtered out with a longer tau value). Molecular domains associated with longer T_2 values represent free water with some impurities, and those with shorter T_2's are related to water highly associated with the polymer as well as mobile larger molecules such as surfactant. As the samples increase in age at room T = 22°C (going down the first column in Figure 4.3), the free water population moves up in T_1 and merges with the lower mobility population in the oldest sample. This indicates a greater degree of structure in the polymer phase which allows the water to become more and more associated

with the polymer as the samples age. This property can be confirmed visually since the samples noticeably increase in viscosity with #1 appearing to be more gel-like than liquid-like.

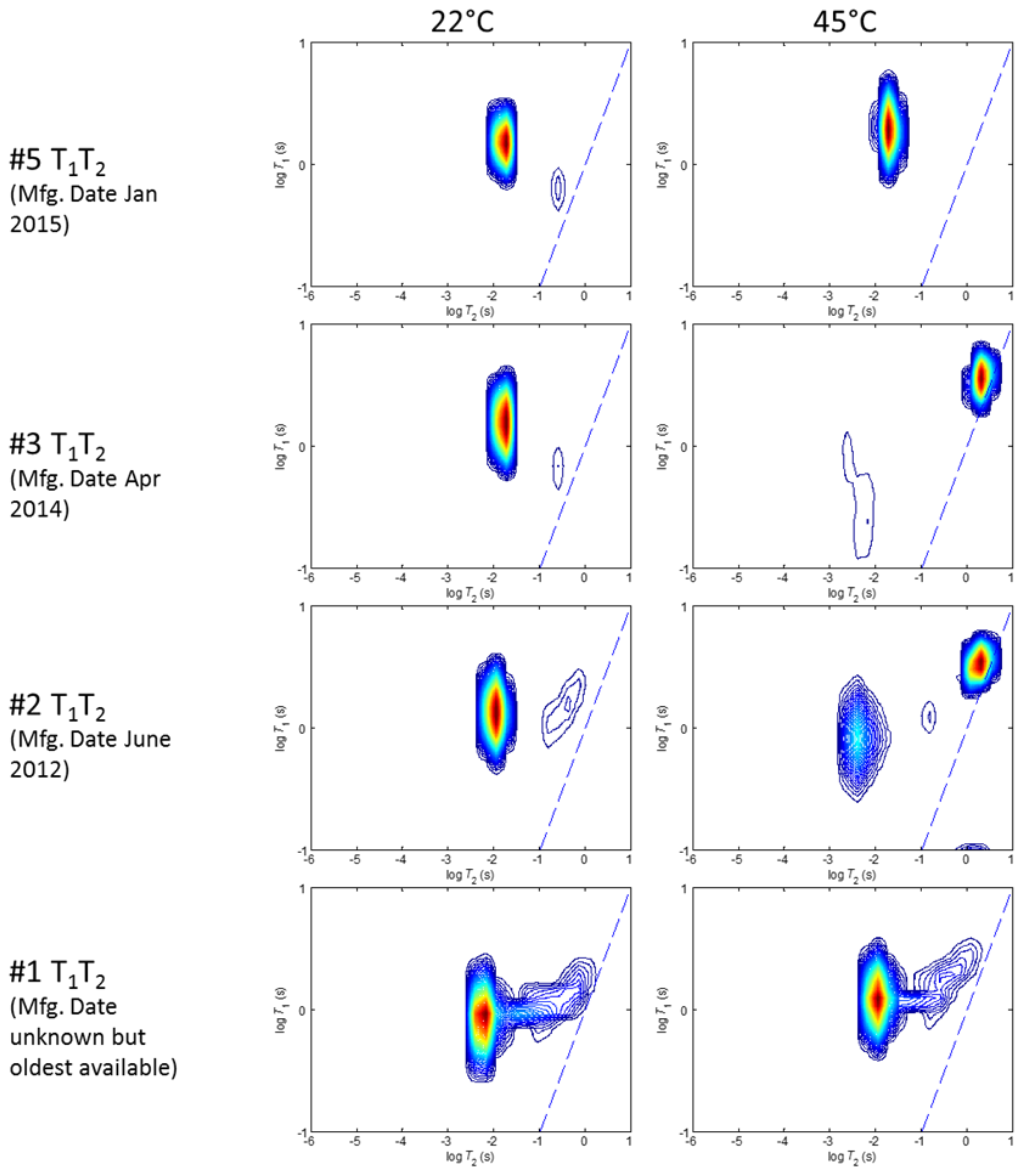

Figure 4.3. T_1-T_2 relaxation time correlation data contour plots of differently-aged polymer 1 pseudolatex samples at room temperature and at their thermal gelation temperature. The contour intensity (red highest) indicates the proportion of hydrogen spins in the sample with that magnetic relaxation behavior.

As the samples age, chemical and physical particle interactions change and cause colloidal particle aggregation. This coagulation leads to increased structure [62]. The T_1-T_2 method presented here appears to be a simple NMR test for determining a pseudolatex's gelling behavior that relates to water retention during processing.

Major differences can be seen among the samples as they thermally gel at T = 45°C (second column Figure 4.3), with the most important being the high intensity population that appears on the parity line in the maps of samples #2 and #3. During their thermal gelation, these samples not only show the expected shorter T_2 population corresponding to ordering of the colloid polymer phase [5] but also a new population of high mobility that represents free water. The thermal gelation results in expulsion of water from the gelled polymer/water phase, and this is quantified by the NMR data. The least aged sample (#5) shows no hint of the new population, and the oldest sample (#1) is already gel-like at 22°C so no significant changes are seen as it is heated to 45°C.

Figure 4.4 shows photographs before and after the thermal gelation of sample #3. It appears as a white, viscous liquid before gelation (top) then irreversibly gels into a solid spiral shape after it has been heated to 45°C (bottom).

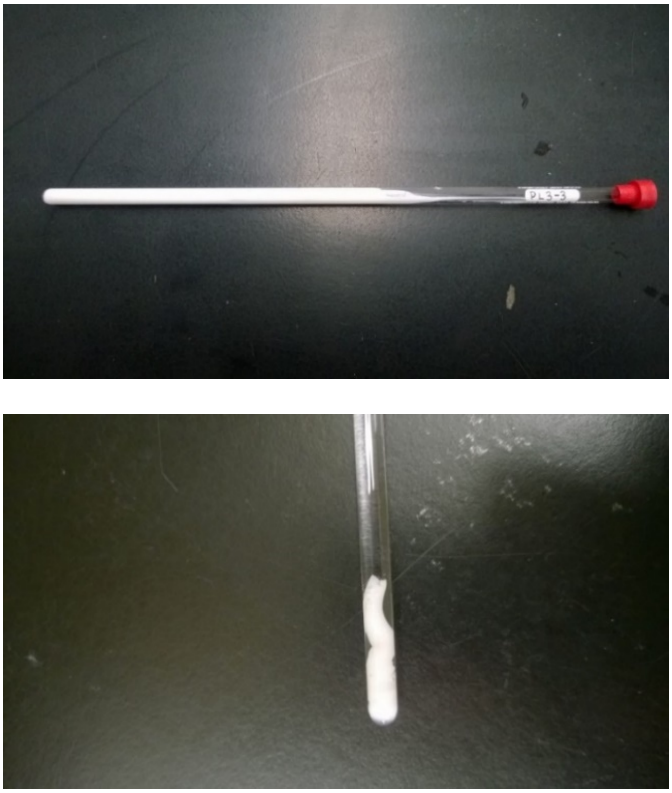

Figure 4.4. Sample #3 before (top) and after (bottom) irreversible thermal gelation.

<u>T_2-T_2 and Diffusion Studies</u>

The parity line water population seen in the T_1-T_2 maps was further studied with T_2-T_2 exchange maps and diffusion measurements. Figure 4.5 shows T_2-T_2 exchange maps at 22°C and 45°C of sample #3 and of the newest formulation, sample #5, for comparison.

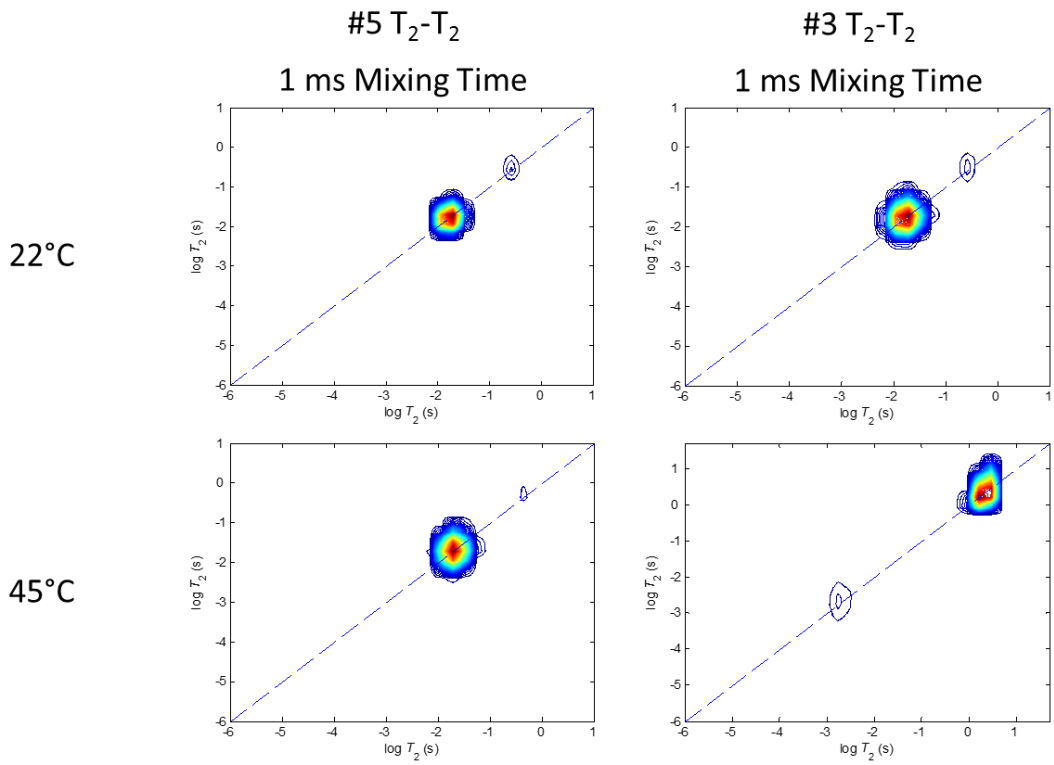

Figure 4.5. T_2-T_2 maps of the newest sample and the aged sample that thermally gels in a unique way at room temperature and at their thermal gelation temperature. The contour intensity (red highest) indicates the proportion of hydrogen spins in the sample with that magnetic relaxation behavior.

Note that the T_2 maps for sample #5 in the first column remain similar through thermal gelation; however, those for #3 change dramatically. As seen in the previous T_1-T_2 maps, sample #3 displays a significant long T_2 population as well as a short T_2 population when it thermally gels whereas #5 does not. This data demonstrates that thermal gelation in the aged sample involves an expulsion of water and a more significant separation into a polymer-rich and solvent-rich or even polymer-depleted phase than the other samples. This phase separation likely has a significant role in sample #3's material properties related to processing.

Figure 4.6 again demonstrates that sample #3 has a molecular population of high mobility that sets it apart from the other samples at 45°C. The data shown is from spectrally-resolved diffusion measurements of the water peak in the pseudolatex's NMR spectra and is normalized by the free diffusion coefficient of water at the respective temperature [64]. The data illustrates that sample #3's water phase diffusion coefficient is notably higher, equal to free water, in comparison to those of the other samples which have restricted diffusion coefficients 35% to 60% of the free water value at their thermal gelation temperature. This increased diffusion coefficient in sample #3 quantifies the more significant phase separation during gelation of this sample.

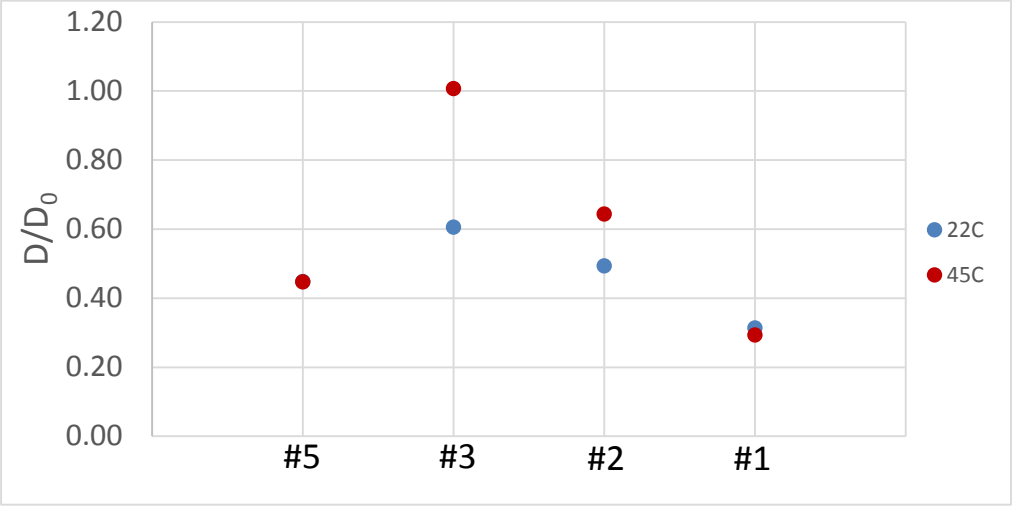

Figure 4.6. Diffusion measurements of the spectrally-resolved water peak in differently-aged samples at room temperature and at their thermal gelation temperature

Conclusions

After analyzing four polymer 1 pseudolatex samples of different ages, it was determined using T_1-T_2 maps, T_2-T_2 maps, and diffusion data that gelation is strongly dependent on aging and that sample #3 thermally gels in a different way than the other samples. As it gels, it separates into more discrete polymer and solvent water phases, evidenced by a population of water with high mobility that appears in the T_1-T_2 and T_2-T_2 maps where no such clear phase separation is seen in the oldest (#1) or newest (#5) samples. Sample #2, the sample closest in age to #3, also displays this population of mobile water, indicating that this magnetic relaxation population is connected to the pseudolatex samples being aged a specific amount of time. Diffusion coefficient measurements confirm that #3 has a domain of water with high mobility at 45°C consistent with discrete polymer and solvent water phases. Because aging destabilizes the pseudolatex and causes coagulation of particles, it can be inferred that the ability of a formulation to thermally gel in a specific way is due to the formation of aggregates pre-gelation.

Polymer 2 Pseudolatex

Pseudolatexes made using a different cellulosic ester and varying plasticizer concentrations were analyzed to compare to the gelation of pseudolatex 1. Table 4.2 indicates sample names and their plasticizer contents. Similarly to polymer 1 pseudolatex, this formulation destabilized with age as hydrolysis occurred so aging effects were investigated as well. Two-dimensional NMR relaxation experiments were used along with diffusion measurements to elucidate the molecular interactions of the different samples.

Sample	Plasticizer wt%
A	0%
E	2.24%
F	2.5%

Table 4.2. Polymer 2 pseudolatex samples and their associated plasticizer concentrations

Thermal Gelation Model

At 22°C, the T_1-T_2 maps of the three samples having varied plasticizer contents appear very similar. Figure 4.7 displays a map from sample F representative of all the pre-gelled samples along with a conceptual model that describes the microstructure of the samples. At this temperature, the colloidal particles exist in an ungelled state surrounded by free water. That free water is seen in the longest T_2 domain of the contour map with a reduced T_1 and T_2 relative to pore water due to solubilized species such as surfactant or plasticizer. The pseudolatex particles themselves (shown larger in the upper left) contain a core of polymer surrounded by surfactant which stabilizes the particles. The sufactants align such that their hydrophobic heads are near the polymer core and their hydrophilic tails reach outward towards the free water. The peak with a slightly shorter T_2 than the free water represents highly restricted water and mobile larger molecules, as evidenced by spectrally-resolved diffusion data.

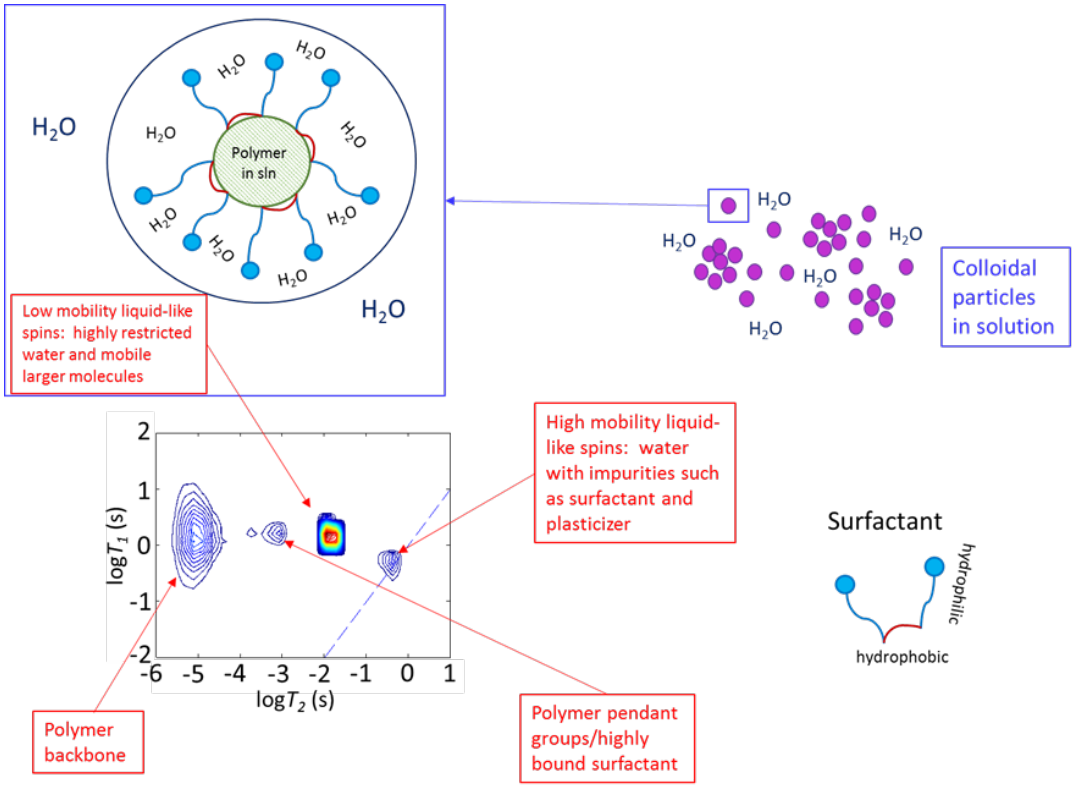

Figure 4.7. Conceptual model of ungelled polymer 2 pseudolatex solutions at 22°C with representative T_1-T_2 relaxation correlation data for sample F shown.

A spectrum from one diffusion experiment of unaged sample F taken at a gradient value of 0.07 T/m is shown in Figure 4.8. With a tau time of 2.12 ms in spectrally-resolved diffusometry experiments, a water peak and a peak pertaining to molecules with proton resonance shifts from water were observed and are shown in Figure 4.8.

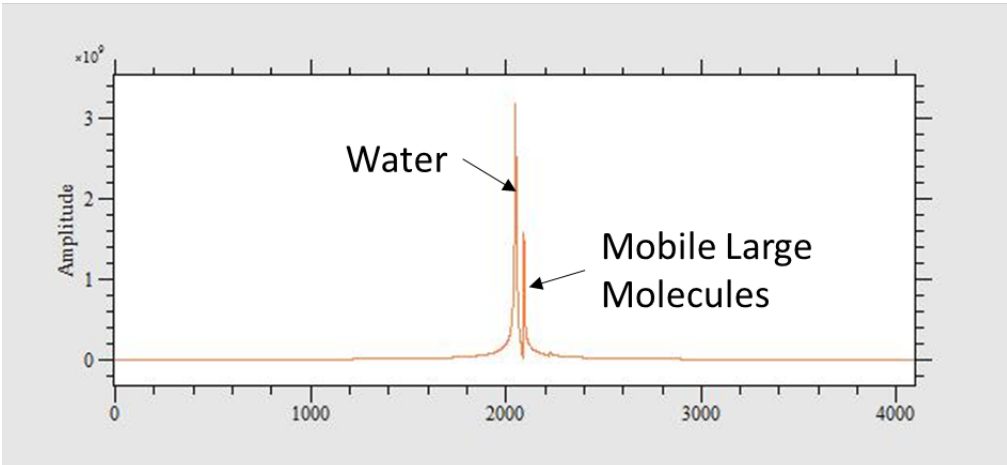

Figure 4.8. Spectrally-resolved diffusion experiments inform which molecules reside in T_1-T_2 data domains. The spectrum shows data from unaged sample F at a gradient value of 0.07 T/m.

The diffusion coefficient of those less mobile molecules (D ~ 10^{-11} m^2/s) was found to be two orders of magnitude lower than that of the water (D ~ 10^{-9} m^2/s). Because the domain to the left of the free water peak in the T_1-T_2 map has a T_2 of about 10 ms, a value greater than the diffusometry tau time of 2.12 ms, those large, low mobility molecules contribute to the relaxation signal at T_2 ~ 10^{-2} s. The domain with a T_2 of approximately 1 ms arises from polymer pendant groups and possibly highly bound surfactant, and the peak with the shortest T_2 value comes from the polymer backbone protons.

When the polymer 2 pseudolatex solutions are heated, they thermally gel. Figure 4.9 shows a model of the gelled state for the aged, plasticized samples along with an illustrative T_1-T_2 correlation data set for sample F obtained at 56°C. The sample has expelled water and effectively increased the particle volume fraction in the gel. The colloidal polymer particles are packed more tightly than they were at 22°C, and there are now two phases. However, the samples for all experiments in this section were placed such that the free expelled water existed above the active region of the RF coil so no signal from it was collected as shown in Figure 4.2.

Thus the T_1-T_2 correlation data reflect only the molecular dynamics of the gel phase. The longest T_2 population corresponds to water entrained within the gel. This population has shifted off the parity line in Figure 4.7 to lower T_2 and high T_1. T_1 increase is indicative of proton ordering. As in the 22°C map, the population with a slightly shorter T_2 relates to low mobility liquid-like spins including highly restricted water and mobile larger molecules and remains at a similar T_1 and T_2. The shortest T_2 domain again arises from the polymer backbone, and the population to its right the polymer pendant groups as well as tightly bound surfactant molecules.

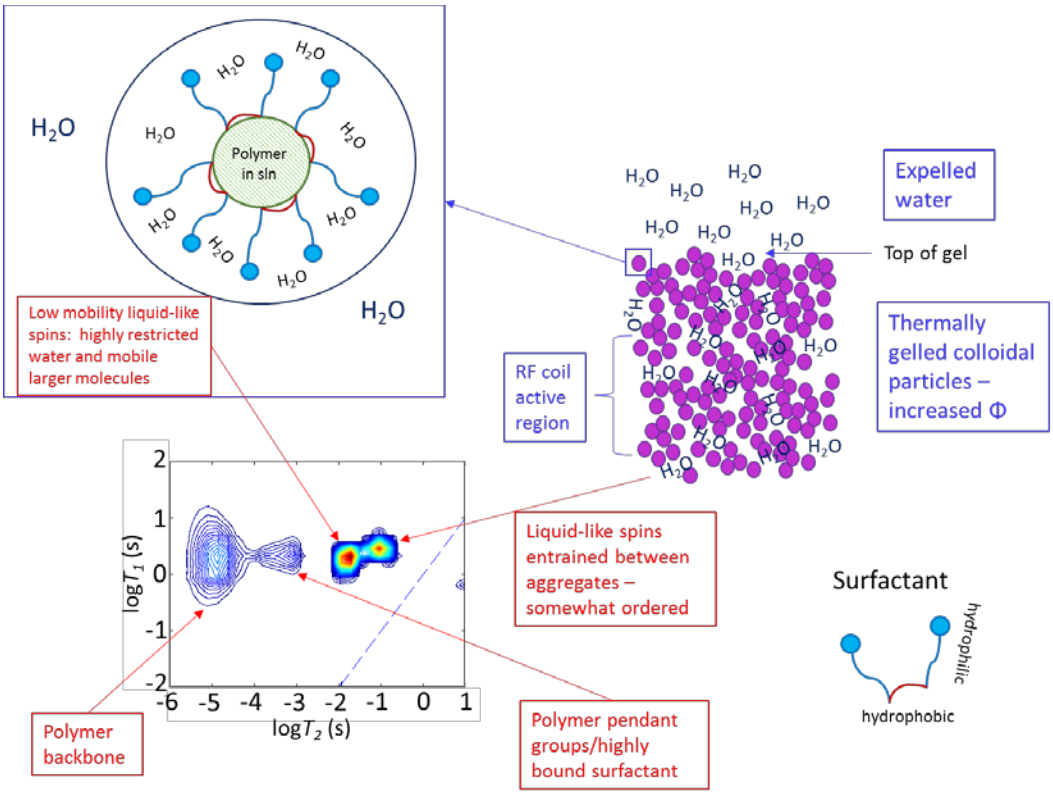

Figure 4.9. Conceptual model of gelled polymer 2 pseudolatex with representative T_1-T_2 data from sample F at 56°C.

Figure 4.2 displays pictures of actual polymer 2 pseudolatex samples in their test tubes before and after gelation. The images can be compared to Figures 4.7 and 4.9. The pre-gelled sample appears as a homogeneous white liquid, and the gelled sample has clearly phase separated into a water and a polymer particle-rich phase.

Plasticization

Plasticization mechanisms are difficult to define because the behavior of the plasticizer is highly dependent upon the system in which it is included [65]. In plasticization of polymer dispersions, the plasticizer partitions into the colloidal particles, softens them, and promotes deformation. This effect assists in applications such as film formation, and once the film is dry, plasticizer alters the polymer intermolecular forces in such a way that the material is flexible and less brittle [66]. Given the above information, it can be surmised that plasticization mimics the effects of aging in this colloidal dispersion. Just as ester hydrolysis produces free acid which alters the surface charges of the particles and causes them to aggregate, plasticizer likely also alters the surface properties and causes an analogous coagulation effect.

T_1-T_2 Studies

Let us first explore the irreversible thermal gelation of a plasticized, aged sample. Figure 4.10 shows T_1-T_2 maps as a function of temperature for sample F (2.5% plasticizer) aged 2 months.

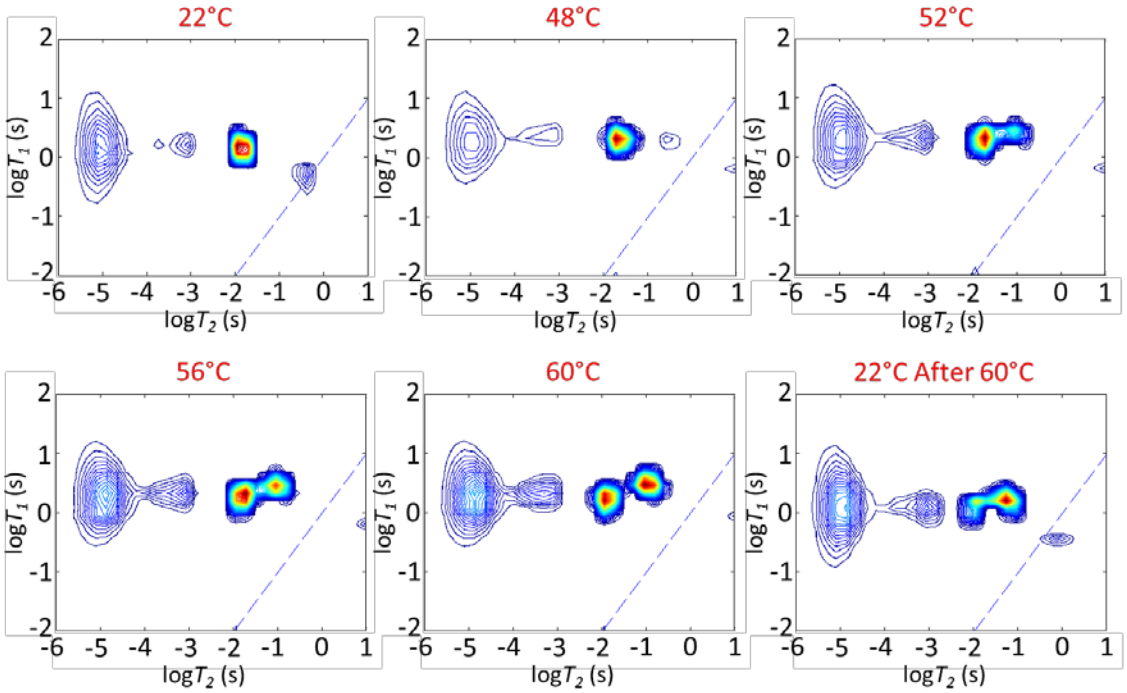

Figure 4.10. T_1-T_2 magnetic relaxation correlation data of the thermal gelation of sample F (2.5% plasticizer) aged 2 months. The sample was equilibrated for at least 30 minutes at each temperature before data acquisition. The contour intensity (red highest) indicates the proportion of hydrogen spins in the sample with that magnetic relaxation behavior.

At 22°C, the sample exists as a homogeneous liquid and the T_1-T_2 correlation data displays the characteristics shown in the Figure 4.7 model. As it begins to gel at 48°C, a high mobility domain with a T_2 of about 500 ms is seen. This population represents water being entrained within the gel as it forms. Phase separation is beginning to occur, but no signal from the expelled water is collected since it is outside of the RF coil active region as shown in Figure 4.2. Notice that the entrained water population becomes more intense, moves to shorter T_2 values, and moves up in T_1 as temperature is increased further. All of these changes indicate increased order and particle density in the polymer-rich phase as the sample phase separates into a gel and expelled solvent water. During heating, the two short T_2 populations corresponding to polymer and

highly bound surfactant merge, demonstrating the overall densification of the particles as their volume fraction increases in the gel phase. When the sample is brought back to room temperature post-gelation, the irreversible nature of the process can be seen. The entrained water population and the merging of the two short T_2 populations not visible in the pre-gelation 22°C map are evident in the 22°C after 60°C experiment.

Unlike the previous example, the sample we will now examine does not form gels sufficiently well for processing. In Figure 4.11, sample A (0% plasticizer) aged for about 2 months is brought from room temperature to 60°C.

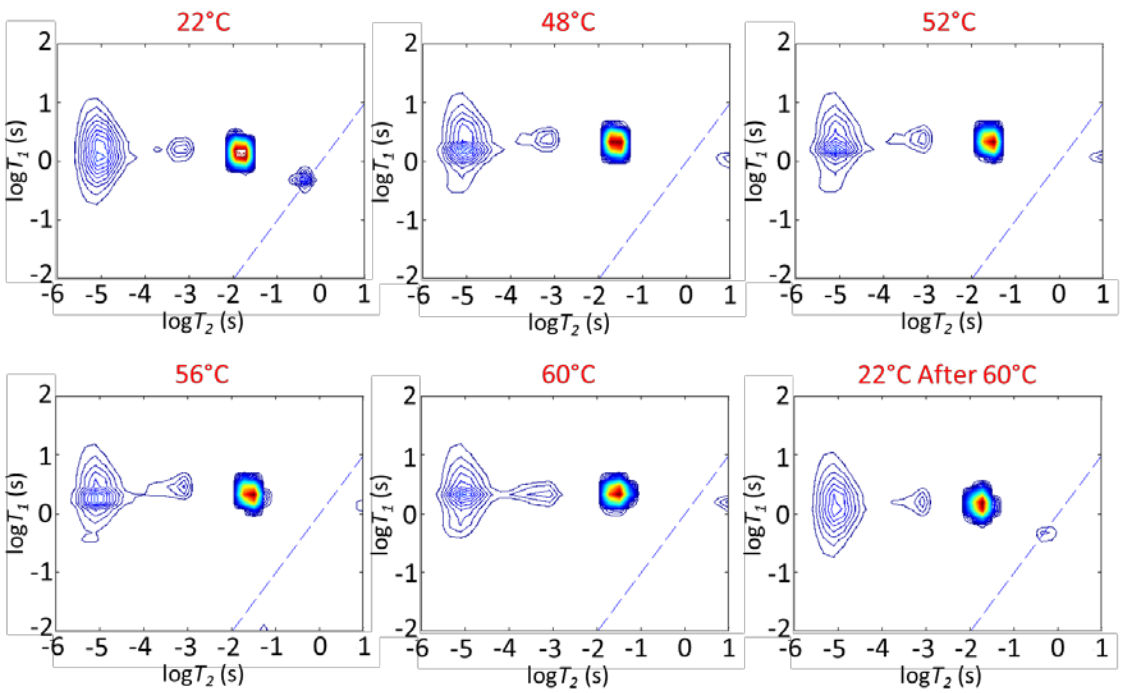

Figure 4.11. Sample A (0% plasticizer) aged 2 months does not exhibit the same T_1-T_2 populations as sample F (2.5% plasticizer) aged 2 months (Figure 4.10) when heated. The sample was equilibrated for at least 30 minutes at each temperature before data acquisition. The contour intensity (red highest) indicates the proportion of hydrogen spins in the sample with that magnetic relaxation behavior.

The room temperature data is quite similar to that of sample F, but significant differences are seen when A is raised to higher temperatures. The entrained water population does not emerge in the maps at all, and it was found when examined visually that A had not separated into a gel and expelled water phase. Notice that the 22°C after 60°C map appears almost identical to the map acquired pre-heating, indicating that no irreversible gelation occurred. This data raises the question of what happened to the long T_2 population seen at 22°C but not visible at any of the higher temperatures. Because these experiments were run with a τ of 9.6 µs and 14,000 echoes to give an acquisition time of 270 ms, they could have failed to resolve populations with T_2's longer than this value. More data must be collected to investigate this idea, but since all T_1-T_2 correlation experiments in this section were run with the same values, it can be concluded that sample F does indeed show an entrained water population that A does not.

In the polymer 1 pseudolatex, pre-formed aggregates arising from the aging process were necessary to form a gel with good mechanical processing properties. Polymer 2 pseudolatex is slightly more stable due to steric hindrance from its large substituent group but still experiences coagulation due to ester hydrolysis over time [62]. It was surmised that an aged sample with no plasticizer would show thermal gelation markers in its T_1-T_2 maps, and this hypothesis proved correct as shown by Figure 4.12.

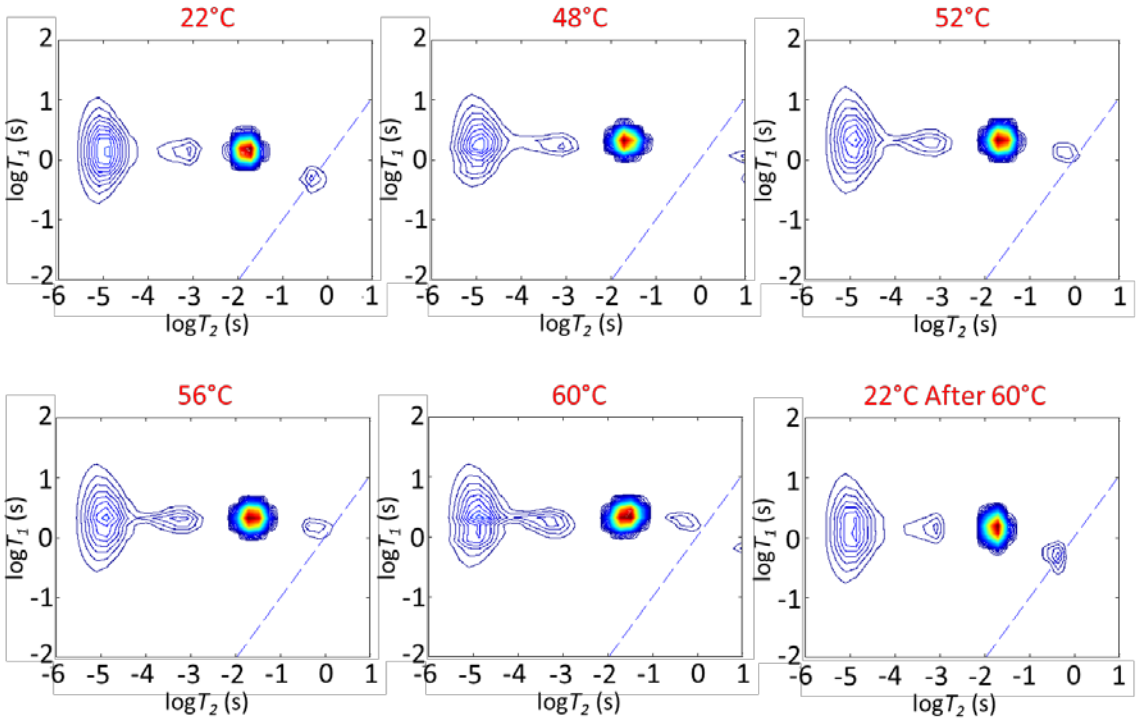

Figure 4.12. Thermal gelation of sample A (0% plasticizer) aged 4.5 months. The sample was equilibrated for at least 30 minutes at each temperature before data acquisition. The contour intensity (red highest) indicates the proportion of hydrogen spins in the sample with that magnetic relaxation behavior.

The data was collected after unplasticized sample A had been aged for 4.5 months. In these experiments, the pseudolatex gained the reduced T_2 entrained water peak indicative of a phase separation and thermal gelation. The peak is notably less intense than that seen in aged sample F upon heating (Figure 4.10), but the aging process clearly changed the microstructure of the dispersion in such a way that it did form a polymeric particle gel structure that entrained water. However, the data taken at 22°C after 60°C is indistinguishable from that taken prior to heating. The entrained water peak does not remain as it did in aged sample F. It is presumed that this aged sample A had only a few, small aggregates prior to thermal gelation and weakly gelled.

Let us now further investigate the effects of plasticizer addition. Figure 4.13 shows T_1-T_2 data of unaged sample F as it is heated.

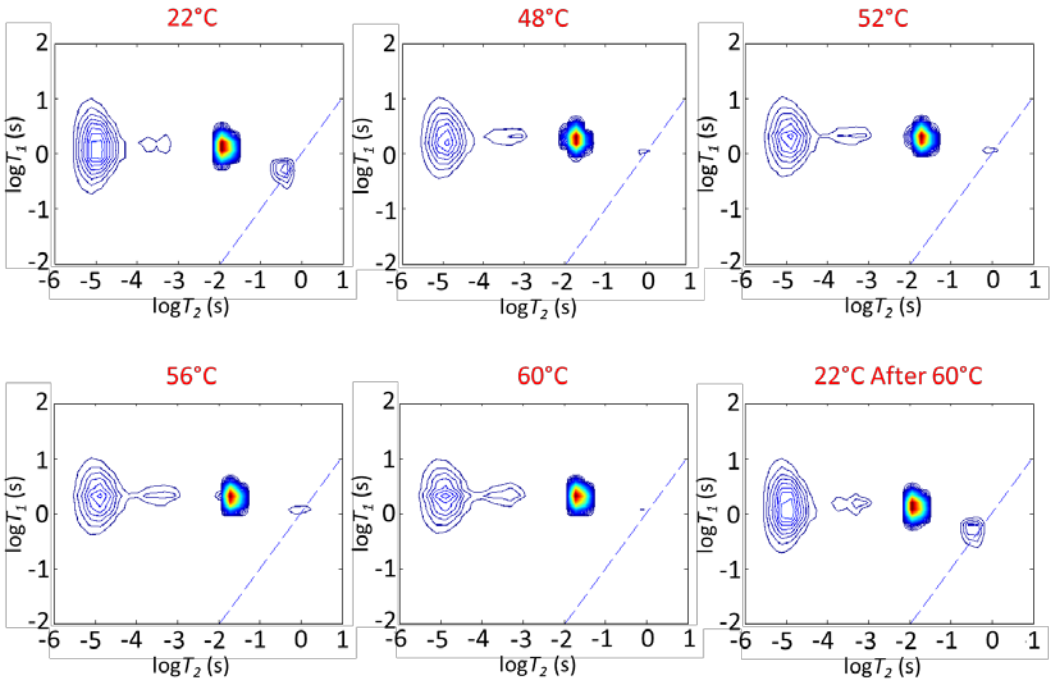

Figure 4.13. Unaged sample F (2.5% plasticizer) T_1-T_2 correlation data. The sample was equilibrated for at least 30 minutes at each temperature before data acquisition. The contour intensity (red highest) indicates the proportion of hydrogen spins in the sample with that magnetic relaxation behavior.

This new F sample does not appear to thermally gel since it displays a small long T_2 population that does not move off the parity line as the temperature is raised. Furthermore, the data taken at 22°C after the sample had been raised to 60°C is nearly identical to the data taken before heating at 22°C, demonstrating that the sample did not irreversibly gel.

Figure 4.14 displays similar T_1-T_2 maps of new sample E which contains 2.24% plasticizer. As with new sample F, the data does not show thermal gelation markers.

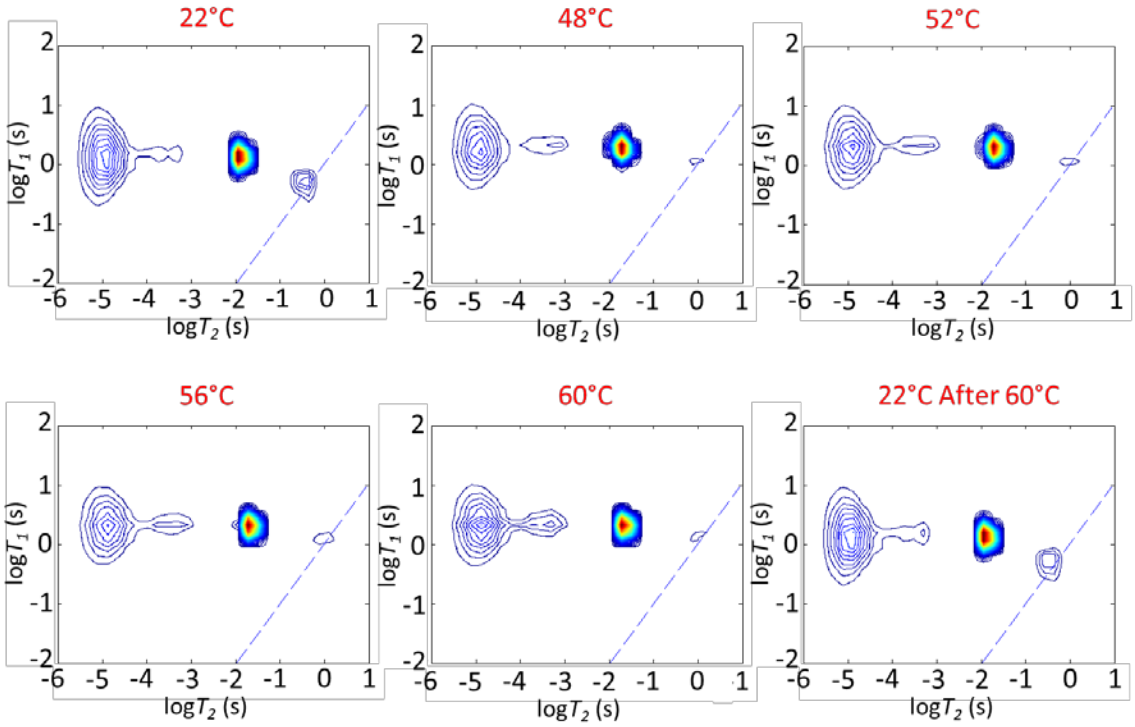

4.14. Unaged sample E (2.24% plasticizer) does not show thermal gelation markers. The sample was equilibrated for at least 30 minutes at each temperature before data acquisition. The contour intensity (red highest) indicates the proportion of hydrogen spins in the sample with that magnetic relaxation behavior.

The high mobility entrained water population clearly plays a role in thermal gelation. Figure 4.15 depicts how aging affects the long T_2 domain; it moves up in T_1 and becomes more intense with age. It has been established that more/larger aggregates form at room temperature as the pseudolatex ages, and these maps can be interpreted in the context of this pre-gelation coagulation.

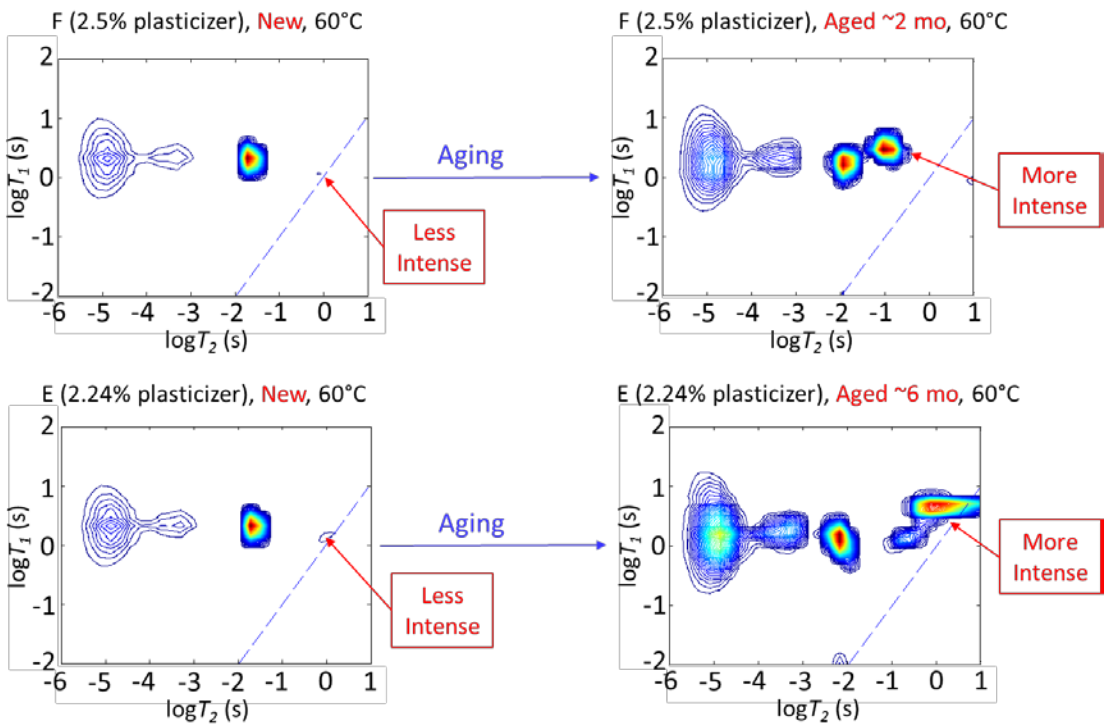

Figure 4.15. The high mobility entrained water domain becomes more intense and changes position with aging. The samples were equilibrated for at least 30 minutes at each temperature before data acquisition. The contour intensity (red highest) indicates the proportion of hydrogen spins in the sample with that magnetic relaxation behavior.

When a few small aggregates and many free colloidal particles gel, thermal gelation markers are not seen as shown in the two maps on the left. When many large aggregates gel, they form large domains of entrained water which exhibit a great deal of structure, demonstrated by the map on the upper right with an entrained water peak displaying shorter T_2 and longer T_1 values. After 6 months of aging (lower right map), the pseudolatex forms a gel with entrained water domains having such high mobility that its T_1-T_2 map shows an intense population of water that lies nearly on the parity line. The domain below this high mobility population likely corresponds to entrained water in smaller pores with slightly less mobility.

Figure 4.16 demonstrates changes in the long T_2 peak with plasticizer content.

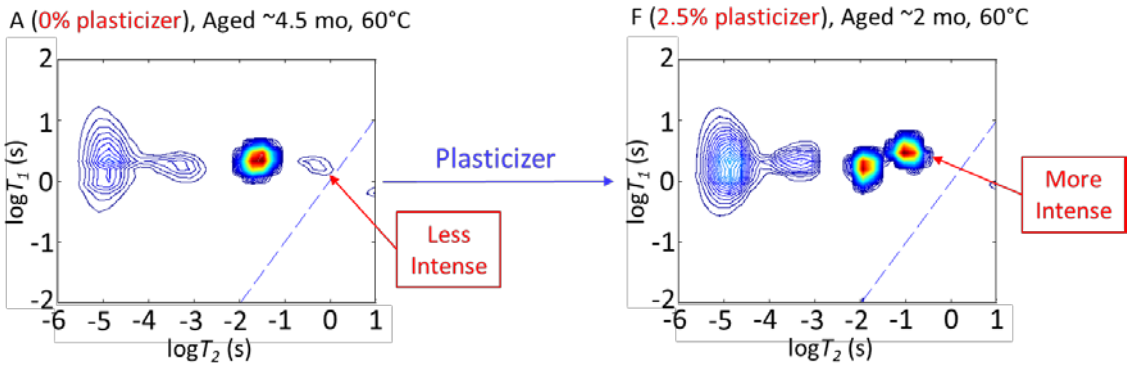

Figure 4.16. The entrained water domain becomes more intense and changes location with added plasticizer. The samples were equilibrated for at least 30 minutes at each temperature before data acquisition. The contour intensity (red highest) indicates the proportion of hydrogen spins in the sample with that magnetic relaxation behavior.

In the unplasticized sample that had been aged long enough to form aggregates prior to thermal gelation, the entrained water peak displays low intensity and a T_1 similar to that of the other populations. In contrast, the plasticized and aged sample has an extremely intense entrained water peak with a longer T_1 which can be indicative of structure when T_2 is decreasing and a significant phase separation. Several pieces of information can be garnered from this data. First, the addition of plasticizer to a sample clearly leads to large domains of entrained water in the gel. Second, plasticizer appears to enhance the aging process. Notice that the sample with no plasticizer that had been aged for 4.5 months displays signs of fewer, smaller aggregates whereas the plasticized sample that had been aged for only two months shows a high mobility domain arising from a great deal of large aggregates formed pre-gelation. The map of the same plasticized but new sample (Figure 4.13) does not show populations indicative of thermal gelation in its T_1-T_2 data. After 2 months of aging, the sample had evidently aggregated a great deal more than the unplasticized sample had after 4.5 months. This effect is likely due to

plasticizer segregating into the particles and allowing water to enter them more easily. With more water contacting the polymer core, hydrolysis and its associated aggregation would occur more quickly.

T_2-T_2 Studies

T_2T_2 exchange data was acquired for sample F that had been aged for 3 months, thermally gelled, then stored at ambient temperature for another 3 months. The sample's T_1-T_2 map at 22°C post-gelation is displayed in Figure 4.17, showing the proton magnetic relaxation populations of an irreversibly gelled pseudolatex.

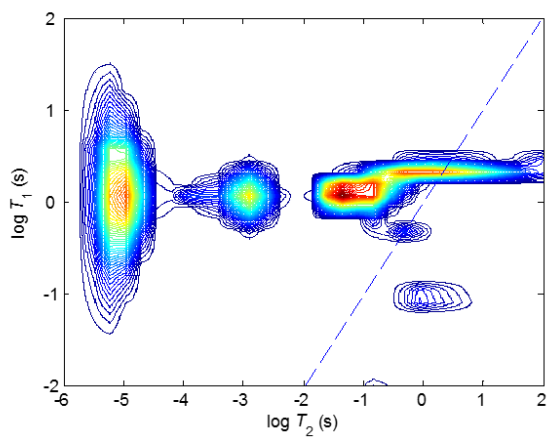

Figure 4.17. T_1-T_2 map of aged sample F at 22°C after thermal gelation at 60°C. The sample was equilibrated for at least 30 minutes at each temperature before data acquisition. The contour intensity (red highest) indicates the proportion of hydrogen spins in the sample with that magnetic relaxation behavior.

T_2-T_2 data was acquired for various mixing times and the cross peak intensity data analyzed as discussed in Chapter 3. The results are shown in Figure 4.18 for the sample at 60°C and the gelled sample at 22°C. Examples of the T_2-T_2 data for two mixing times are shown in Figure 4.19 at T = 22°C. The shortest T_2 polymer backbone population spread in the second dimension

results from sampling that dimension with a number of points less than that used in the first dimension. Exchange between the two mid-range populations at T_2 ~ 100 ms and 1 ms that lie in the middle of the domains of shortest and longest T_2 values was studied. These populations represent highly bound molecules and low mobility liquid-like spins. Thus mixing between them can be interpreted as translational diffusion between domains extremely close to the polymer and domains slightly removed but with less mobility than that of entrained water. Notice in Figure 4.19 the clear off-diagonal peaks that form after a mixing time of 200 ms.

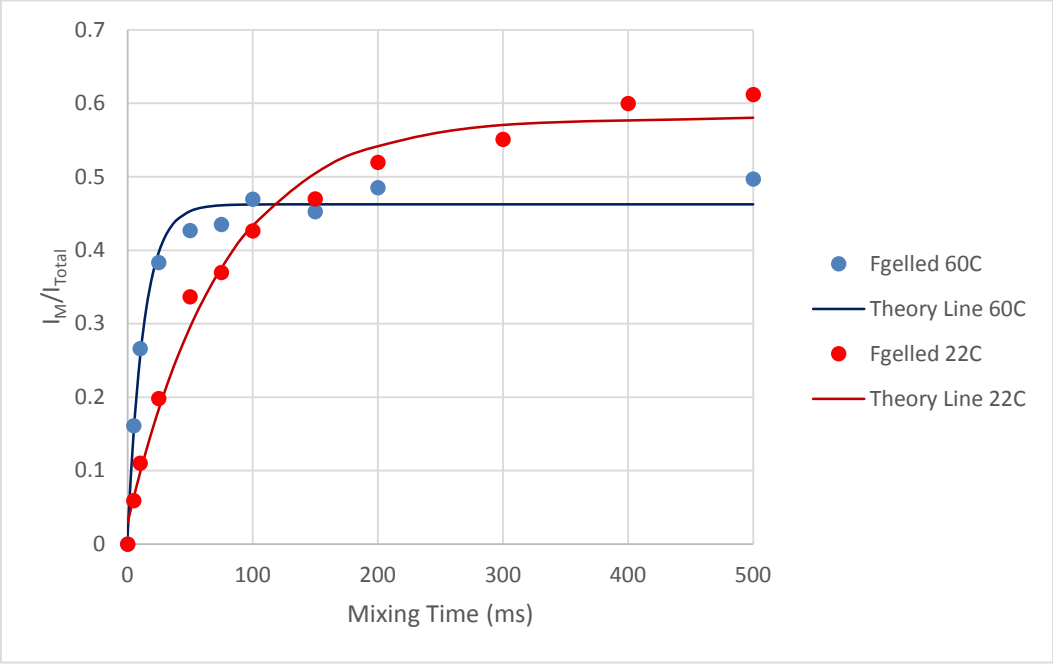

Figure 4.18. T_2-T_2 analysis at 22°C and 60°C for gelled sample F aged 6 months total

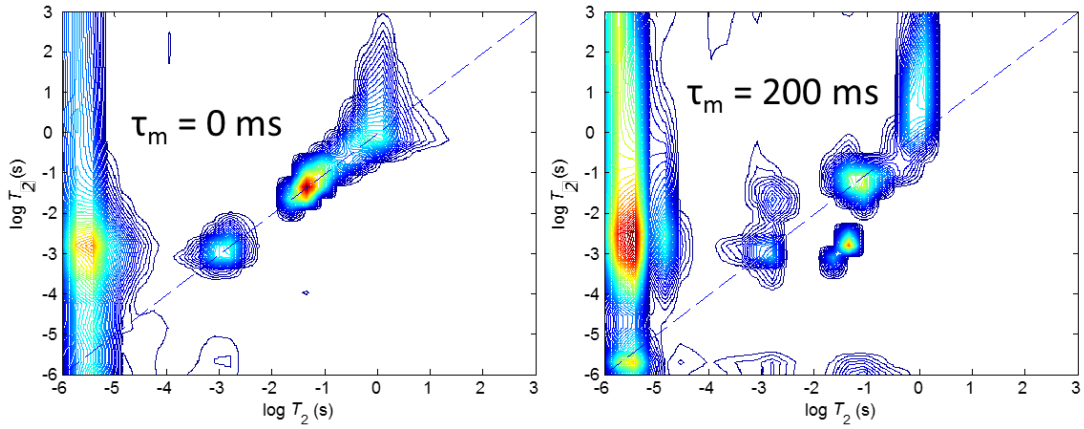

Figure 4.19. T_2-T_2 maps of aged sample F post-thermal gelation at 22°C. A short mixing time (0 ms) is shown on the left and a long mixing time (200 ms) displayed on the right. The contour intensity (red highest) indicates the proportion of hydrogen spins in the sample with that magnetic relaxation behavior.

After performing a T_2-T_2 data exchange analysis, it was determined that τ_c for the sample at 60°C was 12.87 ms $\pm$ 3.85 ms and τ_c at 22°C was 75.85 ms $\pm$ 18.02 ms. By using independently-acquired water diffusion coefficient values, length scales for the sample at the two temperatures were found to be 12.6 µm $\pm$ 2.0 µm and 19.2 µm $\pm$ 2.4 µm for 60°C and 22°C respectively. Because of the irreversibility of the gelation, it was expected that they would be nearly the same which they are, but they clearly indicate a swelling of the gel structure. The T_2-T_2 measurements indicate that the gel is stable and maintains its structure after thermal gelation when subject to thermal cycling. This characteristic length scale of about 15 µm is difficult to interpret but may be indicative of the structure of the gel .

Diffusion Studies

The effects of plasticizer content and age on molecular dynamics of polymer 2 pseudolatex were further studied with diffusometry. Figure 4.20 quantifies values for diffusion

coefficients at 60°C of the water peak in samples having various ages and plasticizer contents. The values are normalized by the free diffusion coefficient of water at 60°C, 4.31×10^{-9} m^2/s [64].

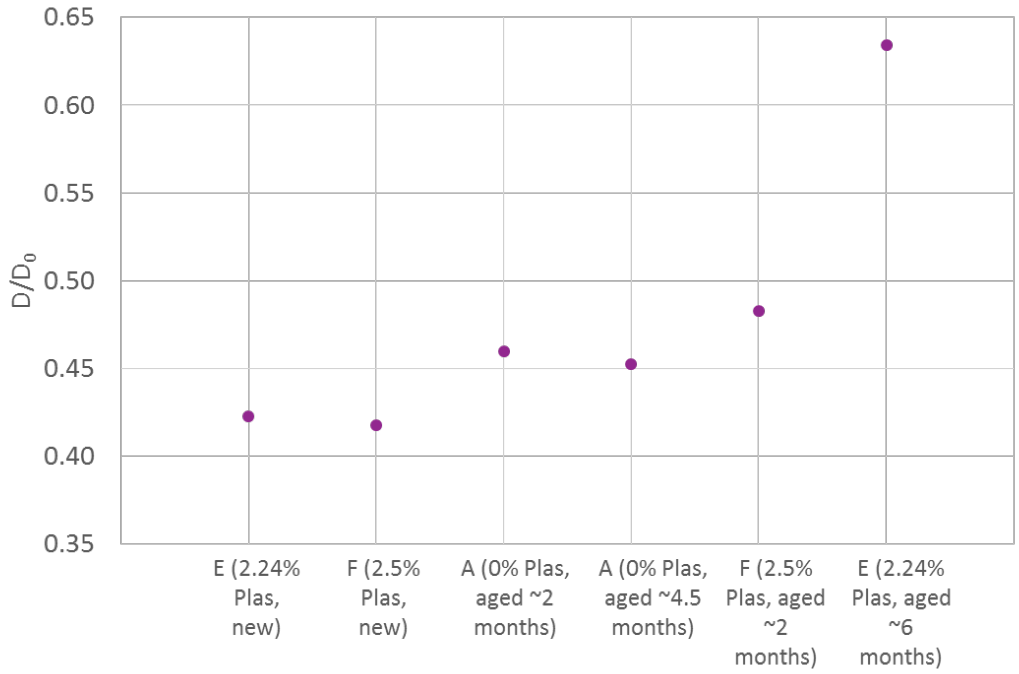

Figure 4.20. Water spectral peak diffusion coefficient measurements at 60°C normalized by the diffusivity of pure water at 60°C, $D_0 = 4.31 \times 10^{-9}$ m^2/s

Many of the dispersions exhibit relatively similar diffusion coefficient values with a general increase as a function of plasticizer and aging. Recall the larger entrained water populations in the T_1-T_2 maps of aged E and F at 60°C (Figure 4.15) and note that those two samples have the largest diffusion coefficients. Because D/D_0 is less than 1 for all measurements, the entrained water in these samples cannot diffuse freely as it would in a pure liquid environment due to the colloid particle phase, but the water in F and E gels is more mobile in comparison to that residing in the other samples. This supports the idea that increased age and plasticizer content

lead to a more significant thermal gelation phase separation into a gel phase containing high mobility entrained water and an expelled water phase. The increased diffusion coefficients of aged E and F indicate that they form gels with larger, more mobile entrained water domains than the newer or unplasticized samples.

Figure 4.21 displays water peak diffusion coefficients as a function of temperature for samples F, E, and A. Sample F had been aged for about 2 months (T_1-T_2 maps in Figure 4.10), sample A had not been aged enough to form pre-gelation aggregates (T_1-T_2 maps in Figure 4.11), and sample E had been aged for about 6 months (T_1-T_2 map in Figure 4.15). The diffusion coefficients are normalized by the free diffusion coefficient of water at each temperature [64].

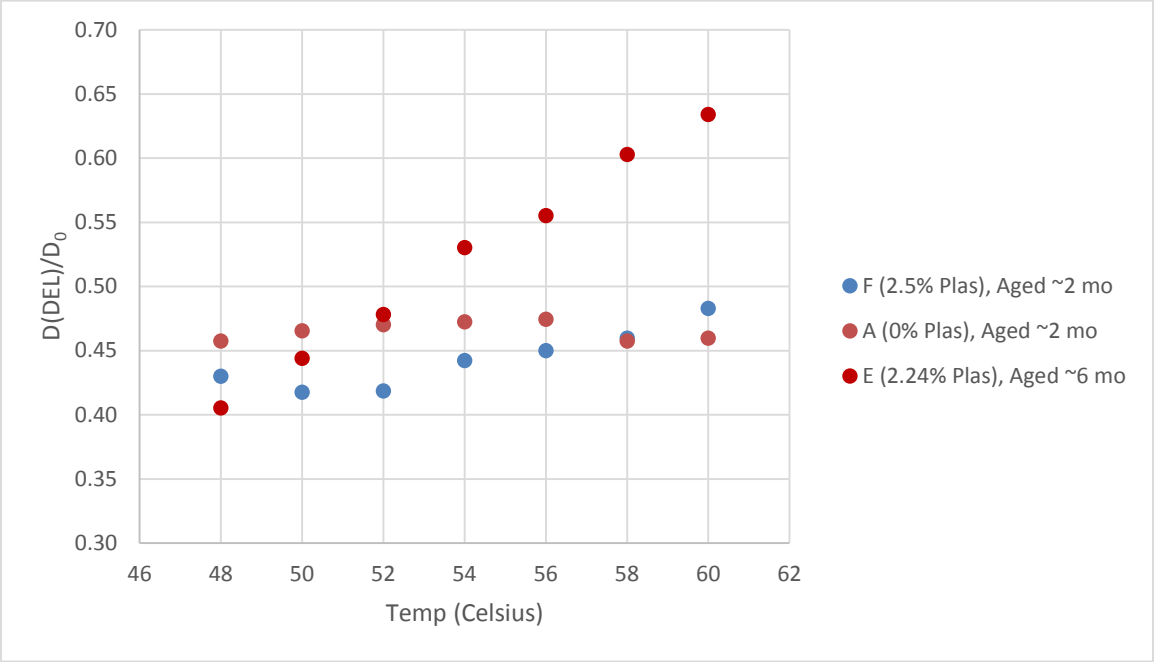

Figure 4.21. Water peak diffusion coefficients as a function of temperature for polymer 2 pseudolatex samples

For samples E and F, $\frac{D(\Delta)}{D_0}$ tends towards increasing values as temperature is increased. This trend can be attributed to the formation of entrained water populations as the pseudolatexes gel. Water within the gels is in larger domains and causes the diffusion coefficient to tend towards that of free water. The normalized water diffusion coefficient of sample A, however, exhibits no appreciable changes when temperature is raised, once again indicating that A does not phase separate and thermally gel upon heating.

Conclusions

After analysis of the T_1-T_2, T_2-T_2, and diffusion data, it was apparent that plasticization and aging cause changes in polymer 2 pseudolatex microstructure which allow the colloidal dispersions to undergo significant phase separation and therefore irreversible thermal gelation upon heating. Using knowledge of the pseudolatex aging process [62] and the idea that plasticization alters interparticle charges [66], it was established that pre-formed aggregates are necessary for thermal gelation to take place. These aggregates trap water upon thermal gelation and cause a long T_2 entrained water domain to be seen in high temperature T_1-T_2 maps. Because older, more plasticized samples exhibit more intense entrained water populations, it was concluded that more plasticizer or longer aging cause the formation of additional, larger aggregates prior to gelation. This effect leads to a gel having large entrained water domains post heating whereas new or unplasticized samples do not appear to thermally gel at all in terms of the proton relaxation populations present. T_2-T_2 measurements were utilized to determine a characteristic length scale of a gel formed with an aged, plasticized sample. The analysis yields similar values for the sample at both 60°C and 22°C, confirming the irreversibility of the gelation process. Diffusion measurements provided more evidence of a significant phase

separation during thermal gelation in samples with pre-formed aggregates. The plasticized, aged samples showed increased water diffusion coefficients at 60°C because of their entrained water populations, and their diffusion coefficients increased with increasing temperature as high mobility water domains formed while those of a new, unplasticized sample remained constant. Using all of the above evidence, it can be concluded with a high degree of certainty that coagulation of polymer colloidal dispersions prior to thermal gelation is necessary for the formation of a strong gel upon heating.

Although experiments in this chapter allow some conclusions to be drawn, more work must be done using T_1-T_2 experiments with different parameters, rheology data in conjunction with NMR data, and further diffusion experimentation. With these techniques, the thermal gelation mechanism of polymer colloidal dispersions will be understood more clearly.

DRIED POLYMER FILMS

This chapter will present data on polymeric films of a type that are often made from the pseudolatex systems of the previous chapter. Two polymer films made from different polymer formulations (formulation 1 and formulation 2) are analyzed. Polymer formulation 1 is of a larger average size than polymer formulation 2, and the different polymer formulations generate different mechanical properties in dry films. T_1-T_2 correlation and T_2-T_2 exchange experiments are applied to investigate whether mobile proton populations are measurable that would indicate how residual relative humidity water in the films might impact the film properties.

Methods

Sample Preparation

The samples studied here were made by dispersing the two different polymer formulations in water. De-ionized water was heated to 60°C with constant stir bar agitation, then the polymer powder was slowly sprinkled into the water over the course of one to two minutes until a concentration of 19 wt% polymer was attained. The dispersion was cooled to room temperature while maintaining constant agitation whereupon the polymer hydrated and the mixture thickened. The stir bar speed was adjusted to sustain agitation with the more viscous solution. Finally, the sample was covered and allowed to stir for twenty-four hours before analysis. The solutions were placed into 5 mm glass NMR tubes using the same vacuum method described in the Sample Preparation section of the Pseudolatex chapter.

Dry films were obtained and cut into small squares then placed as homogeneously as possible into 5 mm glass NMR tubes.

2D Relaxometry Measurements

Measurements were made on a Bruker Avance III NMR spectrometer at a ^{1}H resonance frequency of 250.12 MHz with a Bruker high power probe base and its attached 5 mm birdcage RF coil. For T_1-T_2 measurements of the wet polymer mixtures, a tau time of 36 µs was implemented to resolve the shortest T_2 polymer populations. This value corresponded to a dwell time of 1.5 µs to give 23 dwells per tau. 10,000 echoes were required to reach the noise, and these parameters yielded an acquisition time of 720 ms. The dry films contained domains of shorter T_2 values so their T_1-T_2 experiments applied a shorter tau time of 9.6 µs. The dwell time for these experiments was 0.4 µs, and only 2,000 echoes were necessary to reach noise. The acquisition time was 38.4 ms. The T_2-T_2 exchange experiments on the dry films also utilized a tau of 9.6 µs, a dwell time of 0.4 µs, and 2,000 echoes. The first T_2 encoding period cycled the number of echoes through a list of 64 logarithmically spaced numbers between 0 and 1,000.

Temperature Control

Although all of the experiments in this study were run at room temperature (22°C), the *BVT3000* temperature control unit was always on due to the dangers of heating due to RF power deposition from applying CPMG pulse trains rapidly. The unit used flowing nitrogen gas that was pre-chilled by the BCU II.

Data Analysis

The T_1-T_2 relaxation correlation and T_2-T_2 exchange contour maps were generated using the 2D inverse Laplace transform (2D ILT) software discussed in the 2D Relaxometry section of Chapter 2. The inversion revealed domains of different mobilities from the multi-exponential raw data. After running α-loops, it was determined that the optimal smoothing parameter value was 10^8 for T_2-T_2 maps and 10^7 for T_1-T_2 maps. There were 32 points in each direction of the ILT distribution for all maps. Characteristic time scales for the dry films were calculated via the T_2-T_2 analysis described in the 2D Relaxometry section. A two-site exchange model was assumed, and the gain was kept constant in order to minimize unwanted intensity variation among data sets of different mixing times. Seven different experiments with mixing times ranging from 0 ms to 200 ms were acquired for each dry film polymer formulation.

Wet Polymer Formulations

T_1-T_2 experiments were run on the 19 wt% polymer formulations at 22°C to produce the data shown in Figure 5.1. Both formulations show domains characteristic of polymer/solvent mixtures. The most intense population with the longest T_2 represents mobile solute water, the one with the shortest T_2 arises from polymer signal, and the one in the middle signifies protons on water that are highly associated with the polymer and mobile polymer pendant groups. No significant differences can be seen between these two formulations in terms of T_1-T_2 correlation.

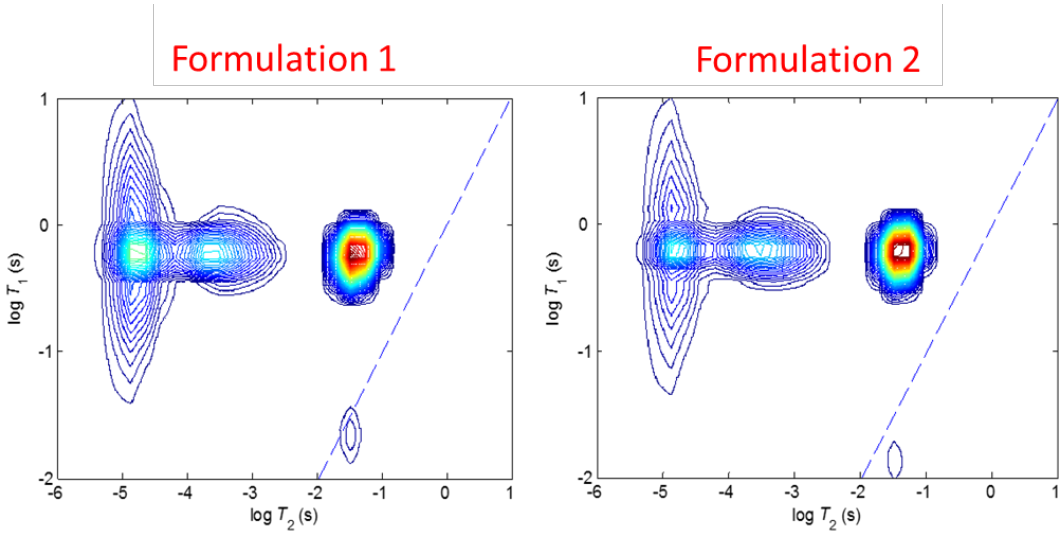

Figure 5.1. T_1-T_2 maps of the wet formulations at 22°C. The contour intensity (red highest) indicates the proportion of hydrogen spins in the sample with that magnetic relaxation behavior.

Diffusion experiments (not shown) were also run on the wet formulations, and no differences were found between the diffusivity values of the water or polymer peaks in the two samples (D_{Water} ~ $2x10^{-9}$ m^2/s and D_{Poly} ~ $2.5x10^{-12}$ m^2/s). It was concluded that the overpowering water signal inherent in a 19 wt% solids sample was preventing small changes in polymer dynamics from being noticed.

Dry Films

T_1-T_2 experiments were run on dry films made from the two polymer formulations to yield the data shown in Figure 5.2.

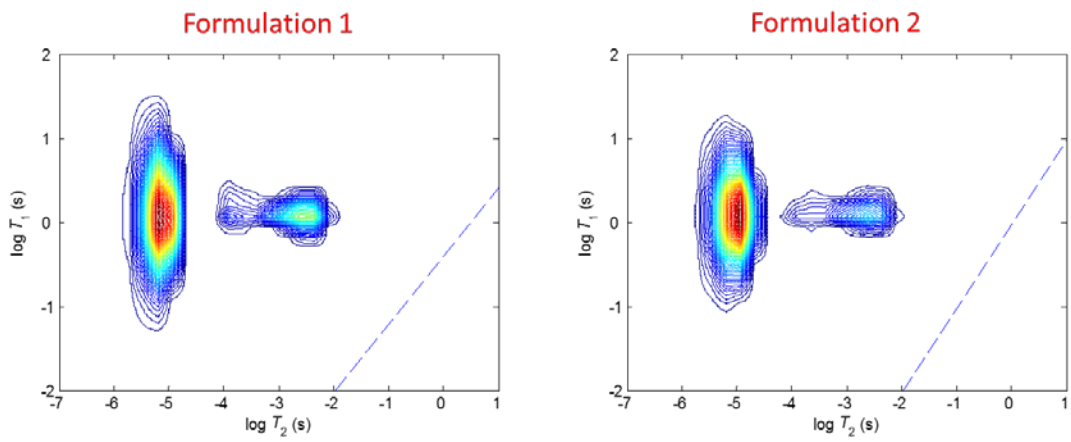

Figure 5.2. T_1-T_2 maps of the dry films from the polymer formulations. The contour intensity (red highest) indicates the proportion of hydrogen spins in the sample with that magnetic relaxation behavior.

As expected, the solid samples in Figure 5.2 show domains of much shorter T_2 values than the liquid samples in Figure 5.1. Comparison of the two data sets for the dry films indicates that the intensities of the longest T_2 populations differ. These populations relate to water molecules that are associated with the polymer but have a significantly higher mobility than that of the other domains in the sample. In formulation 1, this domain is fairly intense and accounts for 31% of the total map intensity, whereas formulation 2's longer T_2 domain has a lesser intensity and accounts for only 23% of the total signal intensity. This difference indicates that formulation 1 retains a larger amount of mobile water after film formation which likely contributes to its different mechanical properties.

To further investigate the water domain of high mobility, exchange between it and the population corresponding to water highly associated with the polymer (T_2 ~ 3.2 ms) was studied with T_2-T_2 exchange experiments. Data representative of short and long mixing times are shown

in Figure 5.3. The data is from formulation 1, but the maps acquired for formulation 2 were similar.

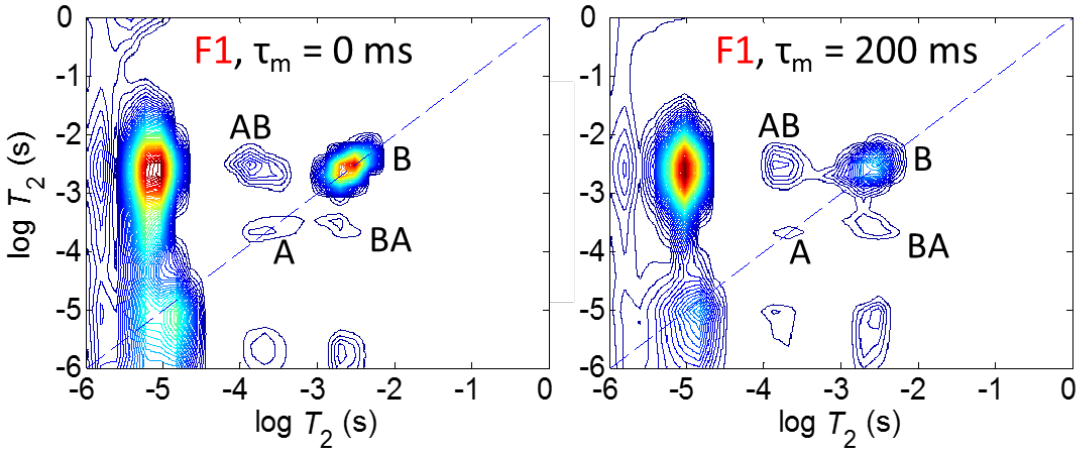

Figure 5.3. T_2-T_2 maps of formulation 1. Left, mixing time (τ_m) = 0 ms. Right, mixing time (τ_m) = 200 ms. The contour intensity (red highest) indicates the proportion of hydrogen spins in the sample with that magnetic relaxation behavior.

In Figure 5.3, peak A arises from spins highly associated with the polymer and peak B corresponds to the more mobile water domain. Peaks AB and BA represent spins that have translationally diffused from T_2 relaxation domains associated with peak A to domains associated with peak B and from B to A respectively during the mixing time. Although it is difficult to discern visually, peaks AB and BA are more intense relative to peaks A and B in the long mixing time map than in the plot for a mixing time of 0 ms. This increase in intensity is quantified by analyzing the seven maps for each formulation to produce the plot displayed in Figure 5.4.

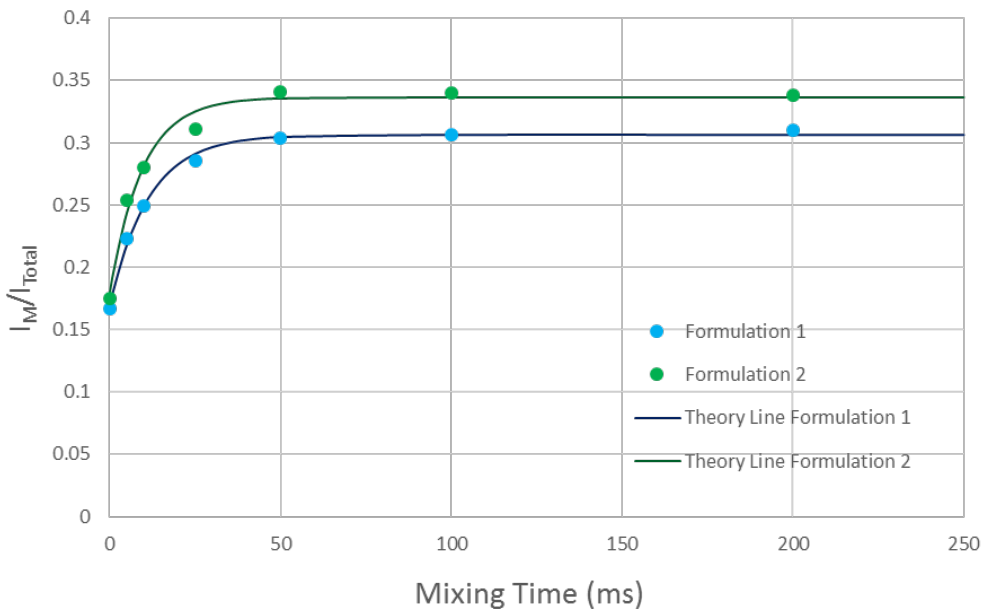

Figure 5.4. Two-site exchange model analysis of the dry film T_2-T_2 maps

The theory line fit of the formulation 1 data yielded a characteristic time (τ_c) of 11.4 ms, and the fit of the formulation 2 data produced a τ_c of 9.5 ms. Therefore, water molecules required a longer amount of time to diffuse from a domain close to the polymer to a more mobile domain farther away in the dry formulation 1 films than in the formulation 2 films. A tau time short enough to capture the dynamics in these solid films could not be implemented in a PGSE experiment so diffusion values were not found. Under the assumption that water diffusion in the two films is similar, the formulation 1 films exhibit a longer characteristic length scale than the formulation 2 films. This larger free volume domain size likely arises from the different molecular level structure of the two different polymer formulations.

Conclusions

After examination of dry film T_1-T_2 and T_2-T_2 experiments, it was concluded that formulation 1's different mechanical properties are related to an increased amount of more mobile water and a corresponding longer characteristic length scale than that seen in the dry formulation 2 films. Many factors such as rates of condensation and evaporation and capillary pressure contribute to the structure of a film, but the difference in free volume domain size between the films formed by the two polymer formulations can be simply understood by considering the branched polymers as fractal objects with radius *R*. For a group of fractal clusters of size *R* and dimension D in three-dimensional space, density decreases by $1/R^{3-D}$ so it is expected that larger precursor particles will form less dense films [67]. A precursor polymer of a larger average size will form a dry film that has a longer characteristic length scale, more high mobility water, and different mechanical properties.

FUTURE WORK

HPMCAS/Acetone Systems

- Determine the effects of adding flufenamic acid (active drug) to the systems
    - Implement fluorine and hydrogen NMR
    - Similar T_1-T_2, T_2-T_2, and diffusion experiments
- Discover if the T_1-T_2 method for finding T_g could be applied with an inexpensive, benchtop setup
    - Test runs with a low-field NMR system
- Further investigate glasslike dynamics in gelled polymer systems
    - Find MSD plateau for a variety of gelled polymer systems
    - Determine length scales via T_2-T_2 exchange for a variety of gelled polymer systems above their T_g
    - Consider relaxation modes in terms of light scattering data

Pseudolatex

- Acquire more data with only one varied parameter
    - Test pseudolatexes of the same age with varying plasticizer contents
    - Test pseudolatexes with the same plasticizer content over various ages
- Ensure sampling of all T_2 domains
    - Test for longer T_2 domains which may have been missed in this thesis data
    - Knowledge of all domains will allow for more complete conclusions to be drawn
- Attain rheology data on solutions with varied ages and plasticizer contents
    - Rheology data used in conjunction with NMR data will inform the polymer colloidal dispersion thermal gelation model
    - Acquire data before and after thermal gelation
- Study dried pseudolatex films

- Determine impact of aging and plasticizer on dry film formation
- Use T_1-T_2 correlation data, T_2-T_2 exchange data, and PGSE diffusion data

Dried Polymer Films

- Study changes in dry films over different relative humidities
  - Equilibrate at a high RH then return to a lower RH to study water uptake of the polymer films
  - Watch time scale changes with T_2-T_2 exchange data
- Optimize diffusion experiments to obtain diffusion coefficients in dry films
  - At high relative humidities, relaxation times may be long enough for a diffusion coefficient to be found
  - With a diffusion coefficient and a time scale, a characteristic length scale can be calculated
- Test different formulations
  - Discern if a trend of increased free water in the dry film with larger precursor polymers holds

REFERENCES CITED

1. Rabi, I.I., et al., *A new method of measuring nuclear magnetic moment.* Physical Review, 1938. **53**(4): p. 318-318.

2. Bloch, F., W.W. Hansen, and M. Packard, *Nuclear Induction.* Physical Review, 1946. **69**(3-4): p. 127-127.

3. Purcell, E.M., H.C. Torrey, and R.V. Pound, *Resonance Absorption by Nuclear Magnetic Moments in a Solid.* Physical Review, 1946. **69**(1-2): p. 37-38.

4. Becker, E.D., *A Brief History of Nuclear Magnetic Resonance.* Analytical Chemistry, 1993. **65**(6): p. A295-A302.

5. Callaghan, P.T., *Translational Dynamics & Magnetic Resonance*. 2011, New York: Oxford University Press.

6. Zeeman, P., *On the Influence of Magnetism on the Nature of the Light Emitted by a Substance .32.* American Journal of Physics, 1948. **16**(4): p. 218-223.

7. Traficante, D.D., *Impedance: What It Is, and Why It Must Be Matched.* Concepts in Magnetic Resonance, 1989. **1**: p. 73 - 92.

8. Lauterbur, P.C., *Image Formation by Induced Local Interactions - Examples Employing Nuclear Magnetic-Resonance.* Nature, 1973. **242**(5394): p. 190-191.

9. Vold, R.L., et al., *Measurement of Spin Relaxation in Complex Systems.* Journal of Chemical Physics, 1968. **48**(8): p. 3831-&.

10. Abragam, A., *Principles of Nuclear Magnetism*. 1961, Oxford: Clarendon Press.

11. Bloembergen, N., E.M. Purcell, and R.V. Pound, *Relaxation Effects in Nuclear Magnetic Resonance Absorption.* Physical Review, 1948. **73**(7): p. 679-712.

12. Carr, H.Y. and E.M. Purcell, *Effects of Diffusion on Free Precession in Nuclear Magnetic Resonance Experiments.* Physical Review, 1954. **94**(3): p. 630-638.

13. Hahn, E.L., *Spin Echoes.* Physical Review, 1950. **80**(4): p. 580-594.

14. Stejskal, E.O. and J.E. Tanner, *Spin Diffusion Measurements: Spin Echoes in the Presence of a Time-Dependent Field Gradient.* Journal of Chemical Physics, 1965. **42**(1): p. 288-+.

15. Hoult, D.I. and R.E. Richards, *Critical Factors in Design of Sensitive High-Resolution Nuclear Magnetic-Resonance Spectrometers.* Proceedings of the Royal Society of London Series a-Mathematical Physical and Engineering Sciences, 1975. **344**(1638): p. 311-340.

16. Keeler, J., *Phase Cycling Procedures in Multiple Phase NMR Spectroscopy of Liquids.* NATO ASI Series C. 322 (Multinucl. Magn. Reson. Liq. Solids: Chem. Appl.), 1990: p. 103 - 129.

17. Bloch, F., *Nuclear Induction.* Physical Review, 1946. **70**(7-8): p. 460-474.

18. Torrey, H.C., *Bloch Equations with Diffusion Terms.* Physical Review, 1956. **104**(3): p. 563-565.

19. Karger, J. and W. Heink, *The Propagator Representation of Molecular-Transport in Microporous Crystallites.* Journal of Magnetic Resonance, 1983. **51**(1): p. 1-7.

20. Callaghan, P.T., C.D. Eccles, and Y. Xia, *Nmr Microscopy of Dynamic Displacements - K-Space and Q-Space Imaging.* Journal of Physics E-Scientific Instruments, 1988. **21**(8): p. 820-822.

21. Einstein, A., *The motion of elements suspended in static liquids as claimed in the molecular kinetic theory of heat.* Annalen Der Physik, 1905. **17**(8): p. 549-560.

22. Callaghan, P.T., et al., *Diffraction-Like Effects in Nmr Diffusion Studies of Fluids in Porous Solids.* Nature, 1991. **351**(6326): p. 467-469.

23. Einstein, A., *The theory of the Brownian Motion.* Annalen Der Physik, 1906. **19**(2): p. 371-381.

24. Song, Y.Q., et al., *T-1-T-2 correlation spectra obtained using a fast two-dimensional Laplace inversion.* Journal of Magnetic Resonance, 2002. **154**(2): p. 261-268.

25. Hurlimann, M.D., L. Venkataramanan, and C. Flaum, *The diffusion-spin relaxation time distribution function as an experimental probe to characterize fluid mixtures in porous media.* Journal of Chemical Physics, 2002. **117**(22): p. 10223-10232.

26. Seymour, J., *HPMCAS Gels_JDS*, A. Dower, Editor. 2015.

27. Whittall, K.P. and A.L. Mackay, *Quantitative Interpretation of Nmr Relaxation Data.* Journal of Magnetic Resonance, 1989. **84**(1): p. 134-152.

28. Provencher, S.W., *Contin - a General-Purpose Constrained Regularization Program for Inverting Noisy Linear Algebraic and Integral-Equations.* Computer Physics Communications, 1982. **27**(3): p. 229-242.

29. Provencher, S.W., *A Constrained Regularization Method for Inverting Data Represented by Linear Algebraic or Integral-Equations.* Computer Physics Communications, 1982. **27**(3): p. 213-227.

30. Venkataramanan, L., Y.Q. Song, and M.D. Hurlimann, *Solving Fredholm integrals of the first kind with tensor product structure in 2 and 2.5 dimensions.* Ieee Transactions on Signal Processing, 2002. **50**(5): p. 1017-1026.

31. Godefroy, S. and P.T. Callaghan, *2D relaxation/diffusion correlations in porous media.* Magnetic Resonance Imaging, 2003. **21**(3-4): p. 381-383.

32. Lee, J.H., et al., *2-Dimensional Inverse Laplace Transform Nmr - Altered Relaxation-Times Allow Detection of Exchange-Correlation.* Journal of the American Chemical Society, 1993. **115**(17): p. 7761-7764.

33. Washburn, K.E. and P.T. Callaghan, *Tracking pore to pore exchange using relaxation exchange spectroscopy.* Physical Review Letters, 2006. **97**(17).

34. Friesen, D.T., et al., *Hydroxypropyl Methylcellulose Acetate Succinate-Based Spray-Dried Dispersions: An Overview.* Molecular Pharmaceutics, 2008. **5**(6): p. 1003-1019.

35. Ambike, A.A., K.R. Mahadik, and A. Paradkar, *Spray-dried amorphous solid dispersions of simvastatin, a low T-g drug: In vitro and in vivo evaluations.* Pharmaceutical Research, 2005. **22**(6): p. 990-998.

36. HARKE. *Product Catalog AQOAT (HPMC-AS, Hypromellose-Acetate-Succinate)*. 2016 [cited 2016 3/16].

37. Mallamace, F., et al., *The role of the dynamic crossover temperature and the arrest in glass-forming fluids.* European Physical Journal E, 2011. **34**(9).

38. de Wijn, A.S., et al., *Criticality in Dynamic Arrest: Correspondence between Glasses and Traffic.* Physical Review Letters, 2012. **109**(22).

39. Cohen, M.H. and G.S. Grest, *Liquid-Glass Transition, a Free-Volume Approach.* Physical Review B, 1979. **20**(3): p. 1077-1098.

40. Kumar, S.K. and J.F. Douglas, *Gelation in physically associating polymer solutions.* Physical Review Letters, 2001. **87**(18).

41. Fox, T.G., *Influence of Diluent and of Copolymer Composition on the Glass Temperature of a Polymer System.* Bulletin of the American Physical Society, 1956. **1**(2): p. 123.

42. Angell, C.A., *Liquid fragility and the glass transition in water and aqueous solutions.* Chemical Reviews, 2002. **102**(8): p. 2627-2649.

43. Ashland. *AquaSolve: Hydroxypropylmethylcellulose acetate succinate Physical and chemical properties handbook*. 2015 April 2016].

44. Kalogeras, I.M., *A novel approach for analyzing glass-transition temperature vs. composition patterns: Application to pharmaceutical compound plus polymer systems.* European Journal of Pharmaceutical Sciences, 2011. **42**(5): p. 470-483.

45. McDonald, P.J., et al., *Surface relaxation and chemical exchange in hydrating cement pastes: A two-dimensional NMR relaxation study.* Physical Review E, 2005. **72**(1).

46. Sun, C. and G.S. Boutis, *Measurement of the exchange rate of waters of hydration in elastin by 2D T-2-T-2 correlation nuclear magnetic resonance spectroscopy.* New Journal of Physics, 2011. **13**.

47. Gennes, P.-G.d., *Scaling Concepts in Polymer Physics*. 1979, Ithaca, United States: Cornell University Press.

48. Mair, R.W., et al., *The narrow pulse approximation and long length scale determination in xenon gas diffusion NMR studies of model porous media.* Journal of Magnetic Resonance, 2002. **156**(2): p. 202-212.

49. Mitra, P.P., et al., *Diffusion Propagator as a Probe of the Structure of Porous-Media.* Physical Review Letters, 1992. **68**(24): p. 3555-3558.

50. Sen, P.N., *Time-dependent diffusion coefficient as a probe of geometry.* Concepts in Magnetic Resonance Part A, 2004. **23A**(1): p. 1-21.

51. Williamson, N., *7 wt% Acetone Diffusion Data*, A. Dower, Editor. 2014.

52. Weeks, E.R. and D.A. Weitz, *Properties of cage rearrangements observed near the colloidal glass transition.* Physical Review Letters, 2002. **89**(9).

53. Sokolov, E.a., *Statistical Thermodynamics and Stochastic Theory of Nonlinear Systems Far from Equilibrium*. Series on Advances in Statistical Mechanics. Vol. 8. 2005: World Scentific Publishing Company.

54. Lascaris, E., et al., *Diffusivity and short-time dynamics in two models of silica.* Journal of Chemical Physics, 2015. **142**(10).

55. Hoy, R.S. and G.H. Fredrickson, *Thermoreversible associating polymer networks. I. Interplay of thermodynamics, chemical kinetics, and polymer physics.* Journal of Chemical Physics, 2009. **131**(22).

56. Quintanar-Guerrero, D., et al., *Pseudolatex preparation using a novel emulsion-diffusion process involving direct displacement of partially water-miscible solvents by distillation.* International Journal of Pharmaceutics, 1999. **188**(2): p. 155-164.

57. Miller, M., *Aqueous Polymeric Film Coating*, in *Pharmaceutical Dosage Forms: Tablets, Volume 1: Unit Operations and Mechanical Properties (3rd Edition)*, S.W.H. Larry L. Augsburger, Editor. 2008, CRC Press: New York, NY, USA.

58. McAllister, J.W., et al., *Thermodynamics of Aqueous Methylcellulose Solutions.* Macromolecules, 2015. **48**(19): p. 7205-7215.

59. Kapnistos, M., et al., *Reversible thermal gelation in soft spheres.* Physical Review Letters, 2000. **85**(19): p. 4072-4075.

60. Sarkar, N., *Thermal Gelation Properties of Methyl and Hydroxypropyl Methylcellulose.* Journal of Applied Polymer Science, 1979. **24**(4): p. 1073-1087.

61. Seymour, J., *Colloidal Dispersion Thermal Gelation Rheology*, A. Dower, Editor. 2015.

62. Davis, M.B., *Preparation and Stability of Aqueous-Based Enteric Polymer Dispersions.* Drug Development and Industrial Pharmacy, 1986. **12**(10): p. 1419 - 1448.

63. W.B. Russel, D.A.S., W.R. Schowalter, *Colloidal Dispersions*. 1989, United Kingdom: University Press, Cambridge.

64. Mills, R., *Self-Diffusion in Normal and Heavy-Water in Range 1-45 Degrees.* Journal of Physical Chemistry, 1973. **77**(5): p. 685-688.

65. Mark, E.H.I.a.H.F., *Plasticization and Plasticizer Processes.* Advances in Chemistry; American Chemical Society, 1965.

66. Fedorko, P., et al., *Insulator-metal transition in polyaniline induced by plasticizers.* Synthetic Metals, 2003. **135**(1-3): p. 327-328.

67. Brinker, C.J., et al., *Fundamentals of Sol-Gel Dip Coating.* Thin Solid Films, 1991. **201**(1): p. 97-108.